In memory of my business partner at "1st Memory Alloys GmbH", a talented engineer, the founder, owner and long-time managing director of "Ultrasonics Steckmann GmbH", the hobby pilot who crashed, resurrected and ascended again into the sky, a very pragmatic businessman with romantic soul traits, a rock in the surf and simply fine fellow and good comrad

Helge George Dr. Steckmann (1941-2018)

Inhalt:

1. Waves 5
1.1 General 5
1.2 Sound waves. 6
1.3 Ultrasonic range 6
1.4 Generating US vibrations 7
1.5 US measurements of elastic constants in solids 8
1.6 Acoustic emission measurements 9
2. US effects and their applications 13
2.1 Cavitation. 13
2.2 Ultrasonic friction reduction 13
2.3 Friction as the basis of ultrasonic grinding 15
3. US welding and processing of thermoplastics 19
3.1 Viscoelastic properties of thermoplastics 19
3.2 Energy dissipation as internal heat and US joining principle 21
3.3 US welding technique and technology 23
3.4 US welding parameters and weldability of thermoplastics 28
4 Metal joining in the ultrasonic welding process 43
4.1 Basics 43
4.2 State of research and technique 44
4.3 Experimental 49
4.4 Structure of the contact zone in metal pairings 53
4.5 Conclusions 65
5. Plastification of metal parts in US welding process 67
6. US residual stress reduction in metallic workpieces 77
6.1 Building internal stresses 77
6.2 Reduction of residual stresses 79
6.2.1 Reduction mechanism of supercritical residual stresses. 79
6.2.2 Reduction mechanism of subcritical residual stresses 81
6.3 Relaxation of residual stresses by thermally activated processes 82
6.4 Reduction of residual stresses by US-treatment 85
6.4.1 Physical requirements. 85
6.4.2 Heat and stress effects by US-vibration 87
6.4.3 Ultrasonic-specific plastification effects 89
6.5. US technique for treatment of metallic workpieces 90
7. Appendix. Ultrasonic devices and systems 93
8. References 115

1. Waves

1.1 General

The propagation of waves in space and time is generally described by the wave equation (one-dimensional x):

$$\frac{\partial^2 A(x,t)}{\partial x^2} = \frac{1}{c^2} \cdot \frac{\partial^2 A(x,t)}{\partial t^2} \qquad (1.1)$$

with a solution for linear harmonics (fig. 1.1):

$$A(x,t) = A_0 \cdot \sin(2\pi f \cdot t + \phi), \qquad (1.2)$$

where f is vibration frequency, and ϕ is wave phase.

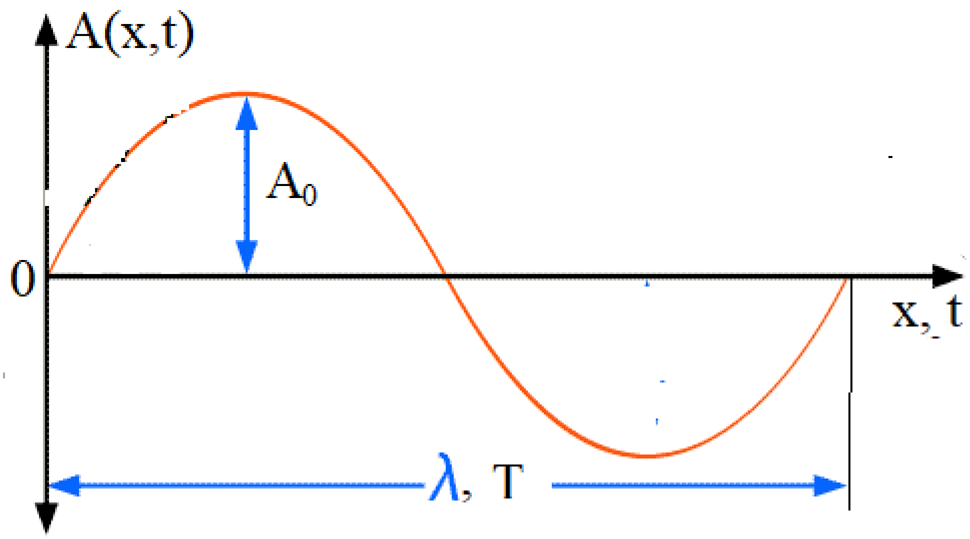

Fig. 1.1. A harmonic vibration

The general wave parameters are [1]: amplitude $A(x,t)$ with a maximum start value $A_0[m]$, period $T[s]$, frequency $f = \frac{1}{T}\left[s^{-1} \equiv Hz\right]$, wavelength $\lambda = \frac{c}{f}[m]$, propagation velocity $c = \sqrt{\frac{1}{\rho \cdot \kappa}}\left[m \cdot s^{-1}\right]$ (κ is compressibility) and density of the medium $\rho\left[kg \cdot m^{-3}\right]$. Waves only transfer energy and no mass as they propagate.

1.2 Sound waves

In contrast to electromagnetic waves and light, sound waves do not propagate in empty space (vacuum), but only in matter. In that sense, the term “dark matter” introduced by astrophysicists for the hypothetical invisible part of cosmic space is somewhat misleading, because if it were matter and not some "dark field" it would be a medium for the propagation of sound waves from stars, their explosions, implosions, collisions and all other catastrophes and cataclysms throughout infinite space. The invisible matter would have made the entire universe or its past billions of “sound years” away audible for us. That wouldn't be all that amusing for us, humans, I would say it.

1.3 Ultrasonic range

The sound waves are divided and defined based on the frequency range audible to humans from $16Hz$ to $16000Hz \equiv 16kHz$. Frequencies below the audible range belong to infrasound. Although infrasound is not used in practice, it is very present in the environment and affects the human organism [2]. The infrasound waves can radiate through the surface of “calm” oceans, causing seafarers to disembark from their fully intact ships. This is one of the explanations for the notorious phenomenon of “ghost ships”.

Frequencies lying above the audible range are understood as ultrasound (ultrasonic, US), which is well known in technology and medicine. Ultrasonic is very common in both the human and animal world for locating and measuring distances from objects. The sonar (for horizontal US propagation) and echo sounding (for vertical US propagation) methods are based on reflection of the US waves at interfaces of objects with a different density (impedance) than the medium (air, water, solid).

US reflection is also the basis for material testing [3]. The reflection as well as refraction, diffraction and interference are the basic wave properties that also apply to US waves and are described by the wave theory (Huygens' principle).

Thanks to diffraction, the US waves can penetrate into the shadow area of an object under the appropriate ratios of their wavelength and the size of the object.

1.4 Generating US vibrations

The US vibrations are generated by a piezoelectric transducer due to the piezoelectric effect. The direct piezoelectric effect is that a uniaxial mechanical stress leads to the polarization of a dielectric crystal, i.e. to the formation of electrical dipoles in this crystal oriented along the stress axis. This causes a macroscopic electric field in and around the so-called piezo element (transducer). PZT ceramics (piezo zirconate titanate) are usually used as piezo elements.

The inverse piezo effect is used to generate mechanical vibrations, in which mechanical stress or elastic deformation of the piezo crystal is generated by applying an electrical voltage. In the case of ferroelectric piezoceramics, the electric dipole moments below the Curie temperature are already present. The dipole moments directed parallel to each other form chaotically oriented electrically charged microdomains with a resulting electrical voltage, so-called Weiss areas known from ferromagnetism, so that no resulting macroscopic electrical moment is achieved in the entire piezoelectric crystal.

When the external electrical voltage is applied, the Weiss areas rotate in such a way that all dipole moments are oriented in the direction of the external electrical voltage. This polarization causes a deformation of the anisotropic piezoelectric crystal, e.g. an extension. Processes similar to the formation of chaotically oriented micromonodomains in ferromagnetic materials and piezoelectric materials (ferroelectric materials) when the temperature falls below the Curie temperature take place in shape memory alloys (SMA) with martensitic transformations when the temperature falls below a characteristic temperature [4].

Each such micromonodomain represents an elementary carrier of the lattice deformation caused by the martensitic transformation. The resulting macroscopic and reversible deformation of the entire SMA body consisting of such micromonodomains is only caused by the orienting effect of the applied external mechanical stress.

By changing the direction of the electrical external voltage acting on a piezoelectric crystal, mechanical vibrations with frequencies up to the US range are generated in such a piezoelectric crystal, which are used for many technical and medical purposes.

1.5 US measurements of elastic constants in solids

The piezo transducers can fulfill both sensor and actuator functions in one and can be used as such, e.g. when measuring the modulus of elasticity in metal samples. The signal from a US transducer is sent into a flat, plane-parallel polished sample, and the echo signals resulting from the reflection from the opposite sample surface are captured by the same transducer and converted into electrical signals.

The time τ measured between two adjacent echo signals is used to calculate the US velocity v_{US} in this crystal:

$$v_{US} = \frac{2d}{\tau}, \tag{1.3}$$

where d is the thickness of the sample. Since this velocity depends on the elasticity modulus G and the density ρ of the sample (§1.1):

$$v_{US} = \sqrt{\frac{G}{\rho}}, \tag{1.4}$$

the elasticity modulus can be easily calculated:

$$G = v_{US}^2 \cdot \rho. \tag{1.5}$$

If such US measurements are carried out on single-crystal samples with different orientations, the values of individual components C_{ij} of the elasticity tensor $\left\| C_{ij} \right\|$ are determined. The temperature dependencies of elastic constants determined in this way are widely used for investigating the softening of the determined elastic constants in the pre-martensitic temperature range in shape memory alloys [5-8].

1.6 Acoustic emission measurements

The direct piezo effect is the basis of piezoelectric sensors for registering acoustic signals (acoustic emission, AE). Acoustic emission occurs in solids as a result of sudden changes in the inner field of elastic stresses, for example when cracks form or during martensitic transformations [4].

In such AE-measurements [4, 9], a piezo transducer as a sensor with a resonance frequency of $400 kHz$ is attached directly to the polished surface of a sample to be examined using a thermal paste that secures the acoustic contact. The electrical signals generated by the sensor through acoustic pressure waves are electronically amplified, digitized by an A/D converter and visualized on a computer screen (fig. 1.2).

Depending on the type of transformation and heat treatment, the frequencies of the acoustic signals during martensitic transformations of shape memory alloys can range from audible, where one can hear the crackling of annihilating phase or domain boundaries with bare ears [4], to the ultrasonic range.

The AE intensity I_{AE} is recorded as the number of acoustic signals (pulses) per second $\dot{N}_{AE}(T) \left\lfloor imp \cdot s^{-1} \right\rfloor$ as the temperature changes at a constant rate $\dot{T} = const$ in the transformation temperature range $(A_f ' - M_f ')$:

$$I_{AE} \propto \dot{N}_{AE}(T) \propto \frac{U_d}{U_{el}} \cdot \frac{\dot{T}}{A_f{}' - M_f{}'} \quad , \tag{1.6}$$

where U_{el} is the elastic energy of the phase boundaries and U_d is the elastic energy dissipated as acoustic emission.

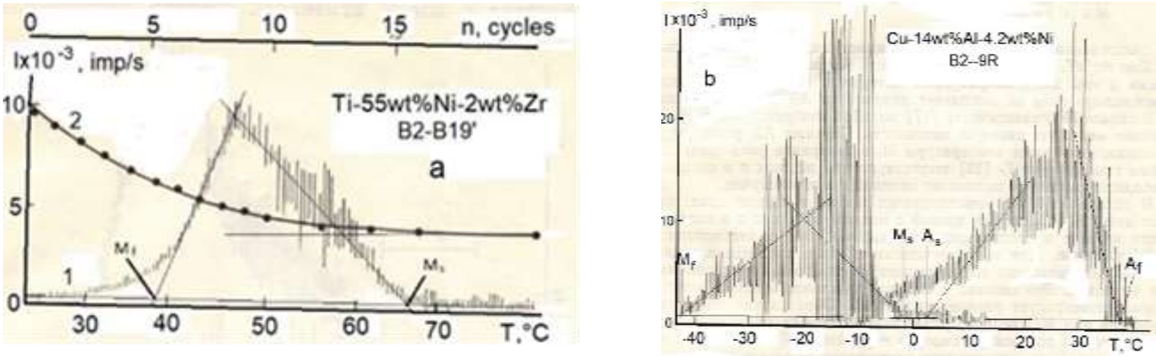

Fig. 1.2. AE measurement curves of polycrystalline SMA samples $Ti-55wt\%Ni-2wt\%Zr$ in the first cycle of the thermo-induced $B2 \rightarrow B19'$ martensitic forward transformation (a - line 1) and $Cu-14wt\%Al-4.2wt\%Ni$ in the first cycle of the thermo-induced martensitic forwards and reverse $B2 \leftrightarrow 9R$ transformations (b). Decrease in AE intensity with the number of transformation cycles (a - line 2).

The acoustic signals during the martensitic transformation arise from the coalescence of martensite crystals growing during the transformation with the formation of internal martensitic domain boundaries with much lower elastic energy densities. During reverse transformation, splitting these internal martensitic domain boundaries takes place into the coherent austenite-martensite phase boundaries with much higher elastic energy density [4].

These abrupt changes in elastic energy density cause acoustic emission, so the number of acoustic pulses is approximately equal to the number of phase boundaries:

$$N_{AE}(T,z) \approx N^{A'M^p} = 2N_{M_f}^{M^p} \cdot z(1-z), \tag{1.7}$$

where $N_{M_f}^{M^p}$ is the number of martensite polydomains M^p after complete forwards transformation at the temperature $T \le M_f$ and at martensite phase fraction $z(T) = 1$.

The decrease in AE intensity with the number of transformation cycles shown in Figure 2a, line 2, which was also observed in other kinds of investigations [10], is due to the stabilization of some martensite crystals by changing their internal domain structure in the field of internal elastic stress [4] and not to the loss of coherence of the phase boundaries by the faults, as is claimed in most cases. Namely, reducing the density of twin boundaries in a martensite crystal leads, as it has been prooved experimentally in [4], to an increase in its reverse transformation temperatures, so that the martensite crystal is eliminated from the reverse transformation cycles in this temperature range.

2. US effects and their applications

The numerous US applications are based on the diverse properties of ultrasonic as pressure waves and its effects on the propagation medium (gases, liquids, solids).

2.1 Cavitation

Actually, cavitation is not explicitly a US specific phenomenon. The formation of cavities (vapour bubbles) in liquids and their implosion on the surfaces of obstacles generally occurs in strong turbulent flows with large pressure drops, e.g. at the ship's propellers. The vapor bubbles form in liquids at the points of minimum pressure, where the equilibrium between water and water vapor can be reached on the $(p-T)-$diagram already at room temperature.

The resistance of obstacles increases the pressure in the cavitated fluid, causing the vapor bubbles to collapse suddenly. The explosively increasing pressure and temperature causes erosion of the obstacle surface and significant damage to them. However, this effect finds a positive use in US cleaning baths (e.g. lenses cleaning).

In metallurgy, too, cavitation by ultrasonic effect on metal melts is an important application, in which their US treatment has a positive influence on the quality of cast parts. The process is based on the creation of cavitation bubbles in the melt, which induces a dispersion and degassing effects. The analysis of the structure and the determination of the mechanical properties of the resulting cast parts are the basis for determining the quality of light metals such as magnesium, aluminum and their alloys [11, 12].

2.2 Ultrasonic friction reduction

Static frictional force F_f acts on the interfaces between two bodies pressed against each other with a force F_N acting normal to the surface and is related to the normal force as follows:

$$F_f = \mu \cdot F_N, \quad (2.1)$$

where μ is a coefficient of friction determined by the nature of the interfaces and body fabric.

The frictional force always opposes the force F_d trying to set the contacting bodies in motion. Friction force depends on the velocity v of movement [13]:

$$F_f = -\alpha \cdot \vec{v}, \; v \le 25 m/s \quad (2.2)$$

$$F_f = -\beta \cdot v^2 \frac{\vec{v}}{v}, \; (25 < v < 350) m/s \quad (2.3)$$

If the US vibrations are applied to one of the bodies in contact, the friction behavior changes. The pressure of a vibrating body counteracts the normal force F_N at the contact points one wavelength λ (fig. 2.1), thereby reducing friction.

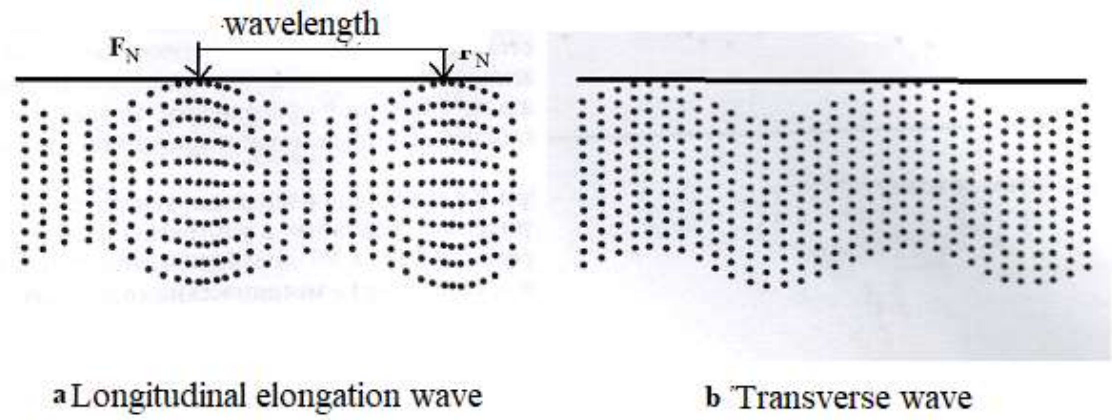

Fig. 2.1. US wave kinds.

If you try it for example, to hold tight the blade of a switched-on US cheese knife with your fingers, you can feel the fingers being pushed off and slide away in the direction of wave propagation. Since the friction coefficient is not changed, the US effect of friction reducing differs from the lubricants effect reducing the friction coefficient μ.

US friction reduction is used very effectively in various metalworking processes such as wire drawing, extrusion, deep pressing, etc. applied to reduce the acting force and to avoid or to reduce the sticking of metal to the tools [14].

The friction created at the interface of two metal parts, if they are moved relative each other with the force F_f by ultrasonic action, can also produce a positive grinding effect at the two rough interfaces.

2.3 Friction as the basis of ultrasonic grinding

The problem with the production of precision mechanical components is that their surface roughness after milling/turning makes their precise use impossible and is intolerable. To solve the problem, a lengthy and ineffective hand grinding process is used.

The investigations [15] carried out on behalf of the companies "Leica Camera AG" and "Ultrasonics Steckmann GmbH" showed a very satisfactory smoothing of the microthreads of the lens parts screwed into each other by applying the US vibrations to the lens of the photo camera.

Light micrographs of thread sections of the aluminum and brass lens parts indicate that friction on the threads of the pairing parts is mainly caused by the surface roughness of parts after thread milling/turning (figures 2.2 a and 2.4 a).

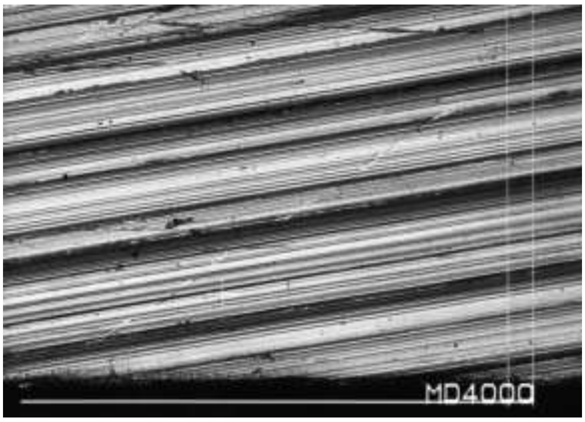

Fig. 2.3 a. The thread of the aluminum part after one-sided ultrasonic acting.

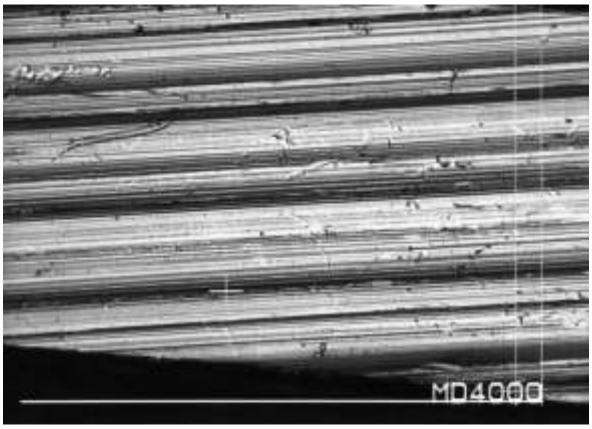

Fig. 2.3 b. The thread of the aluminum part after two sides ultrasonic acting.

The hand grinding aluminum surface remains rough (fig. 2.2 b). However, the aluminum particles created and deposited during processing are rounded off, aligned along the thread (textured) and partially smeared into the surface, which of course should result in a reduction in friction.

US-treatment of the lens parts screwed into each other by applying the sonotrode to one side of the lens smoothes both the aluminum surface (figures 2.3 a, b) and the brass surface (figures 2.5 a, b) extremely efficient. On the light micrograph (fig. 5 a) there is absolutely no trace of said aluminum particles.

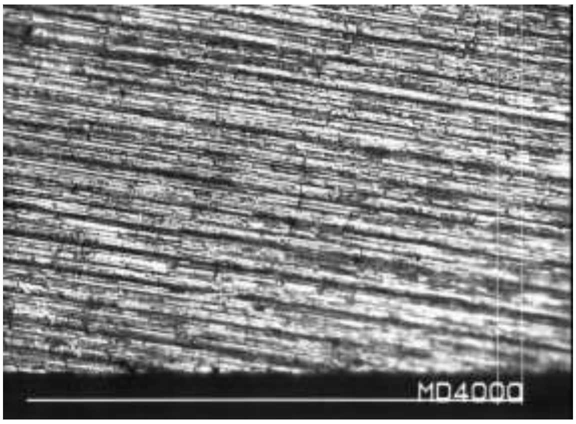

Fig. 2.4 a. The thread of the brass part after milling/turning.

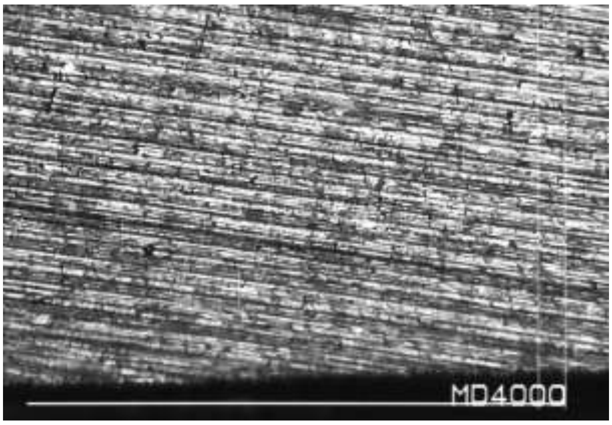

Fig. 2.4 b. The thread of the brass part after hand grinding.

The surface of the brass part after its production is relatively smooth (fig. 2.4 a) and changes only insignificantly with further treatments (fig. 2.4 b), although here too there is a positive ultrasonic effect (figures 2.5 a, b) compared to hand grinding (fig. 2.4 b) can be determined. When grinding by hand, not only the roughness, but also the thread itself is somewhat smeared, while the thread remains originally sharp after US treatment.

The US treatment by a semicircular sonotrode with the 180° rotation has the same effect (figures 2.4 a and 2.6 b) as that with a planar sonotrode. US-treatment by applying the sonotrode to the both lens parts (figures 2.3 b and 2.5 b) is less effective than applying the sonotrode to one side (figures 2.3a and 2.5 a). The surfaces are still smoother than those after hand grinding (figures 2.2 b and 2.4 b), but in contrast to the other US methods considered here (figures 2.3 a and 2.5 a), they show residual traces of granular particles.

Since these two US treatments are more complex and achieve the same or even lesser effect, the use of these methods is not particularly sensible for economic reasons alone and is not recommended.

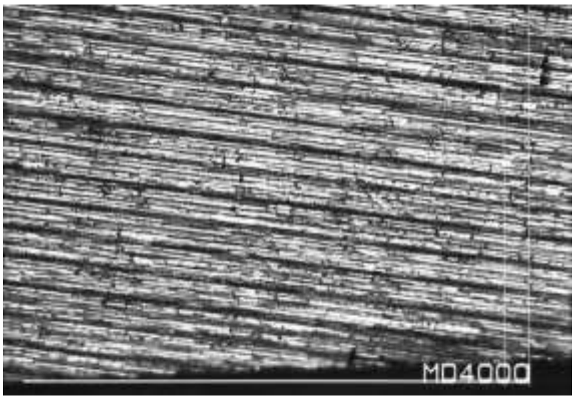

Fig. 2.5 a. The thread of the brass part after one-sided ultrasonic acting.

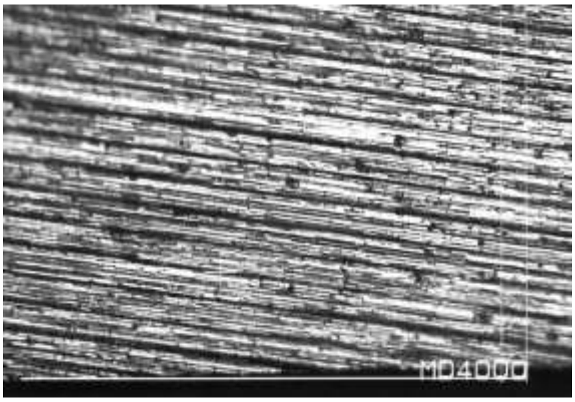

Fig. 2.5 b. The thread of the brass part after two-sided ultrasonic acting.

The influence of the US treatment on the roughness of the aluminum surface is based on the metal plastification investigated here (chapter 5). The lens parts screwed together exert mechanical pressure on each other, especially on the rough areas of the thread surface.

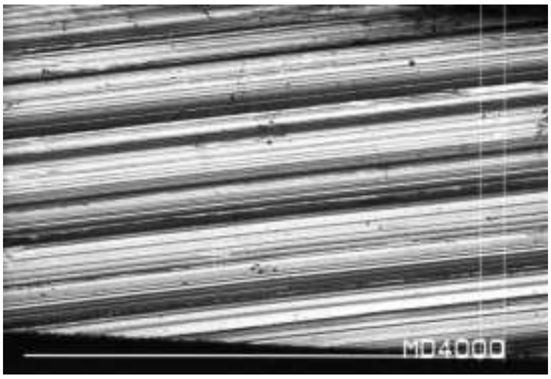

Fig. 2.6 a. The thread of the aluminum part after ultrasonic acting through a semicircular sonotrode, rotated by 180°.

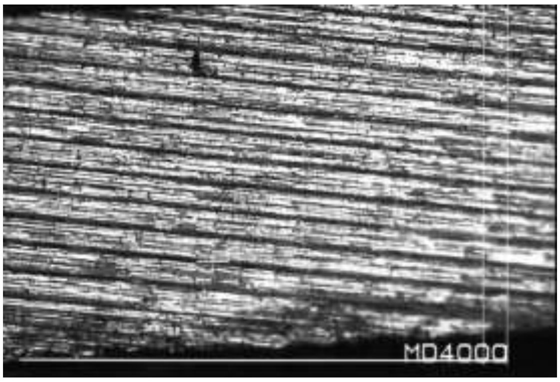

Fig. 2.6 b. The thread of the brass part after ultrasonic acting through a semicircular sonotrode rotated by 180°.

The US vibrations lead to heat production on the contact surface. Through the mechanical pressure, the tangential stresses and the heat, the aluminum yield point is reached, i.e. the aluminum particles are plastificated and smeared into the surface of the aluminum part, so that a perfect smoothing effect is achieved.

The weaker result of the US treatment when placing two sonotrodes on the both parts is probably due to the fact that the two movements are missynchronized and minimize the relative amplitude of the counter-vibration. A better effect is achieved if one part serves as an anvil and remains immobile.

The friction generated by US vibrations under the pressing force and the associated temperature increase in the contact zone also proved to be the basis of US welding of thermoplastics and US metal joining in these investigations.

3. US welding and processing of thermoplastics

3.1 Viscoelastic properties of thermoplastics

US welding thermoplastics is used to join two different molded parts together [16]. This is a welding process most commonly used for this purpose as it lasts from a split second to few seconds, produces clean and strong welds, and it is easy to automate and to integrate into mass production.

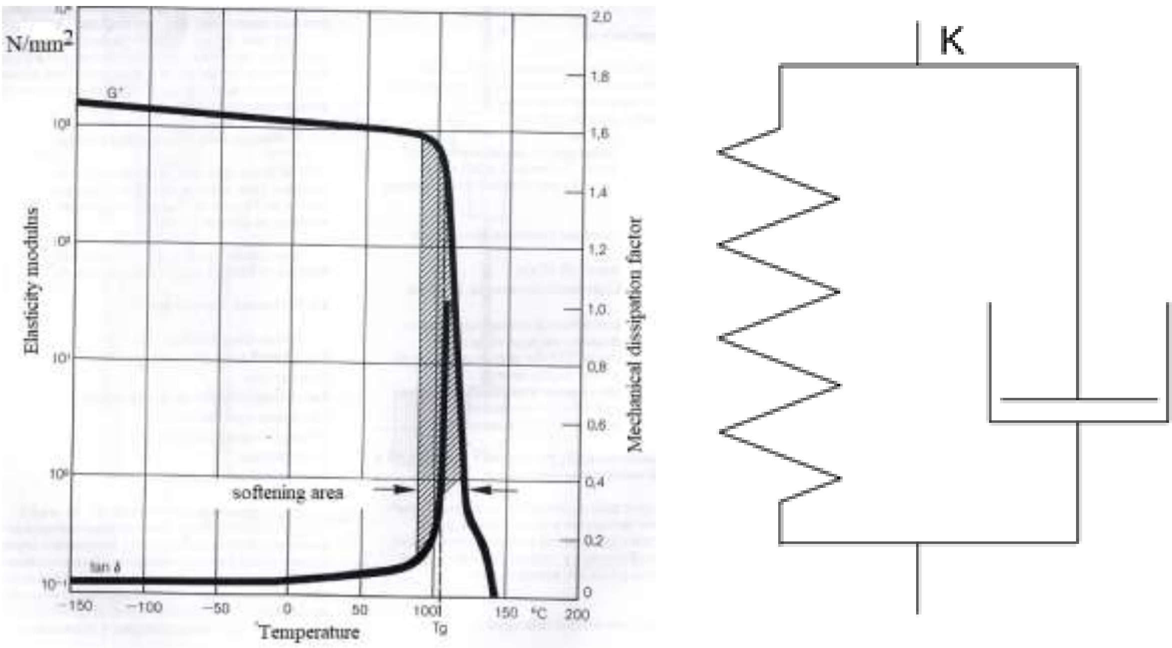

a b

Fig. 3.1. Temperature dependence of the elasticity modulus and the mechanical loss (dissipation) factor $\tan\delta$ of one of the amorphous thermoplastics (**a**)**,** the rheological Kelvin-Voigt model (**b**) with an elastic component (spring) and a viscous component (damper) connected in parallel..

During US welding of thermoplastics, the plastic molded parts are made to vibrate. The continued vibration heats and softens the plastic and then mixes the softened surfaces of the plastic together. This creates both a physical and, with the right choice of plastics, a chemical connection between the moldings.

Thermoplastics as solids have an irregular amorphous molecular structure with short-range order, like it in glass, or a mixed amorphous and crystalline structure with long-range order, like it in all crystalline solids. Amorphous thermoplastics lose their strength when heated up to the glass transition temperature T_g (fig. 3.1 a), become plastic and easily mouldable.

Mixed structures show two softening areas: one for the amorphous component at the temperature T_g and one for the crystalline component around the melting temperature T_m (fig. 3.2).

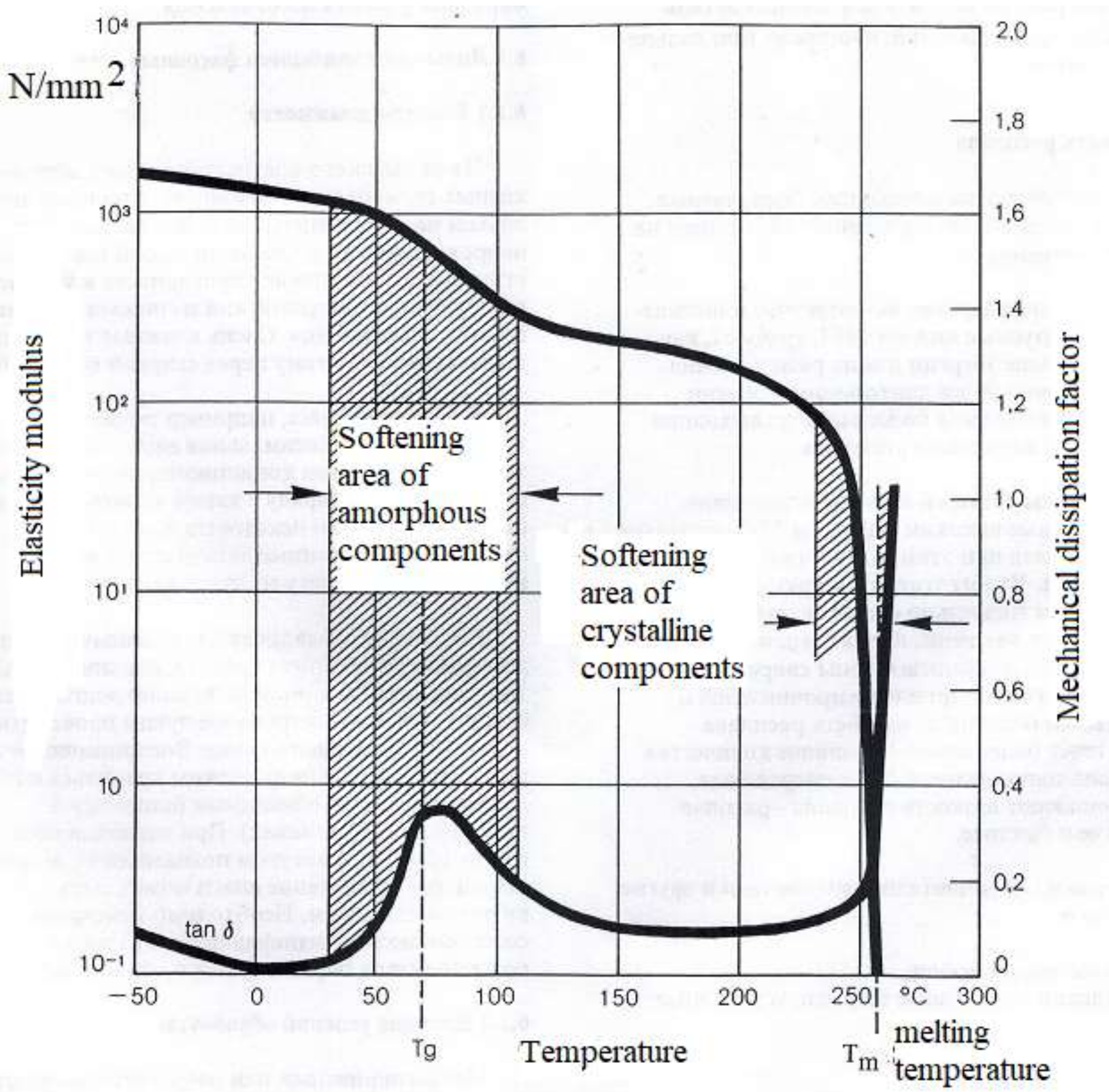

Fig. 3.2. Temperature dependence of the elasticity modulus and the mechanical loss factor $\tan\delta$ of one of the semi-crystalline thermoplastics.

The amorphous thermoplastics are viscoelastic materials which, when deformed, have both an elastic, reversible component and a viscous, time-dependent damping component. A viscoelastic material under an external vibrational shear stress is represented in rheology by a complex elasticity modulus as a complex number:

$$G^* = G^I + iG^{II}, \tag{3.1}$$

where G^I is the storage modulus, elasticity modulus of the elastic part, and G^{II} is the dissipation modulus for the viscous part (fig. 3.1 b). The ratio of the both modules determines mechanical energy losses:

$$\tan\delta = \frac{G^{II}}{G^I} \tag{3.2}$$

through internal friction [17-19].

3.2 Energy dissipation as internal heat and US joining principle

The longitudinal US vibrations with initial amplitude A_0^{US} propagate in the upper thermoplastic molded part as stress-strain cycles with viscoelastic deformation:

$$\varepsilon_{vel} = \frac{A_0^{US}}{x_{top}^{plast}} \tag{3.3}$$

and stress:

$$\sigma_{vel} = G_{top}^{II}(T) \cdot \varepsilon_{vel}, \tag{3.4}$$

where x_{top}^{plast} is the thickness of the upper plastic molded part or the distance between the sonotrode and the welding surface.

The damping component with the dissipation modulus $G_{top}^{II}(T)$ is responsible for energy dissipation whose mass density (per unit mass) corresponds to the area of the hysteresis loop in a one deformation cycle [4]:

$$h\left[\frac{J}{kg}\right]=\frac{1}{\rho_{top}^{plast}}G_{top}^{II}(T)\cdot\varepsilon_{vel}^{2}, \qquad (3.5)$$

where $\rho_{top}^{plast}=\dfrac{m_{top}^{plast}}{S_{weld}\cdot x_{top}^{plast}}$ is density of upper molding with mass m_{top}^{plast} and welding surface S_{weld}.

The density of the thermoplastic molded part should be checked before setting the welding parameters, because it depends on the purity of the plastic and increases in the presence of additives or glass fibers, which can make it difficult to weld thermoplastics.

The total dissipated energy per unit mass is then calculated as the energy loss in one cycle by multiplying the hysteresis area by the resonance frequency f_r^{US} of the sonotrode (number of cycles per second) and by the welding time t_{weld}:

$$e_{dis}^{US}\left[\frac{J}{kg}\right]=\frac{S_{weld}\cdot x_{top}^{plast}}{m_{top}^{plast}}\cdot G_{top}^{II}(T)\cdot\left(\frac{A_0^{US}}{x_{top}^{plast}}\right)^{2}\cdot f_r^{US}\cdot t_{weld}\,. \qquad (3.6)$$

The dissipated energy is transformed within the upper thermoplastic molding into the heat with the mass density $q_{top}^{plast}=\dfrac{Q_{top}^{plast}}{m_{top}^{plast}}$ required for heating the molding from the room temperature T_r to its softening range around the glass transition temperature T_g (Fig. 3.1a) or its melting temperature T_m in semi-crystalline thermoplastics (fig 3.2):

$$q_{top}^{plast}=c_p^{plast}\cdot(T_{g,m}-T_r)=e_{dis}^{US}, \qquad (3.7)$$

where c_p^{plast} is heat capacity of the upper molding, W_{gen}^{US} is the output power of the US generator and $e_{dis}^{US} = \frac{W_{gen}^{US}}{m_{top}^{plast}} \cdot tg\delta \cdot t_{weld}$ is mass density of the energy losses (3.6) for the US energy supplied into the molding by the US generator.

The described dissipation mechanisms and transformation of US energy into the heat is the basis for the US welding of thermoplastic molded parts. The same fundamentals apply to all other US thermoplastics technologies:

- near field welding (direct US welding)
- far field welding (indirect US welding)
- welding with inserted gasket
- welding of various molded parts (casting, extrusion, blow molding, thermoforming)
- welding of combinations of different molded parts
- spot welding
- seam welding and stitching
- welding of coated cardboards and fabrics
- riveting
- flanging
- hammering in
- embedding
- joining of molded parts with textiles

3.3 US welding technique and technology

The US welding process was found to be particularly suitable for this purpose in the 1950s and has been continuously developed since then, both in US technology and in the design of thermoplastic molded parts and weld surfaces.

An US welding system (fig. 3.3 a) essentially consists of a welding press that regulates the pressing force required for US welding, a generator (or several in complex block module systems), an US resonance module and welding tools: a sonotrode as a supplier of US energy and anvil as an absorber.

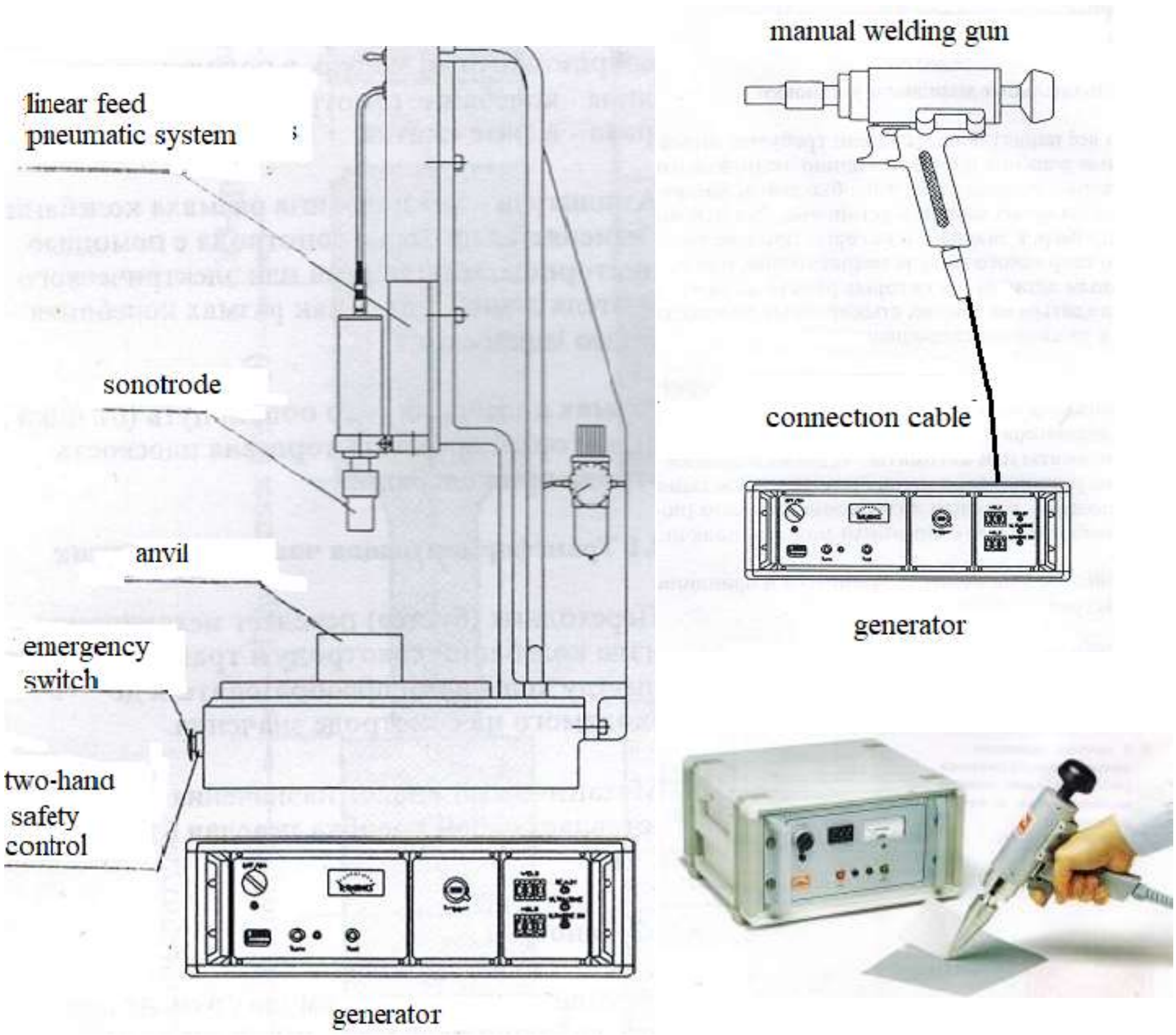

a **b**

Fig. 3.3. Ultrasonic technology: welding system (**a**) and manual welding gun (**b**), which are suitable for spot welding or for cutting foils and synthetic fabrics [15].

The mechanical US resonance module (fig. 3.4) consists of a piezoelectric US transducer, an adapter (converter, booster) and a sonotrode (also called horn) as a welding tool.

The US resonance module is the heart of every US welding system. In complex, fully automated US welding systems (fig. 3.3 a), there is also a pneumatic linear feed system (welding press) for automatic placement of the sonotrode on the upper thermoplastic molded part to be welded normal to the welding surface and for exercising a constant pressing force on that. In addition to the sonotrode, the welding tool also includes the anvil, which absorbs and dampens the constant pneumatic pressure and US vibrations. In US manual welding machines (fig. 3.3 b), the US converter is hidden in the housing with the handle and connected to the generator by a cable.

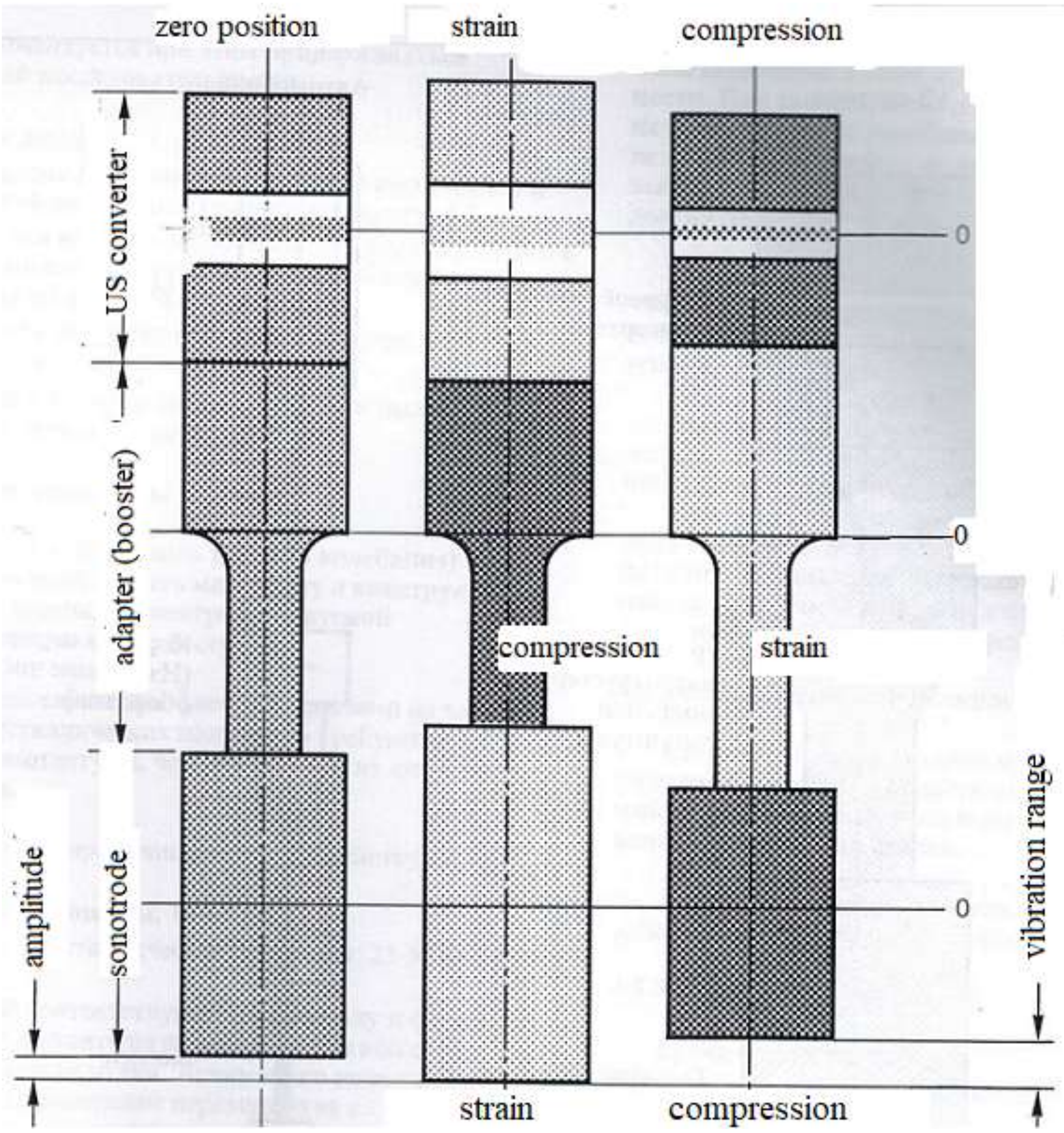

Fig. 3.4. The mechanical resonance module and its behavior.

In practice, linear pneumatic feed systems are used as welding presses, as shown in Figure 3.3a, but hydraulic or magnetic feed systems are also used in special cases. Generator can either be built into the welding machine or placed next to it, which makes the application more variable and the operation easier.

The following conditions are important for standard welding systems:

- compressed air connection (usually $6bar$)
- pressing force (up to $4000N$)
- adjustable work routine
- adjustable US switch-on time
- adjustable feed and placement velocities
- mechanical adjustment of the US resonance module
- free space between sonotrode and table or between sonotrode and the system frame
- precise control of the mechanical resonance module
- plane-parallel position of the sonotrode and of the anvil.

US generator transforms electrical energy from the electrical network into vibrational energy with the resonance frequency f_r^{US} required for the mechanical resonance module. The preferred resonance frequencies for US systems is $20kHz$. However, there are also systems (see appendix) that work with resonance frequencies of $35kHz$, $50kHz$ and $70kHz$.

The output power W_{gen}^{US} of a generator is adapted to its tasks. Power levels from $100W$ to $4000W \equiv 4kW$ are used for US welding of thermoplastics. The no-load power is the sum of the electrical system's own energy losses and energy losses of the mechanical resonance module. This should be minimal and always attuned to it.

Figure 3.4 shows the vibration behavior of the mechanical resonance module: the module is at rest on the left, the sonotrode is in the expansion or strain phase in the middle and the compression phase on the right. US vibration amplitude A_0^{US} is determined as one half of the vibration range (figures 1.1 and 3.4). It is measured on the front side of the sonotrode using an indicator micrometer or an electrical measuring device, while the vibration range is determined using a light microscope.

Converter (booster) directs the vibration energy from the US converter to the sonotrode and transforms the vibration amplitude of the US converter to the value of $(5 \div 300)\mu m$ required at the sonotrode.

The sonotrode is the tool used for ultrasonic welding, flanging, riveting etc. of thermoplastics, which vibrates normal to the contact surface and has the following tasks:

- transfer of the US vibration energy into the workpiece
- transmission of the pressing force to the workpiece
- change in amplitude
- shape design at shape changes

Particular attention is paid to the sonotrode, because good quality can only be guaranteed by correctly calculating the process parameters for the corresponding molded parts.

The lower molded part on the other side of the joint area rests on an energy absorbing anvil, ensuring that the ultrasonic energy stays in the weld zone. The anvil is the second tool opposite the sonotrode, which is used to position the lower molded part or as a guide for the upper molded part. Its surface is adapted to the shape of the lower part. The anvil is preferably made from the following materials:

- steel
- aluminum
- brass
- casting resin (mostly filled)

To protect sensitive molded part surfaces, anvil can be covered with elastic materials, e.g. PTFE, corks, rubber, elastomers.

The control part of the US welding system gives the user the opportunity to set all the necessary welding parameters. The following order is recommended:

- enter the amplitude

- correlation of the pressing force with the amplitude and the output power of the generator
- setting the switch-on time (dampening touchdown or touchdown of the freely vibrated sonotrode)
- adjustment of the touchdown velocity of the sonotrode
- adjustment of welding and holding time under the pressure

The US resonance frequency f_r^{US} and the amplitude A_0^{US} in (3.6) mostly determine the amount of energy dissipated in the upper molded part and are among the most important parameters of the US welding process. These are generated and adjusted in the mechanical resonance module of the US welding system.

3.4 US welding parameters and weldability of thermoplastics

Equations (3.6) and (3.7) contain all parameters relevant to the welding process, both of the US resonance module and US welding system (A_0^{US} , f_{res}^{US} , W_{gen}^{US}) and of the thermoplastic molded parts to be welded (ρ_{top}^{plast} , c_p^{plast} , $T_{g,m}$, $G_{top}^{plast}(T,z)$, S_{weld}^{plast} , x_{top}^{plast}) and can be used to adjust welding parameters or provide orientation (relationships between individual parameters) for practical tests, through which the welding parameters are otherwise determined empirically.

The US parameters for a US welding process should be coordinated with the nature of the thermoplastics (Table 3.1). The thermoplastics listed in Table 3.1 are of course best welded to themselves (diagonal in Table 3.1). The pairings lying outside the diagonal can only be welded to a limited extent or not at all (or if the experimental data is not available), but can be join using other US methods such as riveting and flanging.

The amplitude A_0^{US} should correspond to the material and construction of the molded part and the geometry of the weld surface. In general, larger amplitudes are set for molded parts made from partially crystalline thermoplastics than for those made from amorphous thermoplastics, because the former require more energy for their softening. The orientation values are:

- for amorphous polymers $A_0^{US} = (10 \div 30)\mu m$

- for semi-crystalline polymers $A_0^{US} = (25 \div 50)\mu m$.

Table 3.1. Weldability of different thermoplastics with each other

	ABS	PMMA	PC	PA	POM	PE	PP	PS	SAN	PVC	PPO	Mod. PPO	POLYSULF	POLYIMID	BUTYRATE	CELLULOSI
ABS	X	X	o					o	O	O					O	
PMMA	X	X	o					o	O							
PC	o	X	X													
PA				X												
POM					X											
PE						X										
PP							X									
PS	o	o						X	o	.		X				
SAN	O	O						o	X			O				
PVC	O									X						
PPO											X	X				
Mod. PPO (NORYL)								X	O		X	X				
POLYSULFONE													X			
POLYIMIDE														X		
BUTYRATE	O														X	
CELLULOSE - ACETAT																X

x good weldability
o limited weldability

The correct input of the amplitude corresponding to the requirements can usually only be determined by practical tests. The best way to determine them is to use boosters with different transmission ratios $n_{tr}^{boost} = \frac{A_{sonotrode}^{US}}{A_{wandler}^{US}}$, starting with the smallest value $n_{tr}^{boost} = 1$.

The interplay between the vibration amplitude A_0^{US} and the impact force of the sonotrode F_{son} can be estimated from the following considerations: the attached vibrating sonotrode hits on the upper molded part according to Newton's 2nd law with a force:

$$F_{son}[N] = m_{son}^{stirn} \cdot a_{son} = \rho_{son} \cdot S_{son} \cdot A_0^{US} \cdot 16 A_0^{US} \cdot (f_r^{US})^2 . \qquad (3.8)$$

where $m_{son}^{stirn} = \rho_{son} \cdot S_{son} \cdot A_0^{US}$ is the mass of the front part of the sonotrode, S_{son} is its surface, $V = S_{son} \cdot A_0^{US}$ is the volume of the space between the resting state and the maximum amplitude A_0^{US} in the straining phase (fig. 3.4), $a_{son} = \frac{s}{t^2} = 16 A_0^{US} \cdot (f_r^{US})^2 \left[m \cdot s^{-2}\right]$ is acceleration of the sonotrode front side, which is on the way $s = A_0^{US}$ during the time $t = \frac{1}{4} \cdot T \equiv \frac{1}{4 f_r^{US}}$ (fig. 1.1) is reached.

With a counterforce that is somewhat reduced by damping (inelastic impact), the molded part also acts back on the sonotrode according to Newton's 3rd law, which simply allows the sonotrode to bounce back, if it touches down without any pressing force. To avoid a destructive “hammering” effect, the pressing force $F_{anp}^{US} \geq F_{son}$ is needed.

With values of the steel density $\rho_{son} \approx 8 \cdot 10^3 kg/m^3$, US resonance frequency $f_r^{US} = 70 kHz \equiv 7 \cdot 10^4 Hz$, amplitude $A_0^{US} = 50 \mu m \equiv 5 \cdot 10^{-5} m$, and the surface of the sonotrode front side $S_{son} \approx 10^{-2} m^2$, one can estimate the impact force (3.8):

$$F_{son} = 16 \cdot 8 \cdot 25 \cdot 49 \cdot 10^{-1} \approx 1700N \qquad (3.9)$$

and the pressure acting on the upper molded part:

$$P_{son} = \frac{F_{son}}{S_{son}} \approx 170000Pa \equiv 0{,}17MPa \equiv 1{,}7bar. \qquad (3.10)$$

These estimates good agree with empirically determined values of the force $F_{anp}^{US} = 4000N$ and pneumatically generated pressure $P = 4bar$ (§3.3) acting on the weld surface, at least in order of magnitude, especially when considering that a doubling of the amplitude leads to a quadrupling of the force ($F_{son} = 6800N$) and the pressure ($P = 6{,}8bar$).

However, the formula (3.8) refutes the empirical assertion that the pressing force F_{anp}^{US} relates to the amplitude as $F_{anp}^{US} \geq F_{son} \propto 1/A_0^{US}$. According to (3.8), the pressing force depends parabolically on both the amplitude and the resonance frequency: $F_{anp}^{US} \geq F_{son} \propto \left(A_0^{US}\right)^2 \cdot \left(f_r^{US}\right)^2$. Though, the empirical claim may be true for the pressure on the weld zone without considering the "hammering"-effect. In any case, the pressing force should be set in accordance with the both parameters, but also with the output power of the generator.

When optimizing welding parameters, you start with a small pressing force and increase it until the necessary quality of the weld seam is achieved. After the optimization, the output power of the generator should remain constant.

The switch-on time t_{on}^{US} depends on the touchdown time, the touchdown distance and the pressing force. The ultrasonic can be switched on before the sonotrode is placed, during the placement or after the sonotrode has been placed on the molded part. With time-dependent switching on, you can choose all three options.

When switching on depending on the path, only the placement of the vibraating sonotrode is possible. With pressure-dependent switching on, you can choose from light touchi switching on as soon as the sonotrode touchs the molded part, to switching on only after the full pressing force has been reached.

When US welding thermoplastics, however, it is advantageous to switch on the generator only when the selected pressure is reached. When riveting, embedding and flanging, an vibrating sonotrode should be attached so that the molded part is plastificated more quickly and in good time.

The touchdown velocity of the sonotrode is determined empirically in tests, is normally from $0{,}5 mm/s$ to $50 mm/s$ and plays a decisive role in the welding quality. When riveting, embedding and flanging, you work with low placement velocity.

The welding time as it follows from (3.6) and (3.7):

$$t_{weld} = \frac{c_p^{plast} \cdot m_{top}^{plast} \cdot (T_{g,m} - T_r) \cdot x_{top}^{plast}}{S_{weld} \cdot G_{top}^{II}(T) \cdot \left(A_0^{US}\right)^2 \cdot f_{res}^{US}} \tag{3.11}$$

or

$$t_{weld} = \frac{c_p^{plast} \cdot m_{top}^{plast} \cdot (T_{g,m} - T_r)}{W_{gen}^{US} \cdot tg\delta} \tag{3.12}$$

depends on:

- output power of the generator (W_{gen}^{US})

- materials (G_{top}^{II}, ρ_p^{plast}, c_p^{plast}, $T_{g,m}$)

- size of the welding area (S_{weld})

- molded part thickness (x_{top}^{plast})

- switch-on time ($t_{on}^{US} = t_{off}^{US} - t_{weld}$)

- amplitude (A_0^{US})

- pressing force (F_{anp}^{US}) in (3.8)

and is usually determined empirically in test series. It is kept as short as possible, normally around of $(0.2 \div 1.5)s$, to avoid damage to the molding.

The sharp drop in elastisity modulus in the temperature ranges around of T_g and T_m (figures 3.1 a and 3.2), causes intense attenuation of US vibration energy on the way to the weld surface. In general, energy losses in semi-crystalline thermoplastics are higher than those in solid amorphous thermoplastics. Therefore US welding of semi-crystalline molded parts of the same shape as amorphous ones requires greater output power of the generator and greater amplitude so that the welding time for the two thermoplastics remains comparably short.

As equations (3.6) and (3.7) show, the basic material characteristics such as specific heat capacity, latent heat of glass transition and fusion, viscosity in the softened state affect the US welding parameters both directly and indirectly. Indirectly, they act by influencing the sound velocity and thus the supply of US vibration energy to the contact surface (melting surface). The latter is particularly important in far-field welding.

The distance of the sonotrode from the weld surface, which usually corresponds to the thickness x_{top}^{plast} of the upper thermoplastic part, distinguishes two welding regimes: near-field welding or direct welding (fig. 3.5 a) and far-field welding or indirect welding (fig. 3.5b).

Near field and far field designate two areas of the US field in the propagation medium with very different physical properties. It applies to the near-field area, $x_{top}^{plast} < \lambda^{US}$ i.e. an area in the immediate vicinity of the sonotrode, where strong, uneven interference is at work. It applies $x_{top}^{plast} > \lambda^{US}$ to the far field range, i.e. far away from the sonotrode, where interference effects no longer play a major role.

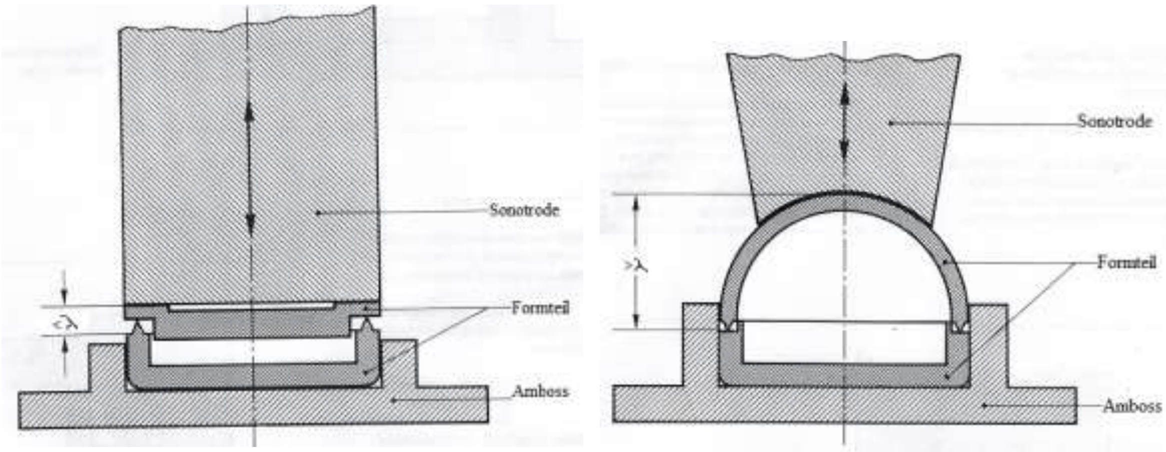

a **b**

Fig. 3.5. Examples of near field (a) and far field (b) welding

The boundary between the near field and the far field depends on the US wavelength $\lambda^{US} = \dfrac{c}{f_r^{US}}$ and the size of the radiating surface of the US source (sonotrode) [1].

Softening or melting the entire molded part during US welding and thereby distorting or even destroying it is not the purpose of US energy input in a welding process. The main task is to transport the maximum US vibrational energy into the contact zone at the weld surface, to plastificate, soften or melt the area of the upper molded part and the two thermoplastic molded parts through the softened material and through the melt respectively to stick together.

For this purpose, the contact surface of the upper molded part will be made extra rough or provided with unevennesses as energy directors (ED's) and with a different seam design (fig. 3.6).

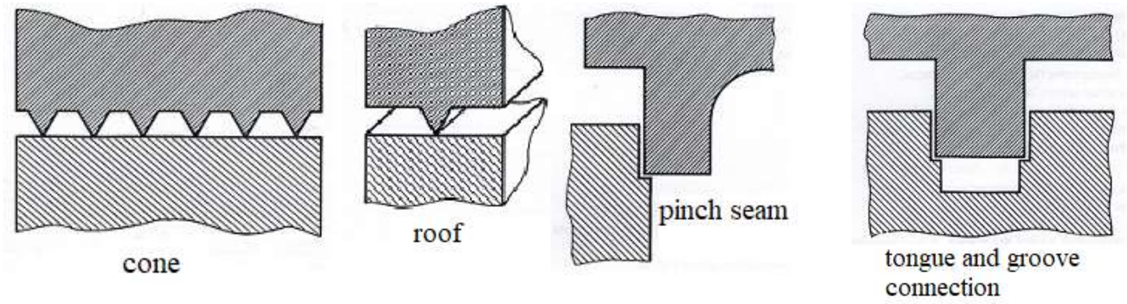

Fig. 3.6. Design examples of thermoplastic molded parts for US welding with various energy directors (ED's).

The ED's concentrate US energy at their peaks. These are also under mechanical stress σ_{ERG} due to the pressing force F_{anp} and elastic deformation ε_{el} of the upper molded part during US vibrations:

$$\sigma_{ERG}[MPa] = \frac{F_{anp}}{S_{ERG}} + G^{I} \cdot \varepsilon_{el}, \tag{3.13}$$

where S_{ERG} is the total area of all ED's, which is very reduced at the spikes.

The material, which is initially softened/melted at the spikes, is squeezed into the gaps by the pressure, fills these up and forms a weld seam when it solidifies again, which ensures a firm join between the two molded parts.

In order to achieve high quality of a US welded joining, the necessary prerequisites should already be created during the planning phase. Depending on the requirement for a welded joint, the construction must meet the following criteria among all other things:

- resilience of the weld
- water- and gas-tight welds
- aesthetic appearance
- absence of the melt leaked inside the molding.

In addition to the welding parameters discussed above, the final quality of the weld is influenced by the following factors:

- kind of material (Table 3.1)
- construction of molded parts
- location and design of contact surfaces
- design of ED's

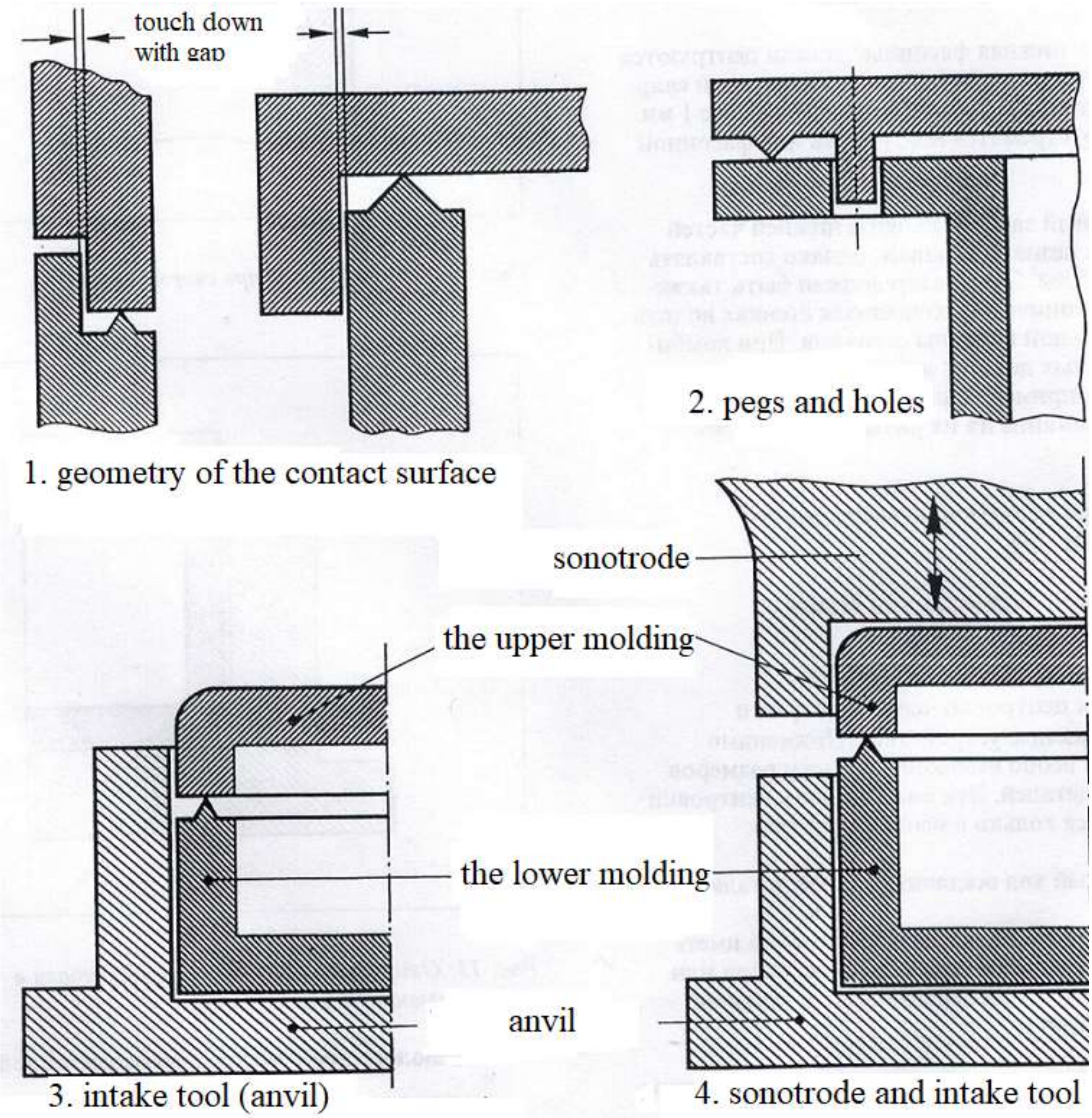

Fig. 3.7. Possibilities for centering molded parts.

- positioning and placement freedom of upper and lower molded parts
- adjustment of the sonotrode
- position in the intake tool (anvil)
- alignment of molded parts [21].

The ED's design and the seam geometries are adapted to the nature and construction of molded parts. In the case of pinch tongue and groove as well as all other tongue and groove or step welds, the upper molded part is pushed down by the pressing force on the vertical walls of the lower molded part (fig. 3.7).

This engenders additional frictional heat, which causes the two molded parts to be joined. Even with the same thermoplastics (the diagonal in Table 3.1), the production of molded parts in different processes such as pressure casting, extrusion, blowing leads to different properties and thereby affects their weldability. In order to ensure the joining such molded parts, US spot welding is used, the principle of which is shown in figure 3.8 on the right.

With **spot welding**, the molded parts do not require a special design of the welding surface. The sonotrode spike penetrates into the lower plate, melting it at the point so that the plastic collects in the parting line and ensures a spotform joining.

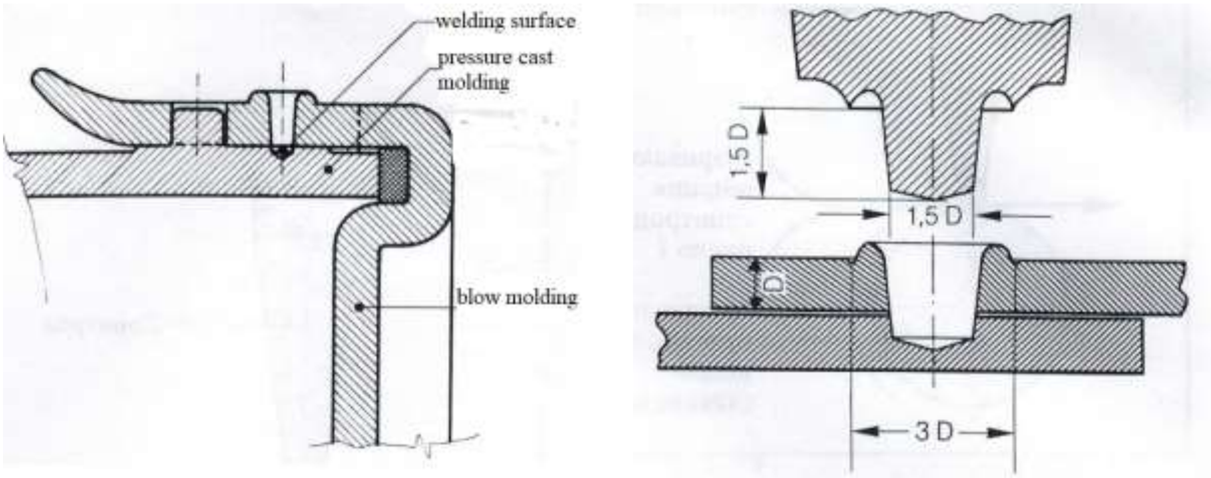

Fig. 3.8. Spot welding of thermoplastics with different properties (example and principle).

Spot welding is simple, quickly, conforming to shape, does not require ED’s and ensures safe, precise joining of molded parts, even with different properties that make conventional US welding difficult.

Other US joining methods for non-weldable thermoplastics include riveting and flanging, well-known in manufacturing. Thermoplastics can be joined to metals or other non-weldable materials by riveting and flanging.

The rivet, which was already produced during the manufacture of the lower molded part, is used during riveting in such a way that the rivet head (fig. 3.9), formed from the protruding pin through the sonotrode, securely fixes the upper component part. After riveting, the two parts no longer require an additional joining.

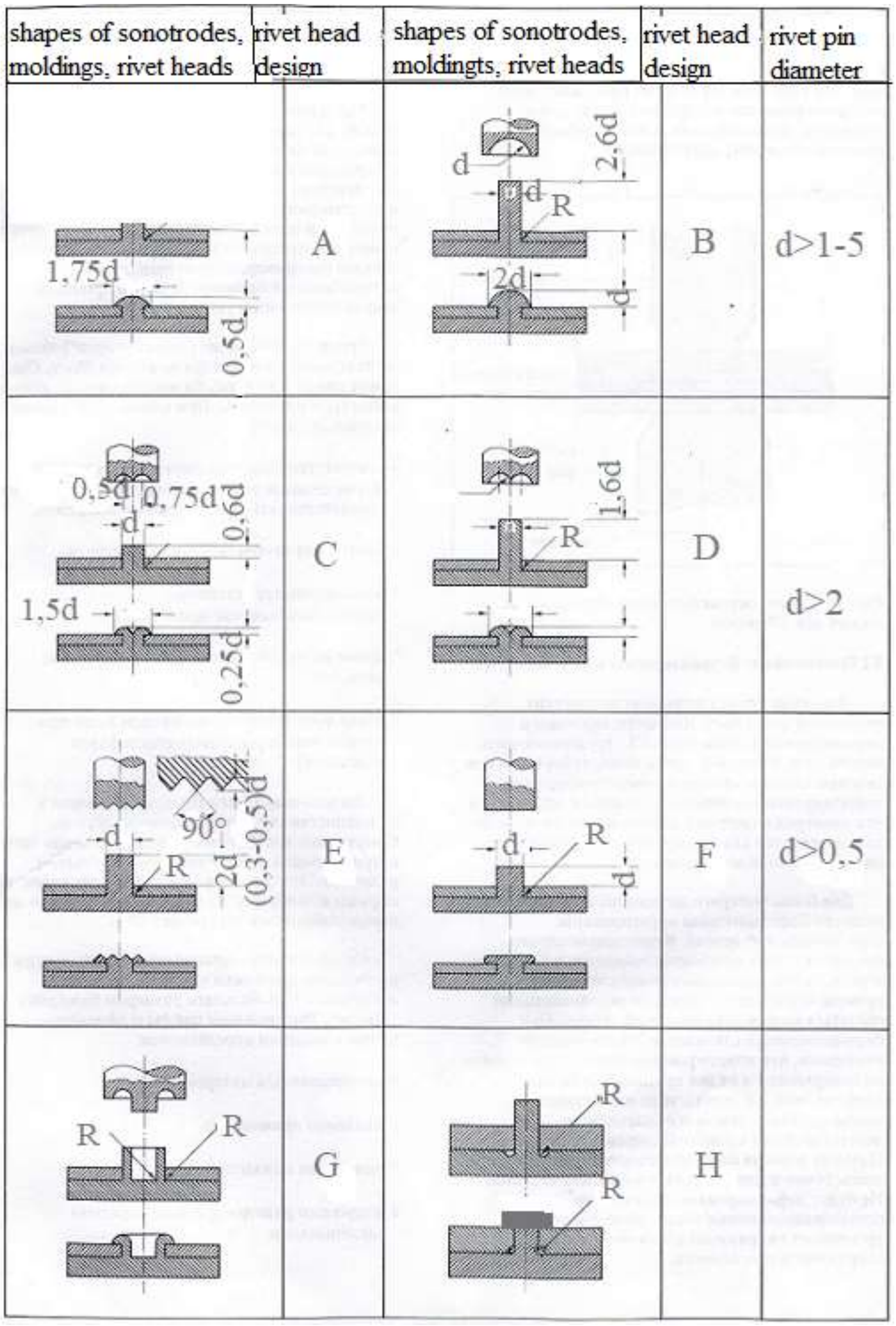

Fig. 3.9. Often used rivet head shapes and shank diameters.

In US riveting processes, the rivet pins can be formed into rivet heads as individual rivets or as several of them in one cycle. This creates a solid rivet joining that does not require any further attachment. Figure 3.9 shows details related to the riveting process.

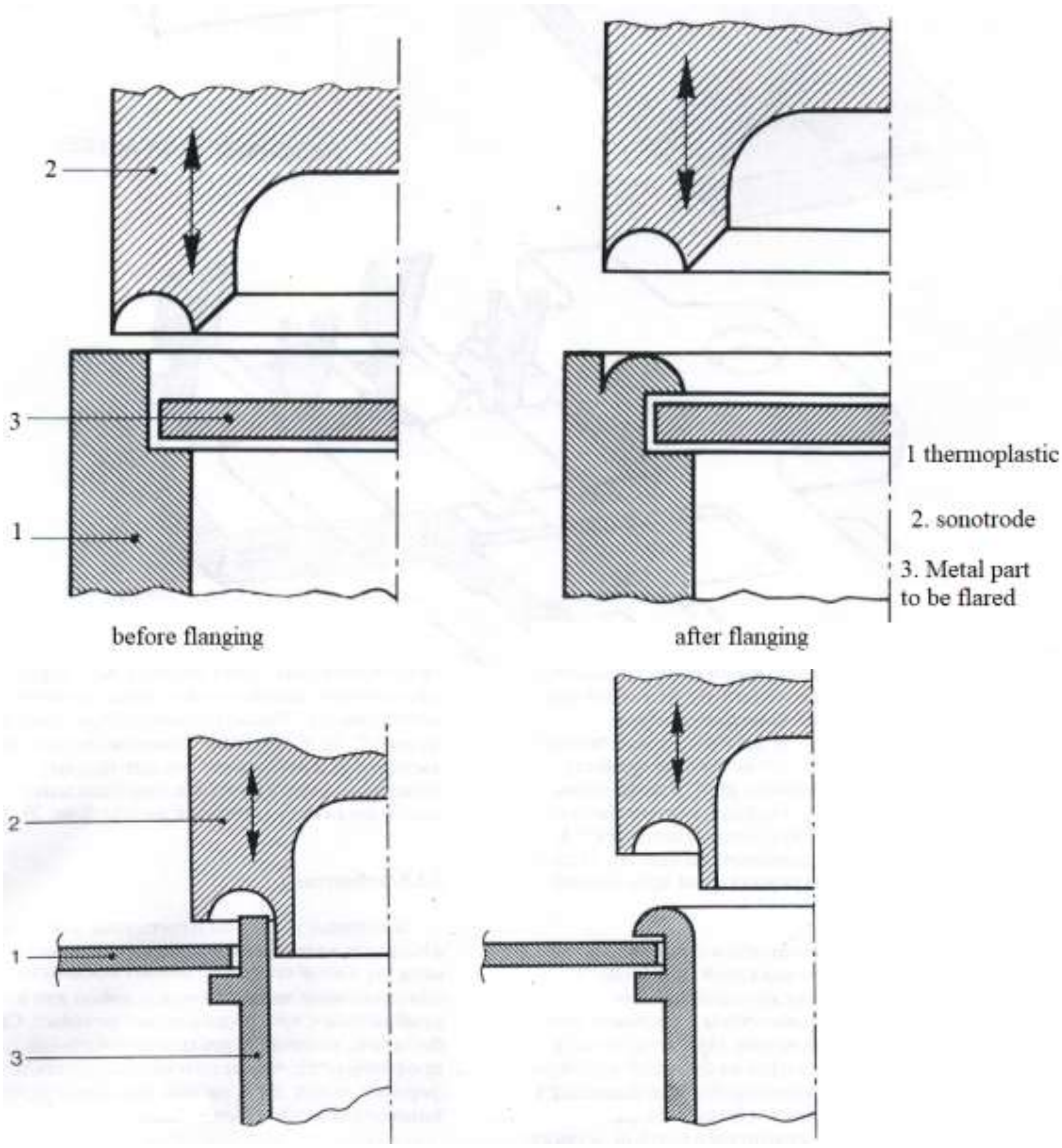

Fig. 3.10. Examples of forming during flanging.

With these joints, the mechanical US vibration energy is conducted through the sonotrode into the plastic, as is the case with US welding. This is plastificated as the temperature rises and shaped by the pressure of the sonotrode as a shaping tool.

Flanging works on the same principle of plastification and forming. It is used as an alternative to riveting when rivet pins are not available on components. The sonotrode is specially shaped on the end face side and can reshape the plastic part in such a way that it encompasses and fixes the second part (fig. 3.10). No energy directors are required for flanging. The US process enables the joining of dissimilar materials with the plastics and large-format forming.

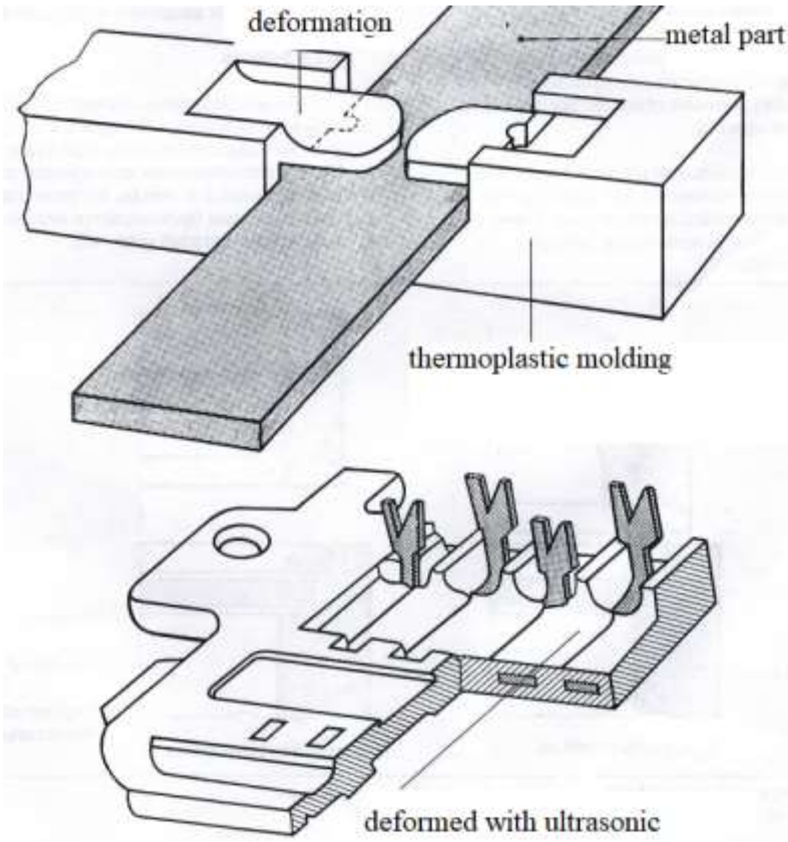

Fig. 3.11. Examples of joining in US impact method.

Joining of dissimilar materials with thermoplastics is also possible in a US process similar to flanging, the **impact-process** (fig. 3.11). In this process, the plastic, which has been plastificated by the sonotrode, penetrates under pressure into the gaps, grooves and holes provided in the non-specific component, so that an inseparable joint is created after the plastic has cooled and hardened.

Embedding metal parts in thermoplastics is a similar US process of inseparably bonding thermoplastics to dissimilar materials. The process is used for embedding threaded inserts, set screws, anchor bolts or other metal parts in the thermoplastic mold.

With special sonotrode combinations (fig. 3.12), several metal inserts can also be embedded in different contact levels in one cycle. The main requirement for product quality is tear and spin resistance. These are ensured by vertical and horizontal notches in metal parts (fig. 3.13), which are filled with plastificated plastic during US embedding. US embedding is performed at lower amplitudes to avoid cracking and destruction of the thermoplastic molded part.

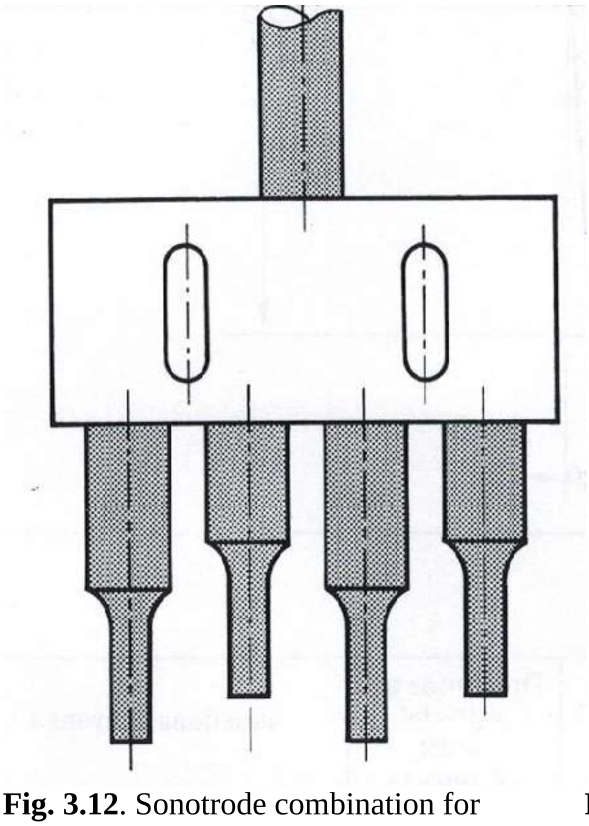

Fig. 3.12. Sonotrode combination for embedding metal parts at different contact levels.

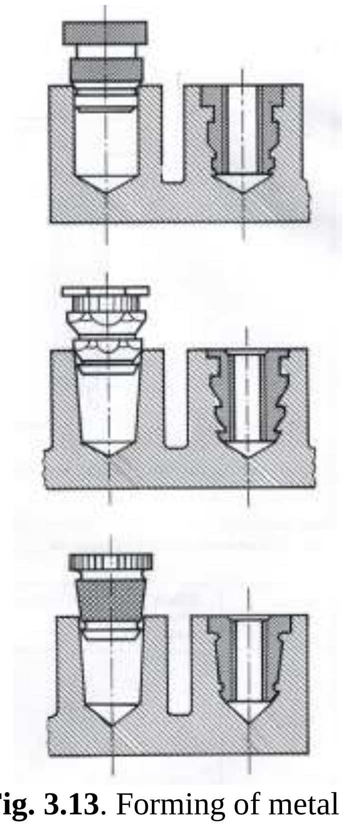

Fig. 3.13. Forming of metal parts and receiving holes in molded parts.

The US welding process is also used to stitch together flat textiles with thermoplastic fibers in an endless cycle (fig. 3.14). The connection is also made by softened or melted thermoplastic material of the fibers.

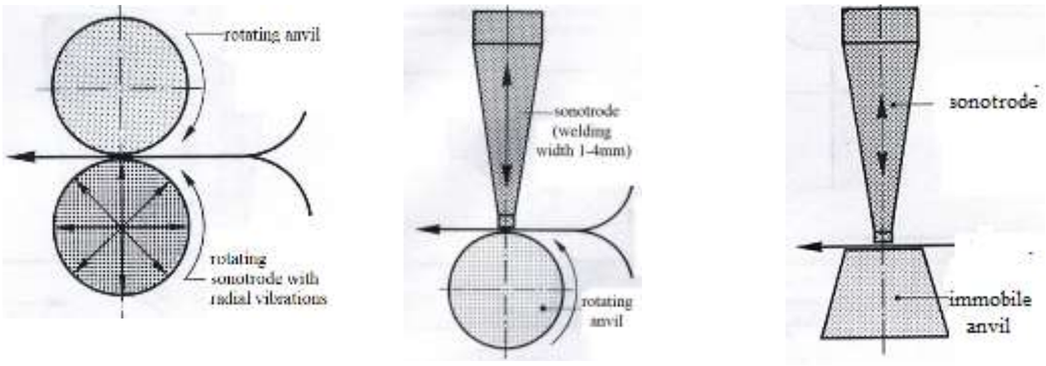

Fig. 3.14. Various possibilities of the endless seam welding process of textiles.

If one of the welding tools, sonotrode or anvil, is made in the form of a knife edge, such textiles can be cut cleanly in a likewise endless separating seam welding process. The edges of the cut are melted off so that no fraying takes place. The same works with US welding of thermoplastic films with cardboard and textiles with molded parts [22] etc..

4 Metal joining in the ultrasonic welding process

4.1 Basics

In the case of large generator outputs, the US joining of metals or metal alloys is even possible, even of those that are considered non-weldable in conventional welding processes such as electrode or arc welding.

US joining of metal parts differs significantly from US welding of thermoplastics. This is solely due to the different properties of the two materials. The term “welding” itself, in relation to the conventional method of joining metal parts, means the melting together of liquefied metal components at the contact line to a weld seam. The same principle applies to the joining of thermoplastics, as presented in the previous chapter.

The rapid softening or melting of thermoplastics occurs during heat production at the contact surface due to intensive internal friction in the amorphous molecular chain structure of the thermoplastics. The heat generated also remains concentrated at the contact surface because the thermal conductivity of plastics is negligible.

Metals, on the other hand, have properties that are unfavorable for their rapid heating: a much lower internal friction [23], apart from special cases in damping alloys, with $\tan\delta = \frac{G^{II}}{G^{I}} \approx 0$ at a loss modulus $G^{II} \to 0$ and a much higher elasticity modulus (storage modulus) $G = G^{I}$, a much higher thermal conductivity $\lambda\left[\frac{W}{m \cdot K}\right]$ compared to thermoplastics, an one magnitude order higher density $\rho\left[\frac{kg}{m^3}\right]$, a much higher melting temperature $T_m[K]$ for most metals and their alloys with comparable specific heat capacity values $c_p\left[\frac{J}{kg \cdot K}\right]$.

So, the energy production (3.6) in metals and the heating (3.7) of metals at the contact surface by US vibrations are much weaker than those of thermoplastics, while at the same time a higher energy requirement to reach the melting temperature. These characteristic differences actually exclude US metal welding as the conventional melting together of components of the two metal parts with the formation of mixed crystals at the contact zone.

4.2 State of research and technique

The joining of metal parts in a US welding process takes place despite the unfavorable conditions outlined above and has now been used intensively in various areas of technology for a long time, although the joining mechanisms were used up to the 1990s, at the time of the investigations at the TU Berlin on behalf of the company "Ultrasonic Steckmann GmbH" from 1999 [24] were still poorly or incorrectly understood and clarified.

The ultrasonic welding process for joining metal parts [25-35], especially in contact technology, has been studied and developed for around 70 years. Despite the large number of different investigations in this field over the years, mechanisms of ultrasonic joining of metal parts have not been clearly clarified, as also confirmed by the citation from the recent literature review [36] on this topic:

> „*The study of post-welding microstructure, the formation of any intermetallic compound at the interface and their effect on the joint strength, the presence of heat affected zone in the ultrasonically joined sheets has been explored but still, arguably the least understood.*"

B. Sanga, R. Wattal, D. S. Nagesh. "Mechanism of joint formation and characteristics of interface in ultrasonic welding", 2018 [36]

The basic results on this method were determined in the works by D. Stöckel

[37-39]. Here the structural investigations of welds of various ultrasonically joined metal pairings as well as adhesive strength measurements were carried out and joining mechanisms in a US welding process were discussed.

The **Adhesion** or the **cohesion**, a metallic joining through the interaction of the electron structures deformed on the surface of the metals to be joined, has been mentioned for the first time as a joining mechanism for US metal joining, with a clean metal surface and a tight contact being a prerequisite for this.

This mechanism was clearly proven as the main joining mechanism in 1999 [24] by scanning electron microscopic EDX analysis of the composition at the joining boundaries of the various metal pairings, whereby the assumption with the pure metal surfaces proved as redundant.

In the US welding process, two metal parts to be joined are pressed together by a pressing force and at the same time exposed to the high-frequency US vibrations oriented parallel to the contact boundary of usually $20kHz$ or $35kHz$.

The parallel application of the US vibrations to the contact surface, in contrast to US welding processes for thermoplastics, is due to the much lower internal friction in metals and thus much lower heat production. When joining metal using US welding, the two metal parts rub against each other at the contact surface with a large shearing force, which produces more heat than when US vibrations are normally applied.

Due to the high-frequency shearing force, oxide layers and impurities on the metal surfaces are destroyed, crushed and thrown out of the joining surface or at least transported to the edge [24, 40, 41]. Mechanical interlockings and entanglements due to drastic plastic deformation and the turbulent flow of the material into one another have been identified as secondary joining mechanisms in light microscopic examinations of the contact boundary [24].

The combination of three factors in the US welding process – static normal pressure, high-frequency vibration shearing force and moderate temperature increase due to the friction of the two metal surfaces in the contact area – enable close contact of both metal parts and the interaction of their electron structures, which ensures a strong and durable joint.

Sometimes the joining mechanisms for conventional metal welding are simply transferred to US metal joining [42]. The phenomena typical of arc welding at the contact boundary are speculative and not experimentally proven:

1. Melting of the contact surface: joining by mixing metals in the melting zone, as in resistance welding, provided that at least one of the metals to be joined rises in temperature above the melting point.
2. Diffusion: joining by mixing the metals to be joined at the atomic level, their ability to form a chemical compound or a mixed crystal, large diffusion coefficients, high temperature, sufficient time are required.

So, formation of welds by melting together and mixing of metal parts to be joined is still considered as the joining mechanism in US metal joining up to now, despite the basics outlined above and the investigations in [24, 37-39].

The term “welding” itself seems to mislead in this regard, as probably happened to the author in [42], because it points to conventional welding techniques based on melting together and forming a weld seam.

However, it can also be concluded from many other published research results that in the top list the first mechanism in US metal joining is unrealistic and even undesirable, because melting togethe leads to microstructural changes or formation of brittle intermetallic compounds, which significantly weaken the weld.

The diffusion mechanism is also out of the question in view of the usually low temperatures in the contact zone of about $(0,3 \div 0,5)T_m$ (T_m is the melting temperature) and a very short US exposure time every second, although the increase in the diffusion coefficient and an acceleration of the diffusion by ultrasonic vibrations are possible.

In the US welding process, plastic deformation of metal parts to be joined occurs [37-40, 43, 44], which is also considered as one of the joining mechanisms. The degree of deformation depends on the adjustable ultrasonic parameters, such as the US energy supplied by the generator, the US vibration amplitude and the US exposure time, as well as the profile of the tool surface and the shape and material properties of the metal parts to be joined.

In a normal contact welding process, the deformation of freely placed parts can be insignificant (up to 5% [38]). Much larger deformations are observed in the contact zone due to the high-frequency frictional movement of the metal parts to be jointed [37, 38].

This stress on the metal surfaces leads to a wavy or, in extreme cases, a whirling profile of the contact boundary and mechanical interlocking of the pairing components. This plays a positive role in bond strength in US metal joining. On the other hand, larger deformations can lead to the formation of micro and macro cracks or even to total material destruction. Such metal damage is to be avoided in US metal joining.

Despite this complex influence on the joint quality of ultrasonically joined metal parts, there are only a few experimental investigations into the US effect on the deformation behavior and on the deformation mechanisms of metals in US welding processes [46]. Most can be found with theoretical models from [47], such as e.g. the metallo-thermomechanically coupled model [48].

In other works, microstructure investigations of metals are carried out after general ultrasonic treatment [49, 50]. In particular, earlier stages of plastic deformation associated with the generation, multiplication and distribution of dislocations are investigated.

The advantages of the US welding process are obvious:

- no special surface cleaning
- no protective atmosphere
- low energy consumption
- short exposure time
- possibility of fully automating the welding process and integrating it into other manufacturing processes or systems
- possibility of joining metals that cannot be welded using conventional methods
- possibility to connect thin and thick, small and massive, round and flat metal parts.

Despite these advantages, metal joining using the US welding process was slow to gain acceptance in production engineering. In the beginning, such a development was caused by the lack of powerful US generators, which could ensure the US joining of large parts in a reproducible manner.

This also led to the focus of research being shifted to the development of ultrasonic devices in the 1980s and 1990s [51-53]. Sufficiently powerful ultrasonic devices and corresponding US procedures have been developed at present. However, research into physical relationships, the joining mechanisms in US welding processes and the behavior of metals under the influence of ultrasonic has lagged behind.

The aim of this experimental research, carried out on behalf of “Ultrasonics Steckmann GmbH”, is to study the structure and composition of the contact zone of ultrasonically joined and the structure of ultrasonically stretched metal parts and to bring the mechanisms of US metal joining up for discussion again, as well as the plastification of metals in the US welding process is not only to be regarded as one of the important joining mechanisms, but also as another possibility of ultrasonic metal processing.

4.3 Experimental

Various metal pairings were selected for US joining (Table 4.1), which are considered as difficult (copper-copper) or non-weldable (copper-aluminium, copper-steel) in conventional electrode or arc welding processes.

Table 4.1. Metal pairings for US joining tests, shape and purity of their components as well as their melting temperatures (T_m) and stretching degree ε during US joining calculated according to formula (5.1).

No.	lower part	upper part	pairing
1	aluminum plate $2{,}5mm$ thick, purity $99{,}9\%$ ($T_m = 659°C$)	copper wire, $\varnothing 3{,}2mm$, purity $99{,}9\%$ ($T_m = 1083°C$), $\varepsilon = 500\%*$,	$Al - Cu$
2	copprr platte $1mm$ thick, purity $99{,}9\%$ ($T_m = 1083°C$)	aluminum plate $1mm$ thick, purity $99{,}9\%$ ($T_m = 659°C$), $\varepsilon = 300\%$	$Cu - Al$
3	brass plate $1{,}5mm$ thick ($CuZn37$, ($T_m = 920°C$) coated ($0{,}05mm$ thick) with fine silver Ag ($T_m = 962°C$)	copper wire, $\varnothing 3{,}2mm$, purity $99{,}9\%$ ($T_m = 1083°C$), $\varepsilon = 80\%$	$Cu - Ag$ $Ag - Zn$
4	steel disc $1{,}3mm$ thick in its technical condition without any surface cleaning, $T_m = 1540°C$)	copper wire, $\varnothing 3{,}2mm$ purity $99{,}9\%$ ($T_m = 1083°C$), $\varepsilon = 300\%$	$Fe - Cu$
5	copper plate $1mm$ thick, coated ($0{,}02mm$ thick) with hard silver $AgCu3$ ($T_m = 938°C$)	copper wires, $\varnothing 0{,}05mm$ ($T_m = 1083°C$)	$Ag - Cu$
6	brass plate $0{,}5mm$ thick ($T_m = 920°C$), coated ($0{,}01mm$ thick) with fine silver Ag ($T_m = 962°C$)	copper wires, $\varnothing 0{,}05mm$ ($T_m = 1083°C$)	$Cu - Cu$ $Cu - Ag -$ $Ag - Zn$
7	copper plate $0{,}5mm$ thick ($T_m = 1083°C$), $\varepsilon = 110\%$	copper wire, $\varnothing 3{,}2mm$, purity $99{,}9\%$ ($T_m = 1083°C$)	$Cu - Cu$
8	copper wires $\varnothing 0{,}3mm$ in bundle ($T_m = 1083°C$) with one another		$Cu - Cu$

The joining of the selected metal pairings or the stretching of metal samples was carried out using a $3kW$ US metal joining machine (fig. 4.1 a). The construction of the US machine is shown schematically in figures 4.1 b, c.

Hardened steel was used as the material for the cone-shaped sonotrode. The sonotrode had the resonance frequency $f_r^{US} = 20kHz$ (wavelength $\lambda^{US} = 15mm$) and an amplitude $A_0^{US} = 30\mu m$. These mechanical vibrations were introduced into the upper of the metal parts to be joined in the horizontal axis (figures 4.1 b, c) by lowering the sonotrode with a pneumatically generated pressure of $6bar$ onto the surface of the upper part.

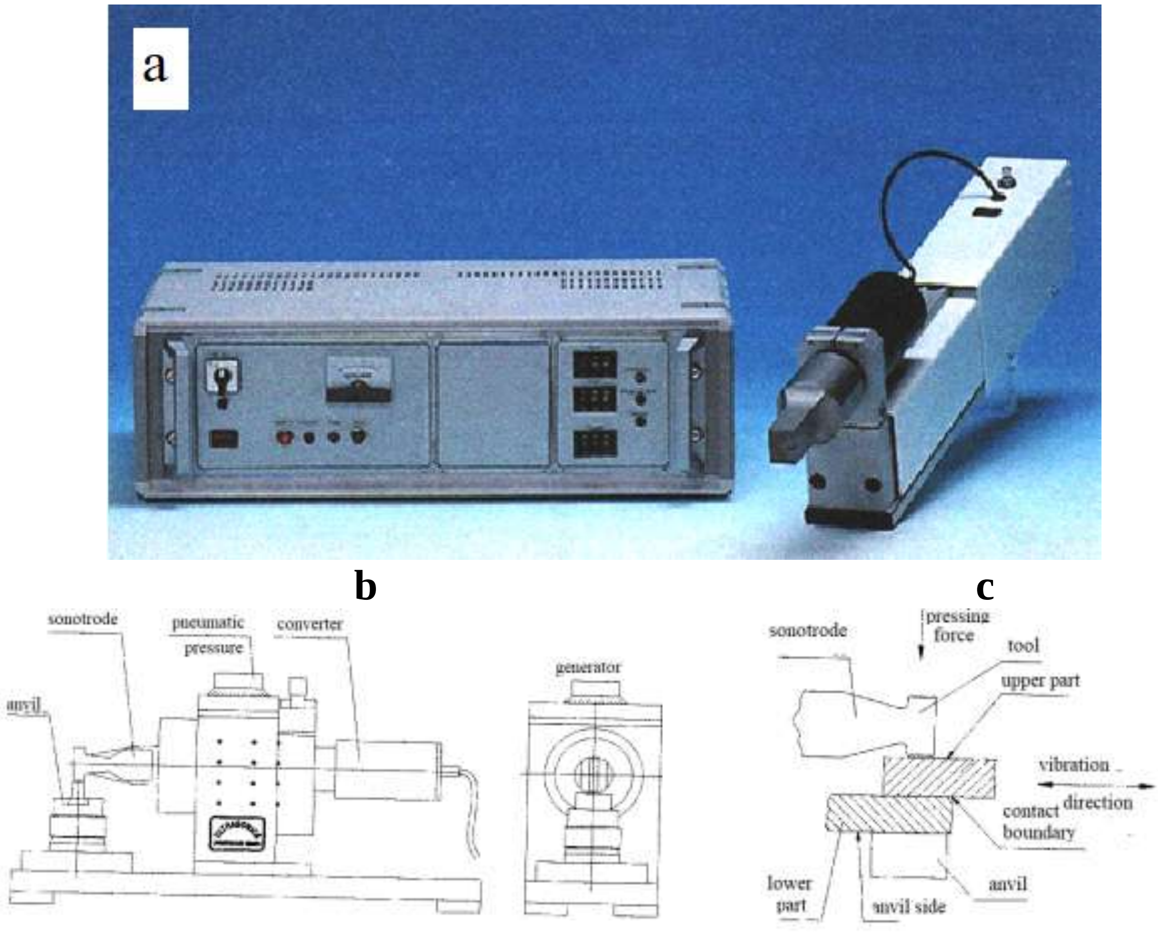

Fig. 4.1 a-c. Photo of the ultrasonic welding machine with an up to $3kW$ powerful generator (**a**), schematic drawings of its construction (**b**) and the joining instruments (**c**).

When joining compact metal parts (Table 4.1, no. 1-4, no. 7), the sonotrode surface had eroded wave corrugation with a period of $1{,}8mm$ perpendicular to the vibration axis. The anvil surface had eroded cross corrugation.

When joining wires (Table 4.1, no. 5, no. 6, no. 8), they were held in place laterally by a mold. The sonotrode entered this mold with both the sonotrode and the anvil having fine eroded corrugation. The power consumed by the US generator from the electrical grid was $3kW$. The welding time was $(0,3 \div 3)s$.

The influence of the grain structure during US joining or US stretching was examined using a light microscope (*LM*) on sanded, polished and etched sample surfaces. All samples were cut perpendicular to the US vibration direction from the joined place (contact zones) or from the stretched wire in a cutting machine. To examine the effect of sonotrode corrugation on the surface of the upper part, a cut of sample 1 along the vibration direction was also examined microscopically.

Distribution of components within the contact zones of the metal pairings and the possible diffusion processes constituting the diffusion transition zones were examined on the same cut samples using energy-dispersive X-ray spectroscopy (*EDX*) in a scanning electron microscope (*SEM*).

The EDX is based on the fact that the components in the surface of the metal sample bombarded by high-energy electrons in the SEM emit their characteristic (K_α) X-rays with a wavelength determined for each component.

The ratio of the radiation intensity of individual components to the total radiation intensity gives very precisely the concentration of individual components in a metal sample, which is the basis for the compositional analysis of metal alloys.

If the detector is set to the characteristic wavelength (window) of a one of the components, the distribution of this component in the surface can be observed immediately on the SEM image as brightly illuminated areas, while the areas with other components or with unknown extraneous elements remain dark. The window method was used here to verify component mixing through their diffusion in the contact zone.

4.4 Structure of the contact zone in metal pairings

The overall EDX image of a surface in the SEM is created when recording the complete X-ray spectrum without a window filter. Such an SEM image of the contact zone sample 1 on a cut along the vibration axis of the sonotrode is shown in figure 4.2 a.

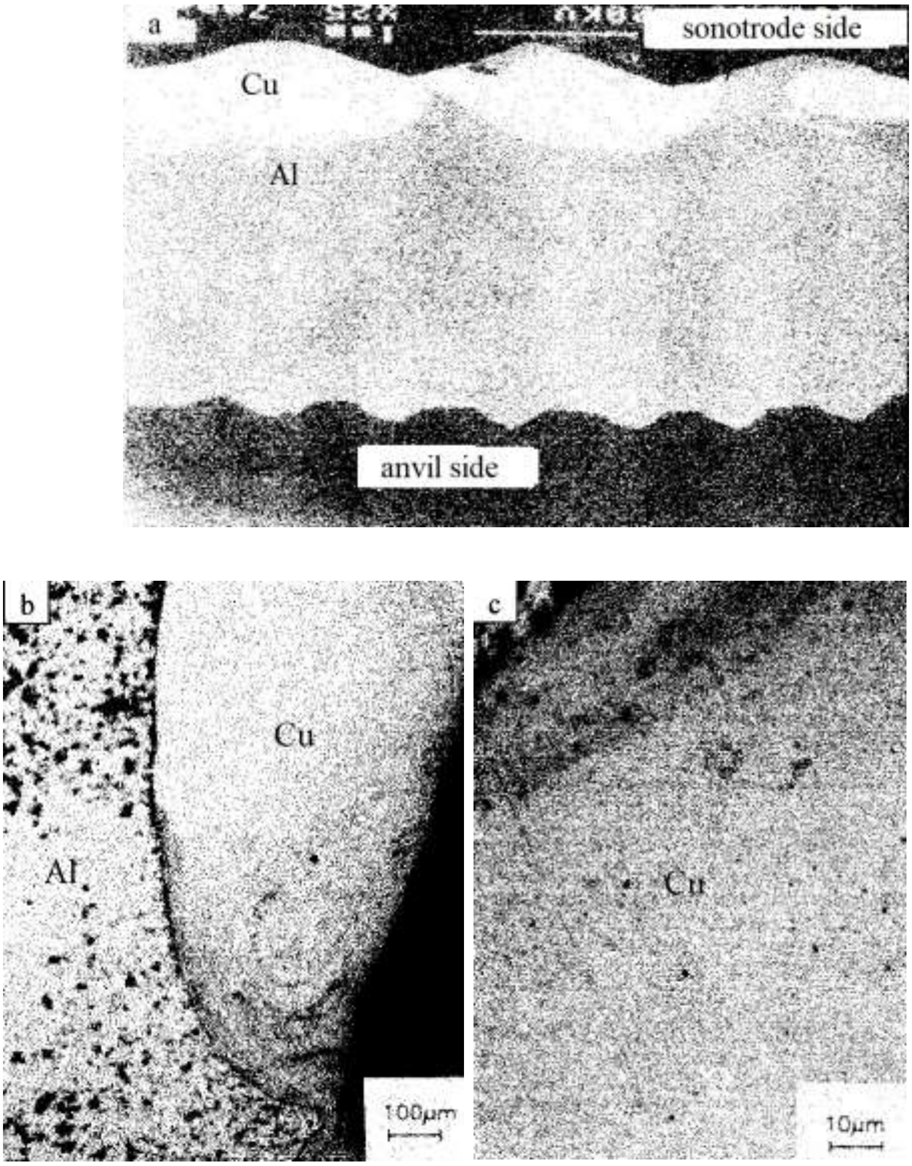

Fig. 4.2 a-c. Profile of the contact boundary on the sample 1 cut along the vibration axis (a, SEM). LM-micrographs of the $Al-Cu$ contact boundary and of structureless Cu surface (**c,** upper left the contact boundary).

The surface of the Cu upper part is imprinted to a wave form with the wavelength of $1.8mm$ of the sonotrode corrugation. The Cu wire has been crushed into a thin layer on the surface of the Al lower part.The deformation of the upper part is more than 500% (see the calculation formula (5.1)). The light microscopic image (figures 4.2 b, c) of the etched surface shows traces of the turbulent plastic flow of the copper in the contact zone.

The grain boundaries can hardly be seen on the LM image (fig. 4.2 b). This is due to strong metallographic texture, grain orientation equalized during plastic flow. With the turbulent plastic flow of the metal, it is even possible that the individual fractions of the metals to be connected are enclosed in one another.

The $Cu-Al$ contact boundary has a wavy structure shifted to half a period from the tool ripple wave on the Cu surface. This irregular and displaced wave can be explained as follows. The material of the Cu upper part is displaced into the vales of the corrugation by the wave crests of the tool, which exert maximum pressure on the surface of the upper part. Through this intense turbulent flow, the maximum pressure is transferred to the surface of the Al lower part in the peak areas of the corrugation wave, forcing the material of the lower part up towards the valley areas of the tool corrugation with such a force that the aluminum even pushes up through the Cu sheet on its surface (fig. 4.2 a, above right).

Despite the intense plastic flow of the copper and the low melting temperature of aluminum, no features of the crystallized melt in the contact zone can be detected in the light microscope **(**figures 4.2 b, c). The melting of metal pairing components at the contact interface would have led to the mixing of these metal components, which do not show any mixed crystals at all, but only various intermetallic Hume-Rothery phases on their equilibrium $(Al-Cu)$ state diagram and to the formation of a weld seam. The contact boundary thus remains sharp along its entire length without any trace of component mixing or a diffusion transition zone (figures 4.3 a, b).

The EDX microanalysis of the composition of the joined $Al - Cu$ metal pairing shows a sharp boundary between the joined metal parts (fig. 4.3 a, b) where no component mixing, either by melting or diffusion, is observed. On the other hand, a step (points marked with arrows in figures 4.3 a, b) with a height of about $3 \mu m$ in the surface shows how the two metals adapt to one another through plastic deformation at the contact surface.

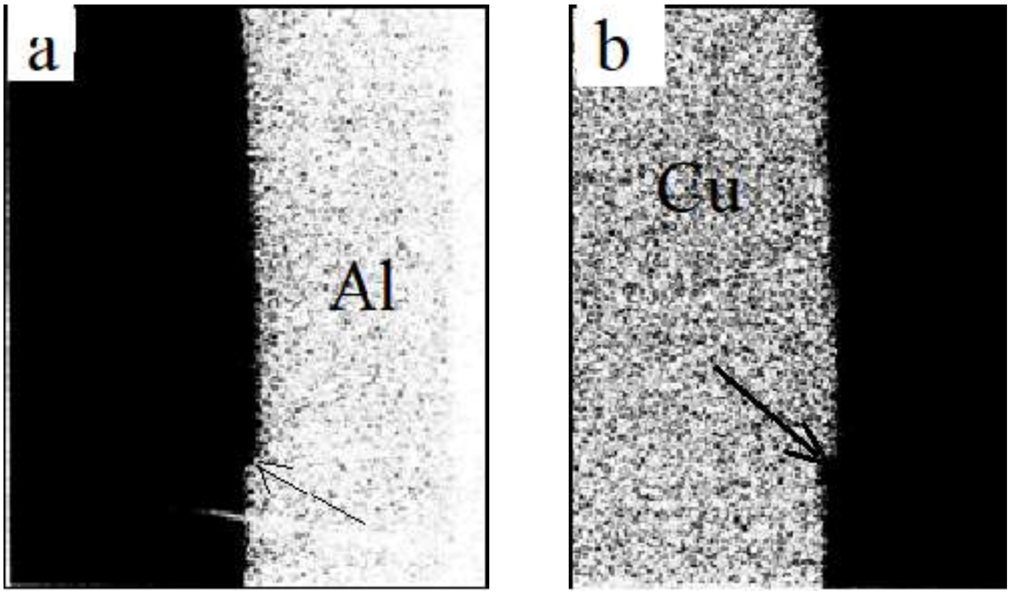

Fig. 4.3 a, b. SEM images of the $Cu - Al$ contact zone sample 1: Al window, (a), Cu window (b). The arrows show the same step at the contact surface. The cut here is perpendicular to the vibration direction..

Figures 4.3 a, b represent the images of the $Al - Cu$ contact boundary in the $Al\ K_\alpha$ $-$X-ray (Al window) and $Cu\ K_\alpha$ $-$X-ray (Cu window), respectively. Accordingly, the Al pairing component is bright in the Al window and the Cu pairing component is brightly lighted in the Cu window, while the other components remain unlighted (black).

Some diffuse contrast at the contact boundaries is due to electron beam cutting off at these boundaries, resulting in asymmetric intensity distribution and thereby diffuse contrast around ca. $0{,}2 \mu m$ at the contact boundary. For these reasons it is difficult to draw any conclusions about the local melting and amorphization in this boundary region. Such amorphization was detected at the interface of $(0{,}002 \div 0{,}02)\mu m$ in an ultrasonically joined Al oxide/Al composite using transmission electron microscopy (TEM) and SEM microanalysis [54].

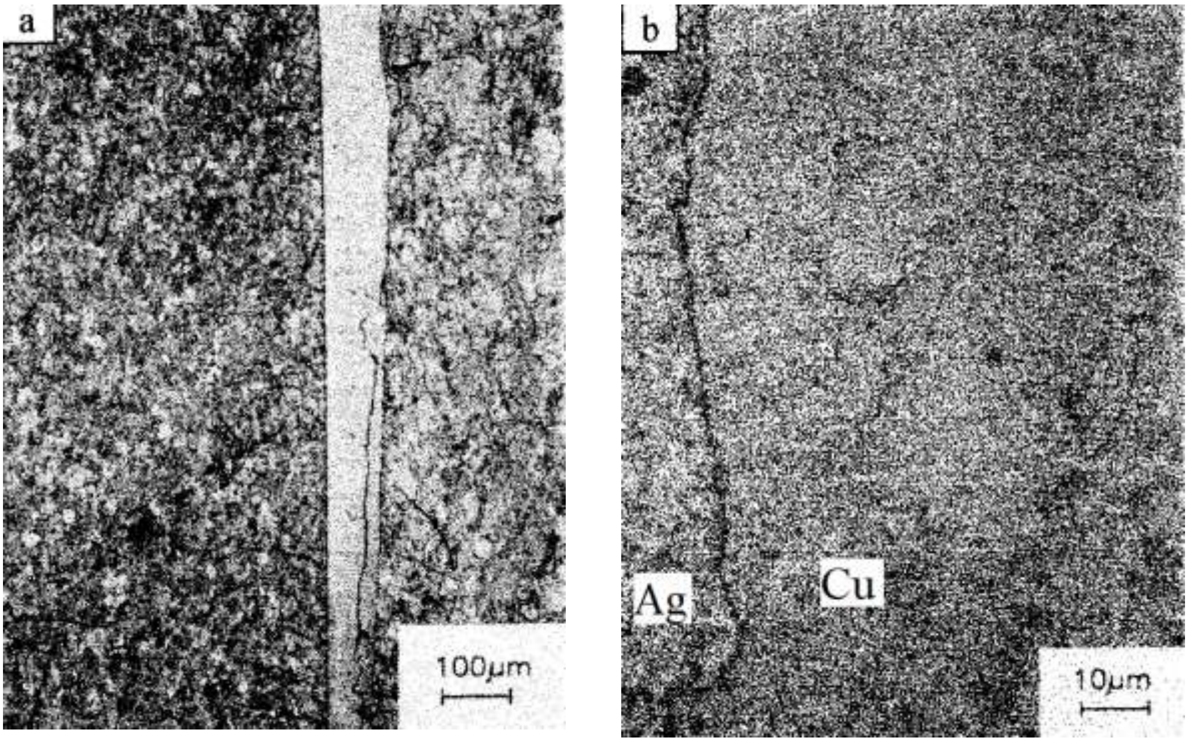

Fig. 4.4 a, b. LM-micrographs of the contact zone sample 3: $CuZn37-Ag-Cu$ (a) and $Cu-Ag$ (b).

The results obtained from the junction at the $Al-Cu$ contact boundary of US joined pairing components sample 2 are similar to those described above and support the conclusion that there is no merging or mixing of malting components through their diffusion at the contact interface in the US joining process.

In contrast to sample 1, the corrugation wave of the sonotrode embossed on the surface of the Al upper part (sample 2) is not transferred to the contact surface of the Cu lower part. This contrast is due to the difference in hardness and the temperature dependence of the hardness of copper and aluminum, so that the soft aluminum cannot exert by its plastic flow enough pressure on the surface of the harder copper to print it in a wavy manner.

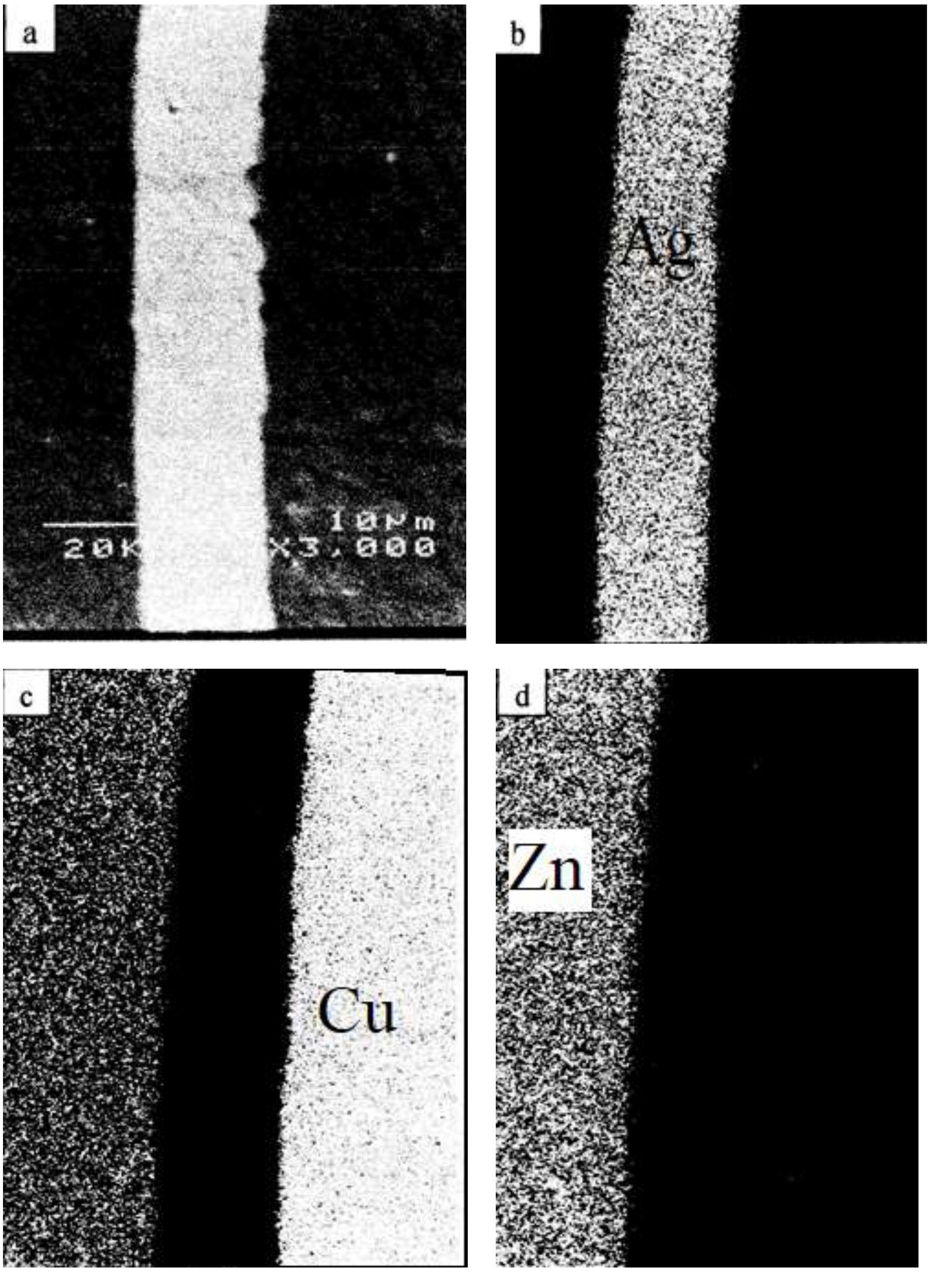

Fig. 4.5 a-d. SEM images of the $CuZnAl-Ag-Cu$ contact zone Sample 3: total radiation (a), Ag window (b), Cu window (c), Zn window (d).

In the next test, the $CuZn37-Ag-Cu$ contact boundary (sample 3) was examined (figures 4.4 a, b). This boundary is also sharp, without any trace of weld seam formation. The grain structure is the same at both contact interfaces and in the volume of two metal parts. Only a few interlockings between Ag and Cu pairing components can be observed.

The EDX microanalysis (figures 4.5 b-d) shows neither the mixing of pairing components in a molten weld nor their diffusion into each other. This applies to the two contact boundaries: for the $Cu-Ag$ one created by ultrasonic joining and for the $CuZn37-Ag$ boundary existing previously (the brass coated with fine silver).

The Ag and Cu windows show no diffusion between the upper part of the copper wire and the silver layer (figures 4.5 b, c). Likewise, no diffusion of silver into the brass in the lower part or of zinc and copper from the brass into the silver layer can be determined on the same Ag, Cu and additionally the Zn windows. Since brass contains both copper and zinc, it remains light gray both in Cu and in Zn windows.

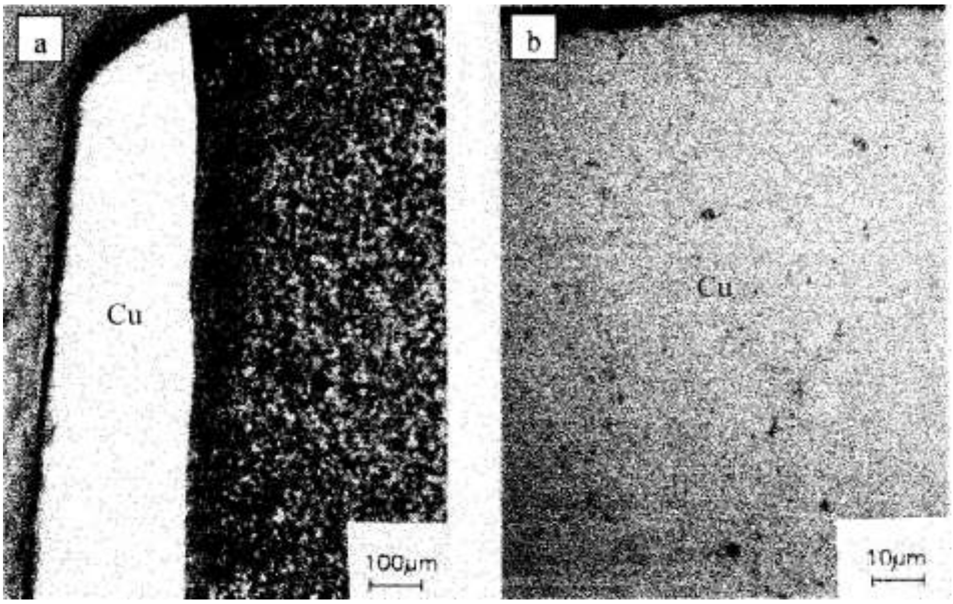

Fig. 4.6 a, b. LM-micrographs of the $Fe-Cu$ contact boundary of sample 4 (a, bright on the left is Cu) and Cu polished surface (b).

The steel-copper contact boundary of sample 4 exhibits the same properties. It is sharp (figures 4.6 a and 4.7 b), although not flat. Despite the unevenness, it shows no traces of weld formation or diffusion of Cu and Fe atoms between the upper and lower parts (figures 4.7 b, c). The etched surface of the upper part crushed on the steel disk is completely structureless because of the large plastic deformation (above 500%).

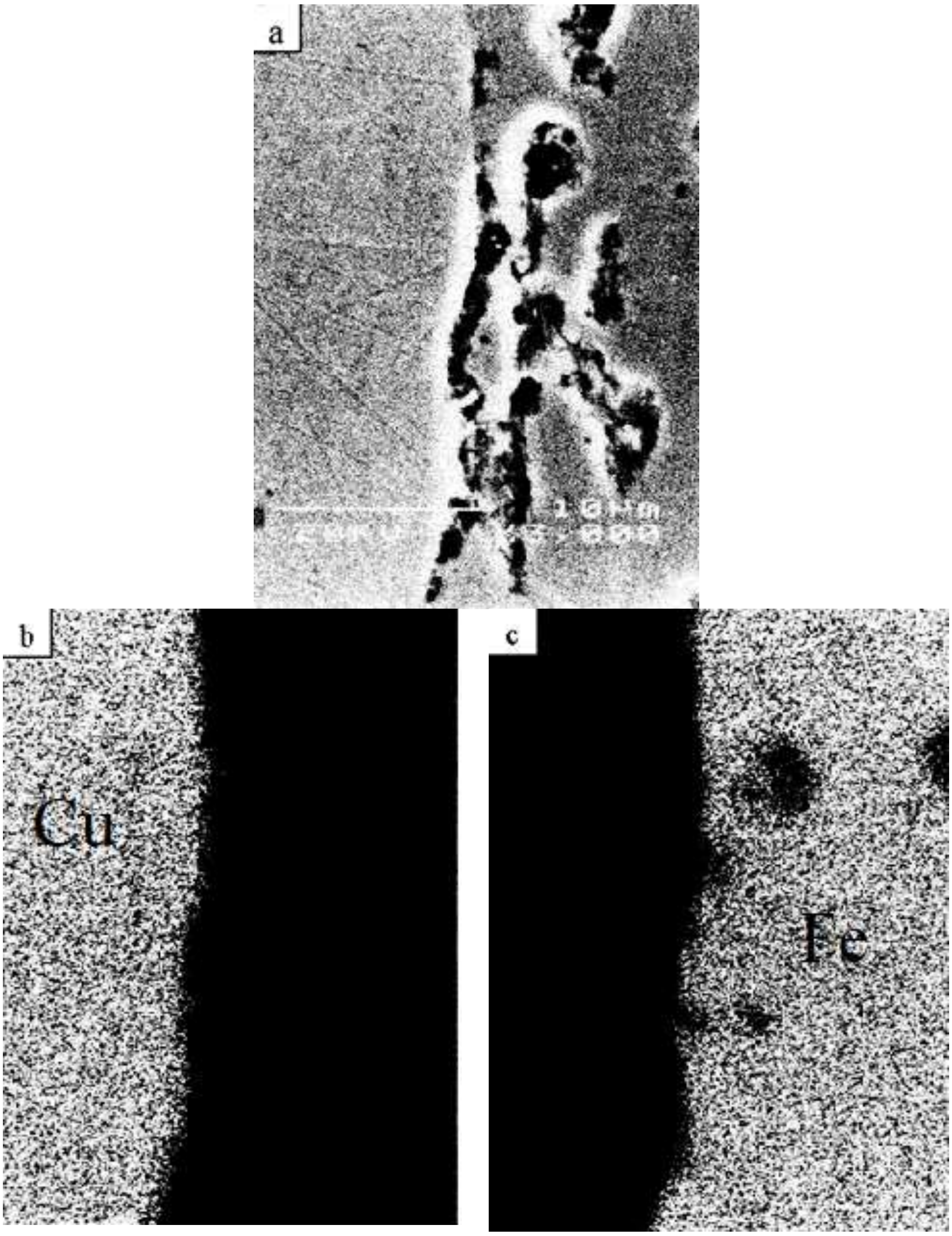

Fig. 4.7 a-c. SEM images of the $Fe-Cu$ contact zone sample 4: total radiation (a), Cu window (b), Fe window (c).

The unevennesses are due to inclusions on and under the surface of the steel disk (fig. 4.7 a, right). Most of them are ferrous (Fe oxides, Fe carbides) inclusions, which do not differ in the Fe window against the iron background and are therefore not visible. The few dark inclusions do not contain iron and are impurities of some kind.

The constitution of the steel disc is irrelevant here. It is only relevant that the inclusions escaping onto the surface of the steel disc at the contact boundary are abraded by the US vibrations and thrown away, resulting in a clean adhesive joint between the two parts. The abrasion is not uniform due to the different hardness of the inclusions and the steel matrix, which on the one hand makes the contact boundary uneven, on the other hand enlarges the contact surface and thereby makes the adhesive bond stronger.

So, also here as in all EDX investigations in the SEM, no traces of oxygen from the oxide layers or other contamination of the contact boundary were detected. However, because of the small amount of oxygen from the thin, destroyed surface oxide layers, it is not possible to assess whether the oxide residues and contaminants have been thrown away from the contact surface or are included in the interface material.

A pairing of the same metals ($Cu - Cu$) represents sample 7. The test is interesting because of the fixed connection of two metal parts of different shapes. The round wire as the upper part makes contact with the planar copper plate as the lower part at one line only. The pressure of the pressing force on the line is enormous, which leads to strong plastic deformation ($\varepsilon = 110\%$) of the lower part.

The LM images (figures 4.8 a, b) clearly show a sharp contact boundary. In some boundary areas, fragments of the metals to be joined are observed (fig. 4.8 a). EDX microanalysis shows that these are the particles of pure copper. Maximum destruction takes place at the boundary edges (fig. 4.8 b). At this relation the thickness of lower part ($0,5mm$) to the diameter of Cu wire ($3,2mm$) as the upper part, the lower part is mostly deformed. The metal of the lower part flows away from the contact zone to its edges, resulting in a “pancake-shaped” grain structure of the lower part, i.e. a strong metallographic texture (fig. 4.8 a, left), while the round upper part is hardly deformed (fig. 4.8 a, uniform grains on the right). Such an alignment of metal parts increases the contact area, creating an even stronger cohesive joint between the two metal pairing components.

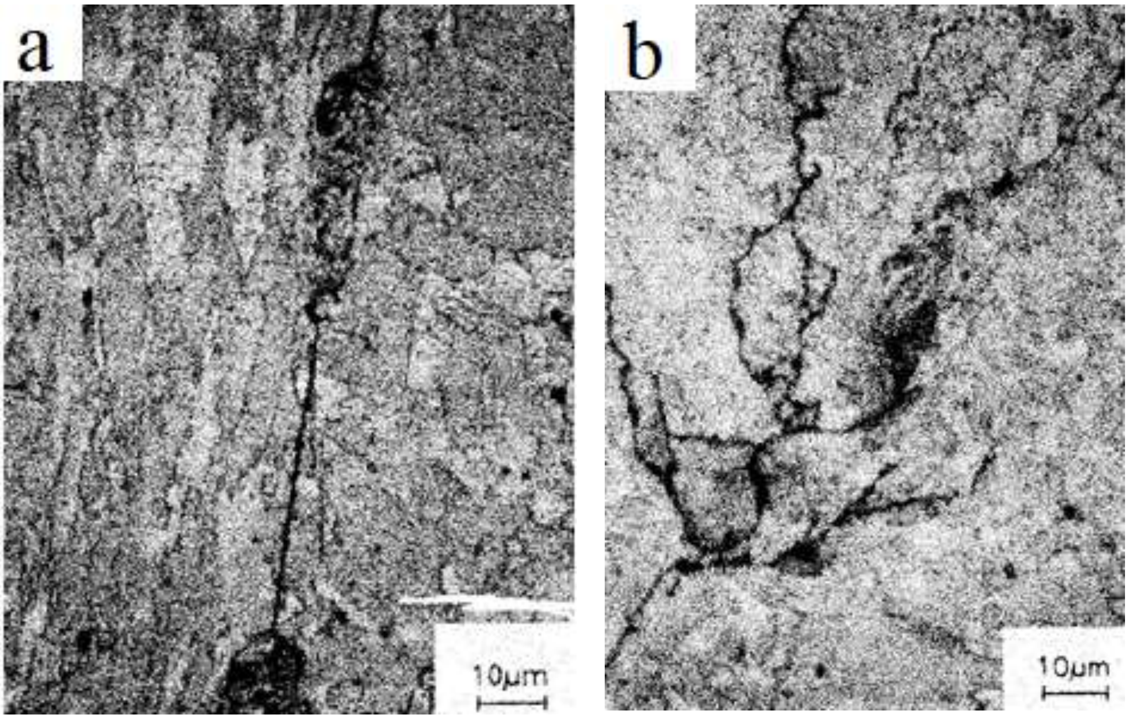

Fig. 4.8 a, b. LM micrographs of the surface sample 7 (lower part on the left, upper part on the right): $Cu - Cu$ joint boundary with enclosed Cu fracture particles in the middle (a) and several microcracks at its edge (b).

The LM images show here, too, that the grain structure in the boundary area does not differ from the grain structure in the metal volume. The grains of both metal parts are cut through the join boundary and there are no grains grown through the boundary.

This proves that neither primary recrystallization – grain enlargement due to their coalescence like that at growing of the martensite crystals [4], nor secondary recrystallization – grain reduction due to nucleation and growth of new grains within the coalesced grains, are caused by ultrasonic. All observed changes in the grain structure in the metal parts are only due to their plastic deformation.

Due to the continuing vibrations of the sonotrode, either the metal connections created by cohesion (connecting bridges) or the metal itself in the joining area are repeatedly destroyed. This leads to multiple microcracks and fractures, as well as crushing of the metal parts to be joined at the contact interfaces (figures 4.8 a, b) and weakening of the join strength. The observed metal fractures in the interface also indicate that the cohesive forces are not smaller than the strength of the grain boundaries in the bulk of the metal where the fracture appears to occur.

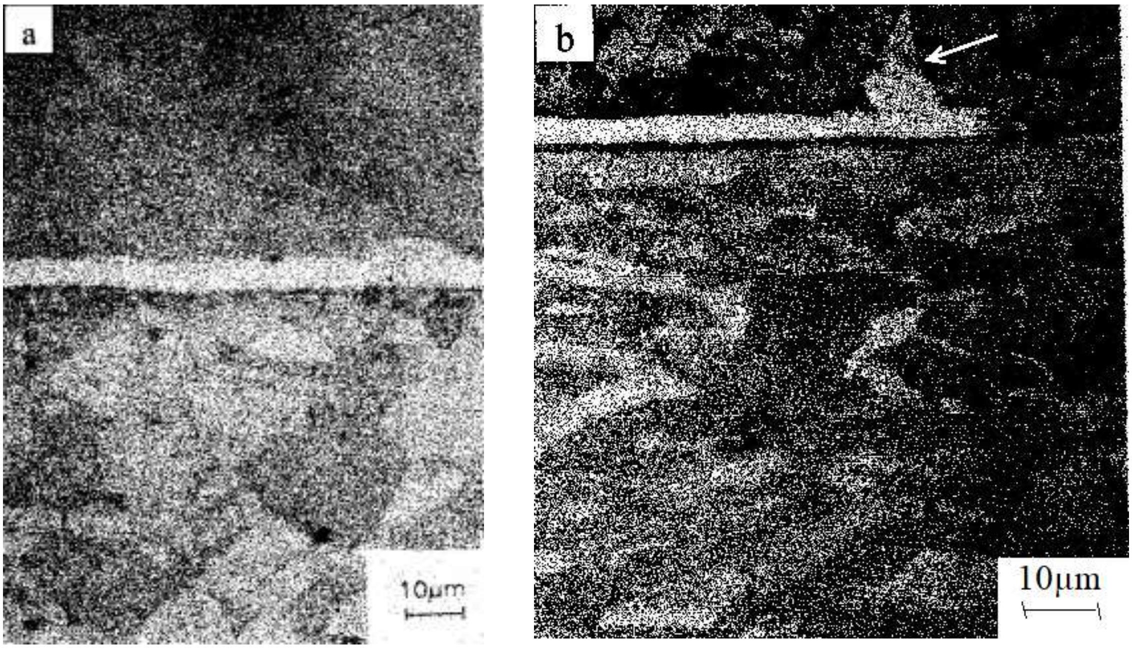

Fig. 4.9 a, b. LM micrographs of the Cu plate, Ag layer, and wires contact zones of sample 5 (a, bottom to top) and of the plate, film, and Cu wires of sample 6 (b, bottom to top). The arrow (b, top right) shows a tooth or hook-shaped Ag part between the Cu wires.

Severe metal destruction at edges of the contact interface can be caused by high tangential stresses and microslips. Under a microslip is to understand sliding between rubbing bodies when rolling, e.g. a sphere on a flat plate. Such phenomena as well as the adhesive coupling of metal pairing components in rolling friction were examined in detail in work [55].

Another test series relates to the ultrasonic joining of thin wires to one another (sample 8) or to solid, compact carrier metal parts (samples 5, 6). Also in samples 5 and 6 it is proven by the EDX analysis that there is no melting togethe or diffusion into each other between the metal components and no weld seams occur accordingly.

The boundaries both between the silver layer and the copper plate and between the silver layer and the copper wires show no diffusion zones from either side of the silver layer (figures 4.9 a, b). In the some boundary areas, silver has penetrated the pores between the copper wires of the upper part due to the plastic flow (fig. 4.9 b). This creates additional joining mechanisms through interlocking, as is the case when joining compact metal pairings. The copper wires of the upper part are compactly joined to each other (figures 4.9 a, b).

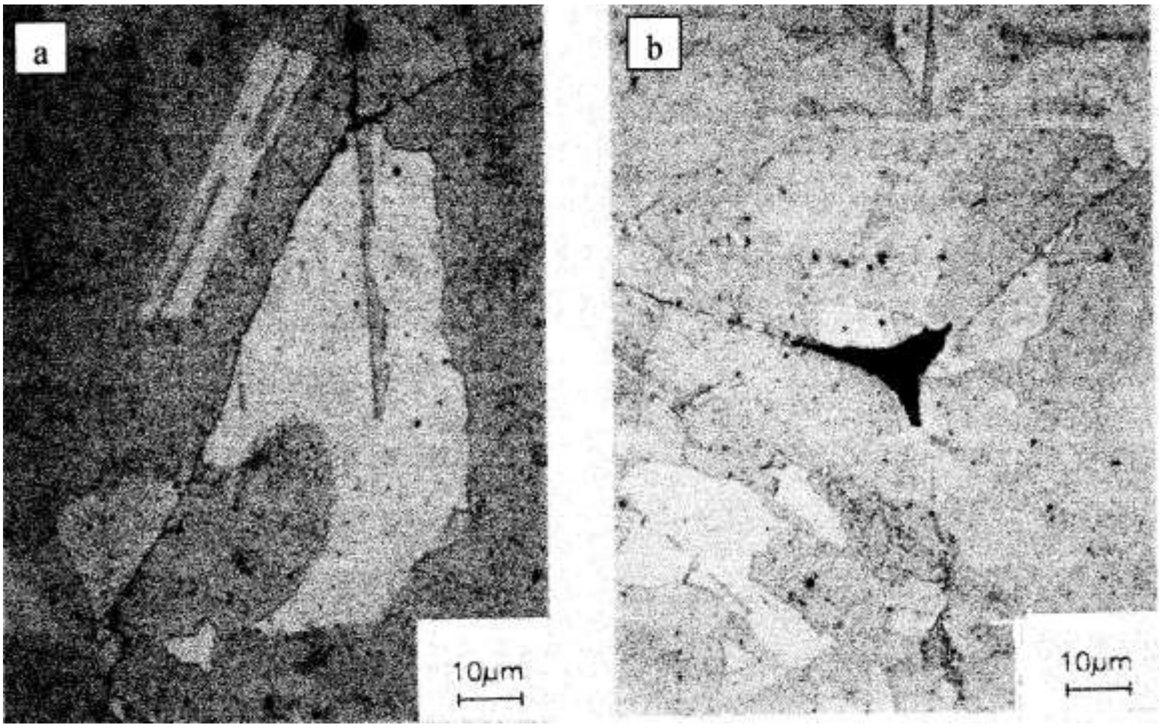

Fig. 4.10 a, b. LM-micrographs of contact segments from 4 (a) and 3 (b) wires in sample 8 bundle.

The grain structure changes due to recrystallization in the joining area cannot be determined either. Despite the strong plastic flow of the silver, there is no direct contact between the copper wires of the upper part and the copper (fig. 4.9

a) or brass plates (fig. 4.9 b) of the lower part. The lower plates do not show any deformation or destruction, although the copper wires themselves are pressed together compactly and firmly joined.

The coating of one of the metal parts to be joined with a metal of lower hardness seems to play a dampening role at the contact boundary, as can also be observed in sample 3 (fig. 4.4 a). The US vibration energy is absorbed in this layer and causes the layer metal to heat up and plastic flow, creating a tight adhesive joint between the upper and lower parts. The upper and lower parts are spared from plastic deformation and from intensive plastic flow in the boundary area.

The US metal joining mechanism of thin copper wires into a bundle is observed in sample 8 (figures 4.10 a, b). The wires, which are initially round in cross-section, are plastically deformed by nearly hydrostatic pressure from all sides into an almost symmetrical hexagonal cross-section (fig. 4.10 b), so that a maximum contact surface between adjacent wires is formed, and the same as in compact solid metal parts arises also cohesive metal joining at these contact surfaces.

The metallographic texture developed by such plastic deformation has axial symmetry, as in wire drawing. Cigar-shaped grains are oriented along the wire axis and can be seen on the cut as round grains or as grain conglomerates. Due to the irregular pressure distribution in the wire bundle during ultrasonic joining, holes or pores can remain between the wires to be joined (fig. 4.10 b). A recrystallization does not take place in this case either.

4.5 Conclusions

The experimental results presented and discussed above allow clear conclusions.

The processes that take place in metals during their joining in the ultrasonic welding procedure and lead to metal firmly joints include:

1. Cleaning the metal contact surfaces of oxide layers, if present, by rubbing them together under constant pressing force and ultrasonic vibrations.
2. A rapid but limited temperature rise in the contact zone due to the friction of the two pairing components at the contact interface and the dissipation of US vibration energy as heat.
3. Plastification of metal parts beyond the yield point up to the breaking point in the contact bondary area.
4. Shape adjustment of non-uniform metal parts through their plastic deformation until a sufficient contact surface is formed.
5. Interaction of surface electrons of the two metal parts to be joined and formation of adhesive or cohesive contact connection bridges at the roughness peaks of the contacting metal surfaces.
6. Smoothing of surface roughness by destroying the formed contact connecting bridges.
7. Formation of a solid, firmly adhesive or cohesive joints between metal contact surfaces.

Processes that have not been determined with certainty in these investigations of the ultrasonic metal joining:

1. Volume melting and mixing of the metal parts to be joined.
2. Melting of the metal parts at the contact boundary.
3. Formation of a weld seam by mixing molten metal components or by chemical reactions between metals or alloy components to be joined.
4. Diffusion of the metals or alloy components to be joined through the contact boundary into one another and formation of a diffuse transition zone.
5. Changes in grain structure due to primary or secondary recrystallization.

Based on these findings, the adhesive or cohesive metall joining of the metal parts to be joined turns out to be the main mechanism of ultrasonic metal joining.

The mechanical interlocking of plastificated metal contact surfaces occur as secondary mechanisms that are important for the adhesive strength. With such a mechanical joining of the metal parts to be joined, however, the increase in the overall adhesive or cohesive force due to the increased contact surface caused by such turbulences is said to play a more important role for the adhesive strength than a purely mechanical adhesion of individual teeth or hooks.

Acknowledgements

This research project was kindly supported by Prof. Dr. Günter Frohberg and his institute for metal physics at the TU Berlin. The author would particularly like to thank his employees Ms. E. Frommbach, Ms. H. Malks and Mr. G. Pruskil for the technical assistance they provided.

5. Plastification of metal parts in US welding process

As the results of the structural investigations of the ultrasonically joined metal pairings discussed above show, the plastic deformation of metal parts occurs to a greater or lesser extent in all cases, depending on the test conditions. The plastification and plastic flow of metals under the influence of ultrasonic thus play an important role in US metal joining as well as in US welding of thermoplastics [16]. They also open up new US metal processing opportunities such as embedding foreign substances in metal parts or embossing.

The change in shape of a metal part during ultrasonic metal joining takes place within a time interval of $(1 \div 3)s$ from the simultaneous switching on of the ultrasonic vibrations tangential to the surface of the metal part and the pressing force perpendicular to this surface. It happens as a sudden collapse of the metal part in the direction of the pressing force.

For the detailed examination of the plastification, the copper wire used in metal pairings (Table 4.1) with the same diameter $d = 3{,}2mm$ was stretched in the US welding process to plates with different thicknesses t, which were measured in the light microscope after stretching.

The stretching degree ε_n in the direction normal to the surface is calculated by the initial diameters d and final thickness t of the plate:

$$\varepsilon_n = \frac{d-t}{t} \cdot 100\%. \tag{5.1}$$

The unusual representation of the strain (5.1) corresponds to the tensile strain of the stretched specimen to its original thickness d.

Such a representation enables a magnitude-wise comparison of the elongation degree after compression with that of tension. According to this calculation (5.1), the stretching degrees were $\varepsilon_n = 0\%$ (the original sample 10a),

$\varepsilon_n = 14\%$ (sample 10b), $\varepsilon_n = 48\%$ (sample 10c), $\varepsilon_n = 110\%$ (sample 10d) and $\varepsilon_n = 195\%$ (sample 10e). The structurless surface of the $Cu-$wire samples 1, 3 and 4 (Table 4.1) stretched over $\varepsilon_n = 500\%$ during US metal joining has been shown (figures 4.2 c, 4.4 b, 4.6 b) and discussed in the previous chapter.

The structure of the undeformed sample 10a shows a uniform distribution of grains with a size of $(5 \div 20)\mu m$ (fig. 5.1 a). This distribution through the polished and etchied surface of sample cutted transversely to the wire axis corresponds to the axial texture of cigar-shaped grains formed during wire drawing. With the deformation $\varepsilon_n = 14\%$ the grain size does not change (fig. 5.1 b). The deformation twins already appear within the grains.

Strain twinning during deformation by generation and movement of partial dislocations is a well-known mechanism of copper plastic deformation at earlier stages. At the strain $\varepsilon_n = 48\%$, the strain twins disappear and the grain size still remains unchanged (fig. 5.1 c). At deformations $\varepsilon_n = 110\%$ and $\varepsilon_n = 195\%$, grain conglomerates are formed, the size of which increases with deformation from $(10 \div 20)\mu m$ ($\varepsilon_n = 110\%$, fig. 5.1 d) to $(30 \div 50)\mu m$ ($\varepsilon_n = 195\%$, fig. 5.1 e).

The coarsening grain structure is associated with rotation of adjacent grains and formation of metallographic texture, as discussed above. The crystallographic texture known for copper corresponds to the orientation of the crystallographic axis $< 112 >$ in the direction of strain.

Identical changes in grain structure are also observed in other ultrasonically joined metal pairings. For example, the grain structure of the ultrasonically joined brass and copper can be clearly seen on the polished and etched cut surface sample 3 (figures 4.4 a, b).

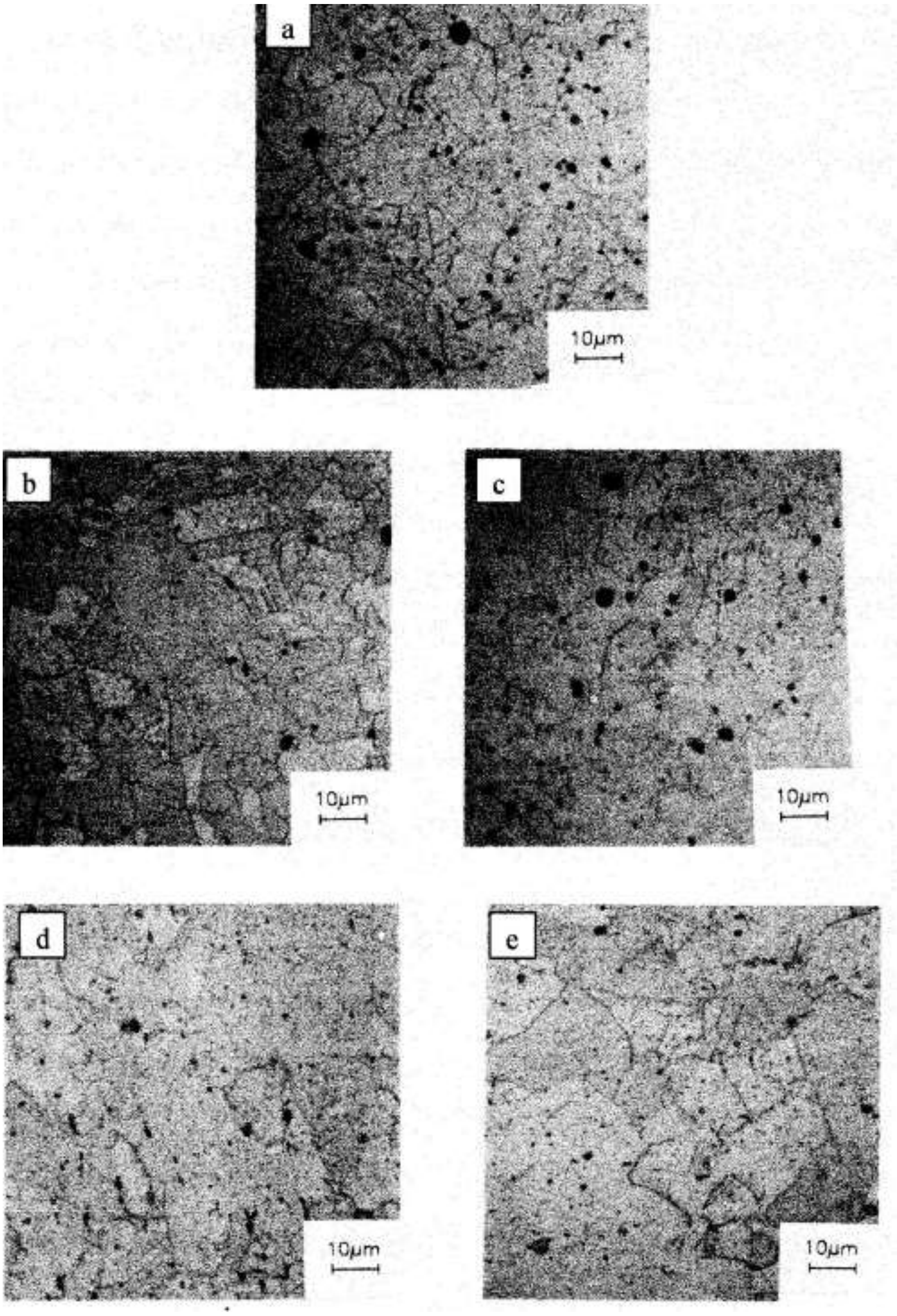

Fig. 5.1 a-e. LM-micrographs of grain structure sample 10: undeformed 0% (a) and ultrasonically stretched to 14% (b), 48% (c), 110% (d) and 195% (e).

The grain structure of brass before joining is the same as after joining and shows no changes due to US welding process (fig. 4.4 a), which also proves the dampening role of the silver layer. The grain structure in the middle of the copper wire stretched to 80% during US joining is similar to that at the contact boundary (fig. 4.4 b). This structure is also similar to the structure of the copper wire stretched in the US welding process (fig. 5.1 d).

The grain enlargement and the formation of grain conglomerates in the ultrasonically joined samples compared to the grain structure of the undeformed copper wire (fig. 5.1 a) is due to the formation of a strong metallographic texture, which arises at deformations over 50% due to the rotation of grains during plastic metal flow.

The grain boundaries between grains with the same or similar orientation have a much lower energy and are not etched out, so you no longer see individual grains, but only the large conglomerates of like-oriented grains in a sample that has been strong textured by ultrasonic deformation. In the case of a very large deformation, as in the case of the upper copper part sample 1 and sample 4, no grain structure can be seen at all, but only the traces of the turbulent plastic metal flow.

The deformation distribution in the material volume in the direction from the sonotrode to the anvil (figures 5.2 a-d) is not homogeneous. Maximum deformation is observed below the surface of the upper part on the sonotrode side. Even with a deformation of 110%, an almost structureless surface can be seen on the sonotrode side (fig. 5.2 a), because grain boundaries are hardly etched out due to the strong turbulent plastic metal flow. At the deformation of 195%, several microcracks form at the invisible grain boundaries (fig. 5.2 b).

The grain structure on the anvil side (figures 5.2 c, d) is similar to that in the middle of the sample (figures 5.1 d, e). Although there is no friction between the upper and lower parts when the $Cu-$wire is stretched and there are hardly sources of internal friction, the wire heats up rapidly during US action.

The heat production in small metal parts with thickness $t < 100 A_0^{US}$ (A_0^{US} is the initial amplitude of US vibrations) is related to the dissipation of the US vibration energy in the volume of the metal part by plastic shear deformation.

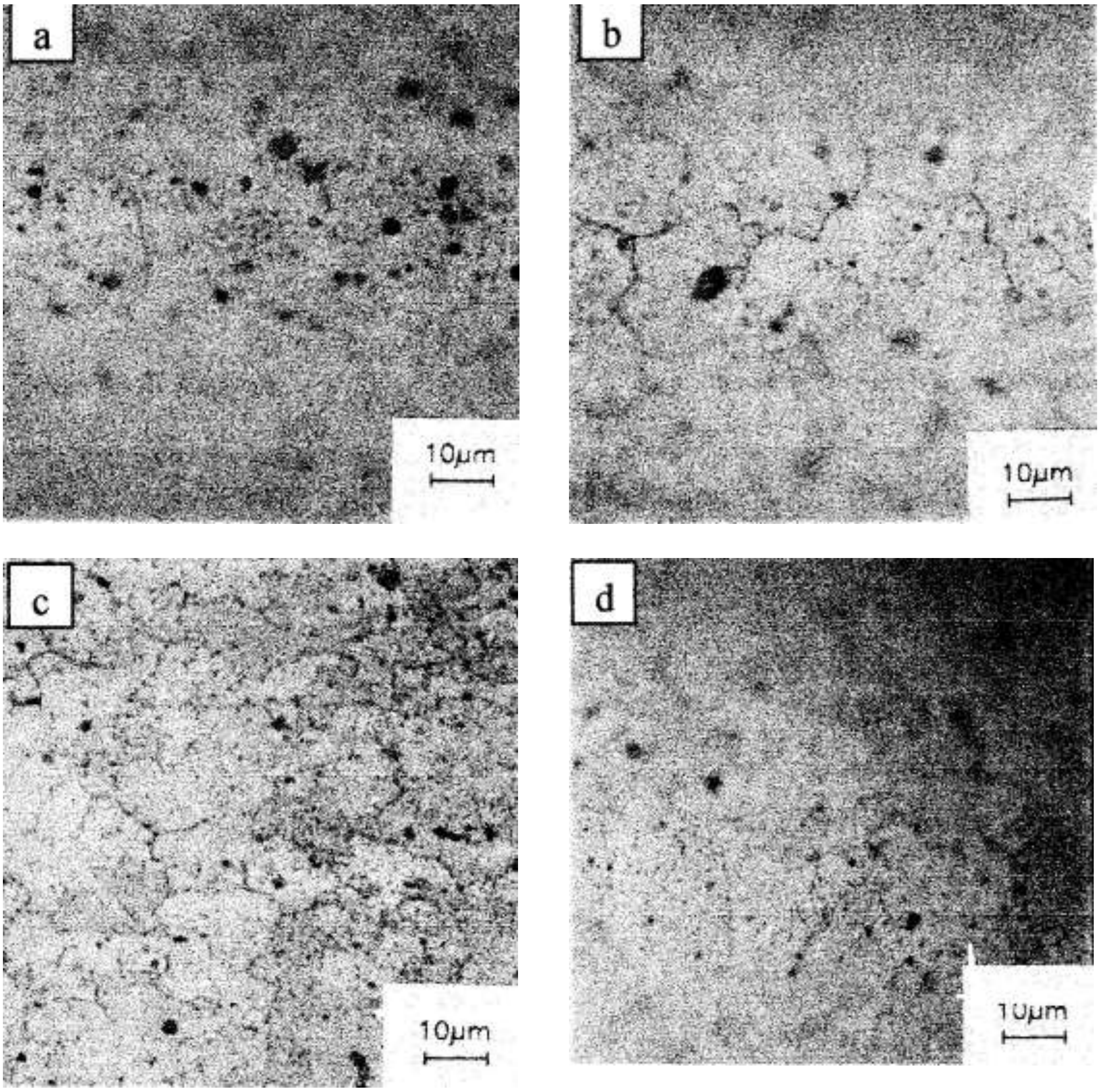

Fig. 5.2 a-d. LM-micrographs of the grain structure of the ultrasonically stretched sample 10 on the sonotrode side: 110% (a), 195% (b) and on the anvil side: 110% (c), 195% (d).

The tangential shear strain ε_τ inflicted by the vibrating sonotrode to the surface of the sample can be calculated as the ratio of the vibration amplitude to the sample thickness t:

$$\varepsilon_\tau = \frac{A_0^{US}}{t} \cdot 100\%. \qquad (5.2)$$

For the initial diameter of $3{,}2 \cdot 10^{-3} m$ of the sample 10 and the US amplitude of $30 \cdot 10^{-6} m$, the shear strain amounts accordingly to (5.2) to about $0{,}93\%$ and lays still at the elastic limit of copper. When the sample is stretched with normal deformation $\varepsilon_n \approx 195\%$, the shear strain increases to $\varepsilon_\tau \approx 3{,}1\%$. This shear strain value is well within the plastic range, with the shear direction changing with the frequency of $20 kHz$.

Due to the non-linear distribution of the deformation amplitude through the cross-section of the sample, the plastic deformation is localized in a thin surface layer on the sonotrode side. The diagram of such a plastic shear deformation represents a hysteresis loop [56] (fig. 5.3), the area of which reflects the energy dissipated mainly as heat.

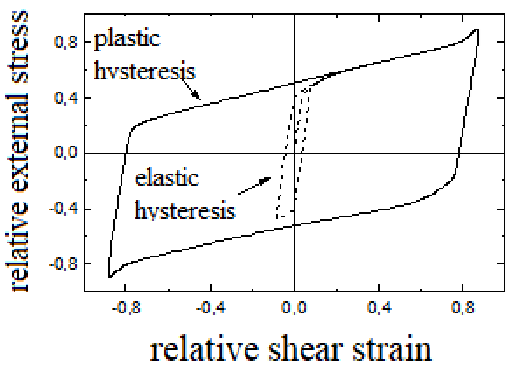

Fig. 5.3. Mechanical hysteresis of cyclic elastic or plastic tension-compression deformation.

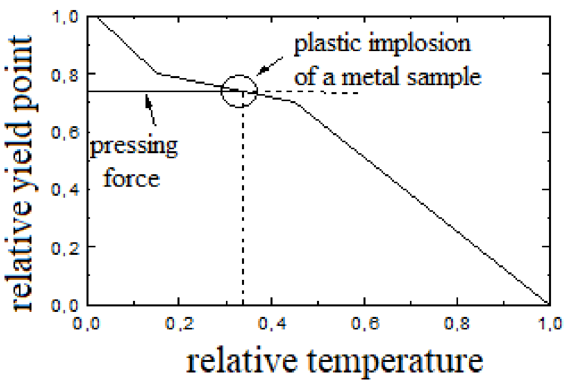

Fig.5.4. Temperature dependencies of the yield point of a metallic alloy and its plastificaton in the US welding process (general representation).

Due to the strain localization, the shear strain and, accordingly, the temperature in the thin upper layer of the sample increases drastically. It is estimated that this layer is approx. $100 \mu m$ thick (figores 5.2 a, b), which corresponds to the normal deformation $\varepsilon_n \approx 100\%$.

The non-elastic relaxation components of the micro-deformation cause US vibration energy dissipation and the hysteresis (fig. 5.3, dashed loop) also in the elastic range [56], i. e. in metal parts with thickness $t > 100A_0$. In figure 5.3, the relationships to the corresponding fracture limits are indicated as relative external stress and shear strain.

Although the amount of heat is an order of magnitude smaller than that in the plasticity area, even in this case the time-dependent relaxation components of the strain lead to a non-linear distribution of the strain amplitude through the sample depth and localization of the strain increasing in the plasticity area in the surface layer of the metal part.

Most of the heat is also produced in this surface layer and conducted into the sample volume. Depending on the thickness of the metal part and the vibration amplitude of the sonotrode, the heating time or the time up to a plastic implosion of the metal part is shorter or longer.

The increase in temperature leads to a decrease in the yield point of metal part (fig. 5.4), so that the constant pressing force at a critical temperature in this sample area exceeds the yield point. At this moment, when the US joining, e.g. from Cu wires observed an abrupt lowering of the sonotrode by the plastic implosion of the metal part, in which the material begins intensively plastically to flow. In figure 5.4, the relative temperature is the ratio of the sample current temperature to its melting temperature and the relative yield point is the ratio of the yield point of a metal sample at the current temperature to its yield point at the room temperature.

The structure of the sample in the bulk is determined by the strain under the pressing force and calculated by the change in sample thickness, while the structure on the sonotrode side is determined by the two, the high-frequency shear strain and the normal strain under the constant pressing force.

This combined exposure of a constant pressing force normal to the surface and an oscillating shear force that occurs in the ultrasonic welding process is also much more informative in studies of ultrasonic effect on the deformation behavior of metals than pure ultrasonic effect [46, 49, 50].

The friction reduction bei the ultrasonic action which leads to decreasing the yield poibt, was also observed experimentally in shape memory alloys [57]. In this case, the friction of the phase boundary moving under an external stress [4] is reduced. However, the movement of phase boundaries is nothing other than the movement of partial dislocations.

All the mechanisms of metal plastification in US welding process considered above play an important role in US metal joining process, whereby the additional heat is also produced at the contact interface by the friction of the metal parts to be joined.

The metal plastification observed in all US joining tests can in principle be used for embedding non-metallic materials such as e.g. glass or ceramic parts can be applied in a piece of metal. The ceramic piece can first be freely inserted into a hole in the metal part and then embedded into the metal that has been plastificated in the US welding process, in that the plastificated, flowing metal encompasses and encloses the exposed piece, as is also the case in the US process when embedding metal parts in plastics happens (Chapter 3).

The wavy contact boundary of the pairing and the imprints of the tool ripples on both surfaces (fig. 4.2 a) show another possible application of metal plastification in the US welding process, namely the stamping different profiles into the surface of a metal piece.

When joining the copper wire to a steel plate (sample 4, Figures 4.6 and 4.7), the wire was stretched to 300%. The $Fe-Cu$ contact boundary in this case remains planar with no wave structure from the sonotrode corrugation in both the vibration and perpendicular directions. This means that the steel plate was not plastificated during US joining because it has a higher hardness and yield point than copper. Nonetheless, a firmly permanent joint between the both metal parts has been established.

The experiment shows that the hardness, the yield point and his temperature dependence of a material to be ultrasonically stretched or ultrasonically joined play an important role in its plastification or in the adhesion strength between the joined metal parts. This data must be known and measured, if necessary, in order to set correct US process parameters such as US generator power, operating time, vibration amplitude and frequency.

The metal plastification identified and discussed here is one of the most important processes in US joining as a high frequency shear stress combined with a constant normal pressing force. Plastic deformation begins shortly after switching on the ultrasonic and during this time it passes all deformation stages from easy sliding by formation of deformation twin in copper due to dislocation splitting and movement of partial dislocations, through plastic flow by the multiplication and propagation of full dislocations as well as plastic turbulent flow by grain rotation and formation of metallographic deformation texture, to the fracture limit as it prove the microcracks in the metal part on the sonotrode side.

The deformation behavior is therefore time-dependent with constant external stress and with the lowering of the yield point on the one hand due to the temperature increase and on the other hand due to a direct effect of the ultrasonic on the dislocation generation and dislocation mobility.

For further development in this direction, investigations of the deformation behavior of various metals under an axial external stress with the simultaneous ultrasonic effect and at different temperatures are to be carried out in order to obtain the appropriate parameters.

6. US residual stress reduction in metallic workpieces

6.1 Building of internal stresses

With every kind of production and processing of metallic workpieces, internal stresses arise in these, which balance each other out within the volume of the workpiece. These internal stresses remain completely or partially after the end of the technological process and are therefore also referred to as residual stresses. The residual stresses are of an elastic nature, i. e. they are below the critical stress of plastic flow, the yield point τ_y.

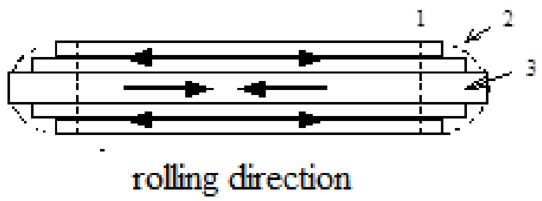

Fig. 6.1. Development of internalstresses in a metal band due to different height decreases in the central and side layers of a metal band compressed by barrel rollers (scheme): 1 - initial length, 2 - final shape and length, 3 - central layer during free compression (without interaction with its neighboring layers).

Development of internal stresses in a metal strip due to different height decreases in the central and surface layers of a metal band compressed by barrel rollers is shown schematically in figure 6.1. These macroscopic internal stresses, so-called first-order stresses, arise as a result of unequal plastic deformation or an unequal change in specific volume in different areas of the metal band.

If the metal band consisted of different free strips, each strip would have shown different sprains. Since the metal band is monolithic-uniform and all its layers are interconnected, compressive stresses will arise in the central layers and tensile stresses in the edge layers of the band due to their elastic interaction. The stresses balance each other out within the band and remain as residual stresses after the rolling.

The internal stresses also build up in many other cases and are differentiated according to process-related stress kinds. They arise with temperature changes of a heterogeneous metal body, which consists of phases with different coefficients of thermal expansion, with phase transformations between phases with different specific volumes, with heat treatment with temperature gradients, e.g. during quenching, welding, grinding, turning, milling, etc. Depending on the process, these stresses are referred to as casting, quenching, welding, etc. residual stresses

The residual stresses affect the behavior of a metallic workpiece during processing, use and even storage. They can cause a change in shape (warping), an intolerable change in size, or sometimes even the destruction of a workpiece, e.g. of an Al alloy casting. A distortion by bending or torsional deformation occurs during chip-forming such as cutting, turning, milling, etc. of a metal workpiece. This kind of processing disturbs the balance of residual stresses inside the volume. If, for example, an edge layer is cuted off the band in figure 6.1, the compressive stresses on this side will predominate and the band will be distorted by the corresponding bending deformation.

A spontaneous shape or size change can take place through the time-dependent relaxation of residual stresses. The relaxation also depends on the initial level of residual stresses, which can variy in different areas of a workpiece. Due to a different degree of relaxation in different areas of the workpiece, the initial balance is also disturbed, and a new balance of internal forces and moments of force is achieved, which inevitably leads to distortion of the workpiece.

The residual stresses are algebraically added to the operational external stresses and are able to reinforce the latter in such a way that even a small load on a workpiece can result in its breakage.

6.2 Reduction of residual stresses

The excess energy in elastic deformed areas of a workpiece can be minimized without distorting it or destroying its integrity, if a reduction in harmful residual elastic stresses occurs through local plastic deformation. So, in order to achieve full or partial reduction of residual stresses, the plastic flow must be induced by some treatment.

This condition is the basis of every known treatment method of metallic workpieces with residual stresses before their final machining. One of the classic processes is annealing: a heat treatment in which mainly the elastic residual stresses are completely, but usually only partially, relieved. This happens in two ways:

- by plastic deformation, when the elastic residual stresses τ_I exceed the plastic yield point τ_y at least in local areas (supercritical internal stresses):

$$\tau_I(T) > \tau_y(T), \qquad (6.1)$$

- by creep when these stresses are less than the yield point (subcritical internal stresses):

$$\tau_I(T) < \tau_y(T). \qquad (6.2)$$

6.2.1 Reduction mechanism of supercritical residual stresses

The elastic residual stresses τ_I are proportional to the elasticity modulus G and the magnitude of the elastic deformation ε_{el} they cause, according to Hooke's law $\tau_I = G \cdot \varepsilon_{el}$.

The difference $\frac{dG}{dT} < \frac{d\tau_y}{dT}$ between the temperature coefficients of the elasticity modulus $\frac{dG}{dT} < 0$ and the yield point $\frac{d\tau_y}{dT} < 0$ makes it possible that when a workpiece is heated, the initially subcritical residual stresses at a temperature T_y exceed the yield point $\tau_I(T_y) > \tau y(T_y)$ and become supercritical stresses (fig. 6.2). When the workpiece is heated above the intersection temperature $T \geq T_y$, the internal stresses $\tau_I(T > T_y)$, which are now supercritical, are reduced over time to this yield point due to plastic flow and creep.

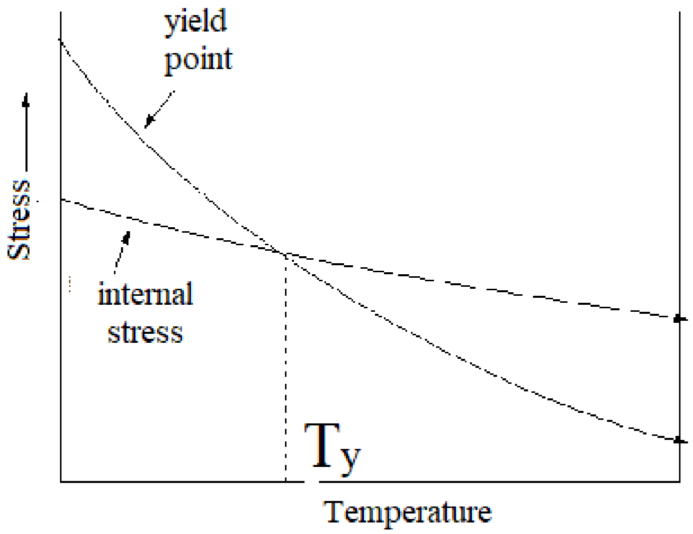

Fig. 6.2. Schematic representation of the effect of temperature on the internal elastic stresses and on the yield point.

The difference $\frac{dG}{dT} < \frac{d\tau_y}{dT}$ is based on the fact that the yield point is not only determined by the elasticity modulus and its temperature dependence, but above all by the dislocation structure, its mobility, activation energy, etc.

Dislocations are generated by the local residual stresses that are above the yield point at these temperatures, i. e. a mass generation and multiplication of dislocations takes place. Their sliding leads to rapid plastic deformation, so that stress relief is determined more by the annealing temperature than by the annealing time (holding time). The residual stresses are only partially reduced down to the yield point corresponding to the annealing temperature and reach their new equilibrium distribution or their new equilibrium state.

6.2.2 Reduction mechanism of subcritical residual stresses

Creep at temperatures $T < T_y$ (fig. 6.2) or at $\tau_I(T) < \tau_y(T)$ is the only possible mechanism for reducing elastic residual stresses in a workpiece that are smaller than the yield point. Creep allows the elastic deformation that causes residual stresses in the workpiece to transform over time into the plastic deformation ε_{pl} without affecting the overall deformation ε or shape of a workpiece:

$$\varepsilon = \varepsilon_{el} + \varepsilon_{pl} \tag{6.3}$$

At these smaller subcritical residual stresses, there is no mass generation and no mass slipping of dislocations. Slow plastic flow is caused by the sliding of a limited number of easily mobile dislocations, which is possible even at room temperature.

However, thermal fluctuations also activate the slipping of dislocations in the other slip systems that are not so favorably oriented. The thermal fluctuations also help to overcome obstacles (point defects, dislocation meshes, crystalline boundaries, etc.) where dislocations got stuck while sliding.

6.3 Relaxation of residual stresses by thermally activated processes

The time-dependent relaxation of residual stresses (fig. 6.3) in crystals or in preloaded metal samples takes place through creep. Creep is the time- and temperature-dependent viscoelastic or plastic deformation under constant load or the time- and temperature-dependent reduction of residual stresses $\sigma(t)$:

$$\sigma(t)[MPa] = \sigma_0 e^{-\omega \cdot t} \qquad (6.4)$$

where σ_0 is the initial stress and ω is a coefficient with frequency units $\left[s^{-1}\right]$.

The stress reduction with a velocity:

$$\dot{\sigma}\left[MPa \cdot s^{-1}\right] = -\omega \cdot \sigma_0 e^{-\omega \cdot t} = -\omega \cdot \sigma(t) \qquad (6.5)$$

take place through movement of dislocations, diffusion of vacancies and other defects in the internal stress field. These processes only set in after thermally activated overcoming of energetic barriers such as Peierls-Nabarro barriers [59].

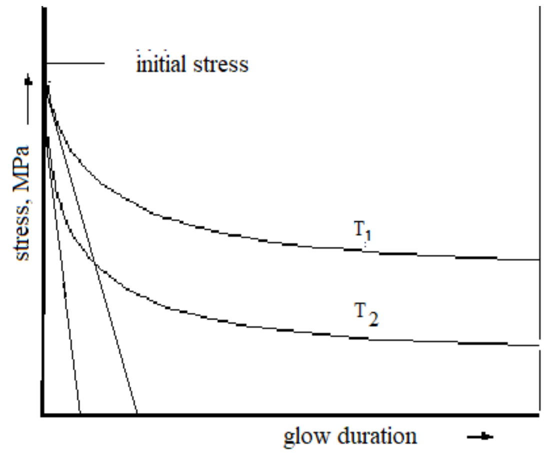

Fig. 6.3. Reduction of residual stresses with increasing holding time at two different annealing temperatures $(T_2 > T_1)$.

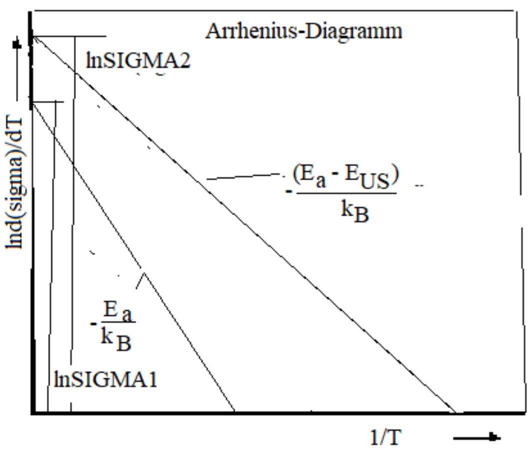

Fig. 6.4. Arrhenius diagram $\ln\dot{\sigma}$ vs. T^{-1} for determination of activation energy.

The kinetics of thermally activated relaxation is subjected to the Arrhenius law: the rate $v\left[s^{-1}\right]$ of a chemical thermally activated process has an exponential character:

$$v = \frac{dn}{dt} = K \cdot e^{-\frac{Q}{R \cdot T}}, \tag{6.6}$$

where n is the number of individual reaction steps (e.g . change of position of atoms), $K\left[s^{-1}\right]$ is the pre-exponential factor or Arrhenius pre-factor, $R\left[J \cdot K^{-1}\right]$ is the universal gas constant, $E_a[J]$ is activation energy or energy of the barrier to be overcome, $T[K]$ is absolute temperature.

Thermal activation means the supply of energy to the substance by increasing the temperature until this activation energy exceeds the energy barrier responsible for the start of a process. Any heat treatment to reduce internal stresses in metal alloys, such as annealing or tempering, is based on this.

The tempering temperature T_a in the tempering process for reduction of residual stresses in metals is related to the melting temperature T_m approximately as $T_a \approx 0.4 T_m$ [4]. Below the tempering temperature, residual stresses can only be reduced by thermal fluctuations. At temperatures above the tempering temperature, intensive movement of dislocations begins, i. e. plastic deformation leading to stress reduction. The activation energy serves to overcome Peierls-Nabarro barriers for dislocations.

The reduction rate of residual stresses can also be represented in Arrhenius form (6.6):

$$\dot{\sigma} = \Sigma \cdot \exp\left(-\frac{E_a}{k_B \cdot T}\right), \tag{6.7}$$

where $\Sigma\left[\frac{J}{kg \cdot s}\right]$ is the pre-exponential factor, k_B is Boltzmann constant and $E_a[J]$ is the activation energy required to overcome lattice friction and allow dislocations to slide.

The activation energy E_a and the pre-exponential factor Σ are obtained from the plot $\ln\dot{\sigma}$ vs. $\frac{1}{T}$ (Arrhenius diagram, fig. 6.4) by taking the logarithm of equation (6.7):

$$\ln\dot{\sigma} = -\frac{E_a}{k_B}\cdot\frac{1}{T} - \ln\Sigma \tag{6.8}$$

The slope of the Arrhenius line determines the exponent $-\frac{E_a}{k_B T}$ and the ordinate (Fig. 6.4) results $\ln\Sigma$. The $\dot{\sigma}$ values are calculated graphically as the tangents (derivatives $\frac{d\sigma(t)}{dt}$) from the relaxation curves (Fig. 6.3) determined experimentally at different annealing temperatures $T_i > T_a$.

So, the higher the initial stress and the annealing temperature, the greater the rate of stress relaxation. After rapid dissipation, the internal stresses reach a saturation level that hardly depends on the annealing time (fig. 6.3). However, an increase in temperature for the complete reduction of residual stresses is limited by the occurrence of possible undesirable structural and phase changes.

In order to complete the reduction of residual stresses, temporal overloading of a workpiece, e.g. knocking off a cast ingot. The overload stresses are added to the residual stresses and lead to their plastic relaxation. These methods also include treatment through heat cycles or temperature shocks or through vibrations (vibrating table).

6.4 Reduction of residual stresses by ultrasonic treatment

All of the mechanisms for reducing residual stresses through plastic deformation considered above can certainly be implemented during the US treatment of a workpiece.

6.4.1 Physical requirements

Ultrasonic effect on reducing residual stresses as thermally activated generation and propagation of dislocations consists in reducing friction and lowering energetic barriers by the magnitude of US vibration energy E_{US} introduced into a metall workpiece. In view of this, the ultrasonic effect can be naturally incorporated into the kinetic Arrhenius equation (6.7) and thereby analyzed:

$$\dot{\sigma}_{US} = \Sigma_{US} \cdot \exp\left(-\frac{(E_a - E_{US})}{k_B \cdot T} \right). \tag{6.9}$$

Equation (6.9) describes the direct US effect as a reduction in the activation energy and the resulting increase in the reduction rate of internal stresses $\dot{\sigma}_{US}$. The other ultrasonic-specific effects considered below also increase this rate by increasing the pre-exponential factor Σ_{US} (fig. 6.4).

The direct influence of the US energy on the energetic barriers assumed in (6.9) can easily be tested experimentally by comparing the slopes of the Arrhenius straights determined in the experiments described above with and without ultrasonic (fig. 6.4). Unfortunately, there are still only a few experimental results [46, 50, 59, 62], but many models and simulations in this direction [48, 63-69].

The decreasing the activation energy and increasing the dislocation velocity have been experimentally proven in semiconductors [62]. Cleaning the grain volume from dislocations by their movement to the grain boundaries and reducing internal stresses by 20% depending on the amplitude of US vibrations by restructuring dislocation distribution, i.e. plastic deformation, have been evaluated in numerical simulations [63-65]. Increased creep deformation and a general increase in dislocation density or plastic deformation are discussed in theoretical models [66-68], whose theoretical results agree well with experimental ones.

The extended constitutive model [69] also gives the decreasing the yield point $\tau_y^{US} < \tau_y$ during deformation under the US action, referred to as US softening, in good agreement with experimental results. This effect can be used in manufacturing processes based on the plastic deformation of metal workpieces, such as rolling, wire drawing, deep drawing, etc., in order to avoid or reduce the metal from sticking to the tools.

The addition of US vibration energy thus reduces the exponent in (6.4) and thus has a similar effect to an increase in temperature (fig. 6.3), with the upper line as stress reduction at a constant temperature T_1 without ultrasonic and the lower line as stress reduction at the same temperature T_1 with ultrasonic can become. The effect is the greater, the greater the amplitude and frequency of the US vibrations, because the US vibration energy E_{US} depends parabolically on the amplitude and linearly on the frequency (3.6).

The assumption shown analytically in (6.9) about the direct ultrasonic effect on the energetic barriers applies equally to all thermally activated processes taking place in solids, which contribute directly or indirectly to the stress reduction by influencing the mobility of dislocations such as diffusion of defects.

The diffusion coefficient $D(T)$ represented in Fick's laws $J = D\dfrac{\partial c}{\partial x}$ and

$\frac{\partial c}{\partial t} = D\frac{\partial^2 c}{\partial x^2}$ also shows an exponential form of temperature dependence similar to the Arrhenius equation (6.7):

$$D(T) = D_0 \cdot e^{-\frac{E_B}{k_B \cdot T}}, \qquad (6.10)$$

where D_0 is the initial diffusion coefficient (e. g. at room temperature) and E_B is energy barrier for the individual diffusion jumps.

Similar to eq. (6.7), one can postulate the effect of the US vibration energy E_{US} on the diffusion coefficients in solids as a direct decreasing the energetic barriers for the individual diffusion acts:

$$D(T) = D_0 \cdot e^{-\frac{E_B - E_{US}}{k_B \cdot T}}. \qquad (6.11)$$

The diffusion of defects (vacancies, interstitials, etc.) in the internal stress field itself can lead to the reduction of these stresses. But even more important is the US effect on the mobility of dislocations, which leads to overcoming obstacles, climbing and cross-slipping of dislocations and thus promoting internal stress-relieving creep deformation.

6.4.2 Heat and stress effects by US vibration

The relaxation of internal peak stresses in a workpiece by plastic flow, even at room temperature, can be achieved simply by adding these local peak stresses τ_S to the elastic stresses τ_{US} of ultrasonic vibrations, which induce elastic deformations in this workpiece with an amplitude $\Delta\varepsilon_{US}$ and contribute to the fulfillment of the follow condition:

$$\tau_S + \tau_{US} = G \cdot (\varepsilon_{el} + \Delta\varepsilon_{US}) \geq \tau_y \qquad (6.12)$$

where τ_y is the yield point, the critical shear stress limit of plastic flow.

The further reduction of internal stresses occurs through the plastic deformation with lowering the yield point (fig. 6.2) due to the temperature increase, so that the condition (6.1) or (6.12) for smaller internal stresses is fulfilled [24].

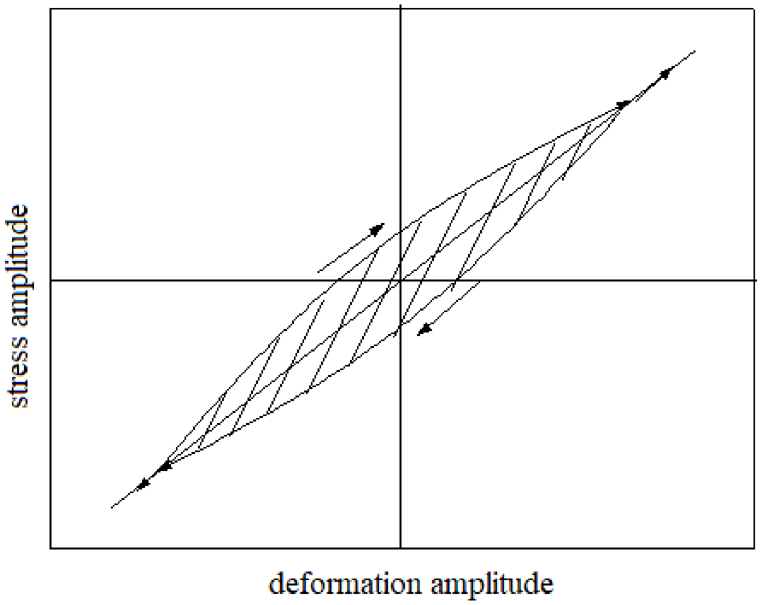

Fig. 6.5. Energy dissipation during ultrasonic vibrations of a metal body in the elastic range (see also fig. 5.3).

The experimentally measured [41, 58], even though relatively small, increase in temperature by the ultrasonic effects on metals is caused by heat production. Even in the elastic range of a metal body, US vibrations are accompanied by time-dependent relaxation processes that lead to energy dissipation (fig. 6.5):

$$e_{dis}^{US}\left[{}^{J}\!/_{kg}\right] = \frac{1}{\rho}\Delta\tau_{US}\cdot\frac{A_0^{US}}{d}\cdot f_{res}^{US}\cdot t\,, \qquad (6.13)$$

where e_{dis}^{US} is US dissipated energy per mass unit, $\Delta\tau_{US}$ is amplitude of US shear stresses, $\Delta\varepsilon_{US} = \frac{A_0^{US}}{d}$ is amplitude of US shear strain, d is thickness of workpiece normal to the US vibration axis, t is duration of US action.

The dashed area of the (visco)elastic hysteresis loop drawn in figure 6.5 corresponds to the energy dissipated as heat during one oscillation period [4, 24, 56]. At an ultrasonic resonance frequency f_{res}^{US} in the kHz range, even such a small heat production leads to a rapid temperature rise $\Delta T[K]=\frac{e_{dis}^{US}}{c_p}$ of a workpiece with a heat capacity c_p.

Since the rapid plastic deformation hardly depends on time, but above all on temperature and elastic stresses, as shown above, this short exposure time is sufficient for the effective reduction of elastic residual stresses.

6.4.3 Ultrasonic-specific plastiification effects

Much more important for the complete reduction of subcritical elastic residual stresses is the less well-known effect of ultrasonic, namely creep acceleration. Apart from the thermal activation caused by the temperature increase, this acceleration of the plastic deformation through creep has the following purely ultrasonic-related reasons:

- friction reduction [16, 55] of the sliding dislocations by the elastic US vibration energy, which appears as an additional term in the exponent of equation (6.7), reducing the Peierls-Nabarro barriers
- bulk multiplication and generation of dislocations [45, 46, 59, 60] by activating Frank-Read and other dislocation sources under the tangential ultrasonic stresses
- mass sliding of dislocations by including the dislocations blocked by obstacles and lying in unfavorably oriented slip systems and mobilized by the overall US action
- ultrasonic-initiated polygonization and grain structure shrinkage through the formation of dislocation walls of various types (similar to recrystallization in heat treatments)
- diffusion accelerated by ultrasonic in gradients of the internal stresses, which leads to the reduction of these gradients and thus to a reduction in internal stress

So, the physical principles and the experimental results already available speak in favor of the ultrasonic treatment of metall workpieces as the treatment method for the close to complete reduction of elastic residual stresses.

6.5. US technique for the US treatment of metallic workpieces

In order to exhaust all the reduction mechanisms considered above for relieving residual stresses, it is desirable to simultaneously subject the workpiece to the tangential US vibrations that generate the shear stresses in the workpiece, as in US metal joining, and to the normal US vibrations, as in US welding of thermoplastics.

The application of the US treatment of metallic workpieces naturally requires specific ultrasonic technology such as ultrasonic generators, vibrating systems, etc. that correspond to the objective. This technology was developed for years by the company ”Ultrasonics Steckmann GmbH” (see appendix) for US welding and US processing of plastics [15] as well as for US metal joining and US treatment [16, 20].

Powerful generators:

In order to create the ultrasonic effects described above for the reduction of elastic internal stresses, sufficient US-energy must be added to a metallic workpiece in particular. The powerful generators developed by “Ultrasonics Steckmann GmbH” are presented in photos in the appendix. The power consumed from the electric power grid is up to $3kW$ at resonance frequencies of $(20 \div 70)kHz$.

Ultrasonic resonance systems:

An US vibration or resonance system generally consists of an ultrasonic transducer, a transformation piece (booster) to adjust the vibration amplitude and a sonotrode to transfer the US-energy to the workpiece to be treated. The resonance systems were developed by “Ultrasonics Steckmann GmbH” for various purposes (see appendix).

Since the treatment of large workpieces such as cast ingots requires large amounts of US-energy, the sonotrode should afford a high resonance frequency,

e. g. of $70kHz$ and a large amplitude e.g. of $100\mu m$. These mechanical vibrations are applied to the metallic workpiece to be treated.

Procedure:

In addition to the US technique shown in the attached photos, the US-process for the treatment of metallic workpieces generally includes a few more technological steps.

These include:

- setting the amplitude
- adjustment of the pressing force to the amplitude and the generator output power
- setting the ultrasonic switch-on time
- setting the impact velocity of the sonotrode
- setting the treatment time.

The whole process has to be developed for the specific metallic workpieces and process-specific kinds of stress.

Künftige Aufgaben und Perspektiven:

All of the aspects considered above indicate that ultrasonic treatment of metal workpieces not only reduces residual elastic stresses, but also improves mechanical properties, e. g. is to be expected by a refinement of the grain structure. The US-reatment is also less expensive and much faster than conventional methods, and can easily be automated and integrated into other production processes.

The plastic deformation necessary for the reduction of residual stresses and accordingly the degree of stress reduction in the metallic workpieces treated with ultrasonic depends both on the adjustable US-parameters and on the shape and material properties of the workpiece to be treated, such as hardness, yield point and their temperature dependence, etc.

The data must be known, if necessary determined experimentally, in order to set the correct US-parameters such as the power supplied by the generator, the effective time, and the vibration amplitude. Above all, the resonance frequencies of a workpiece must be calculated or determined in advance and avoided, because the resonance can lead to rapid cracking and even destruction of the workpiece to be treated [49].

So, there is still a great need for research and development for the application of US-treatment of metallic workpieces to reduce elastic residual stresses.

7. Appendix. Ultrasonic devices and systems

In this appendix, US devices and US systems are presented, which were developed and used by the company “Ultrasonics Steckmann GmbH” in many years on behalf of various global industrial companies:

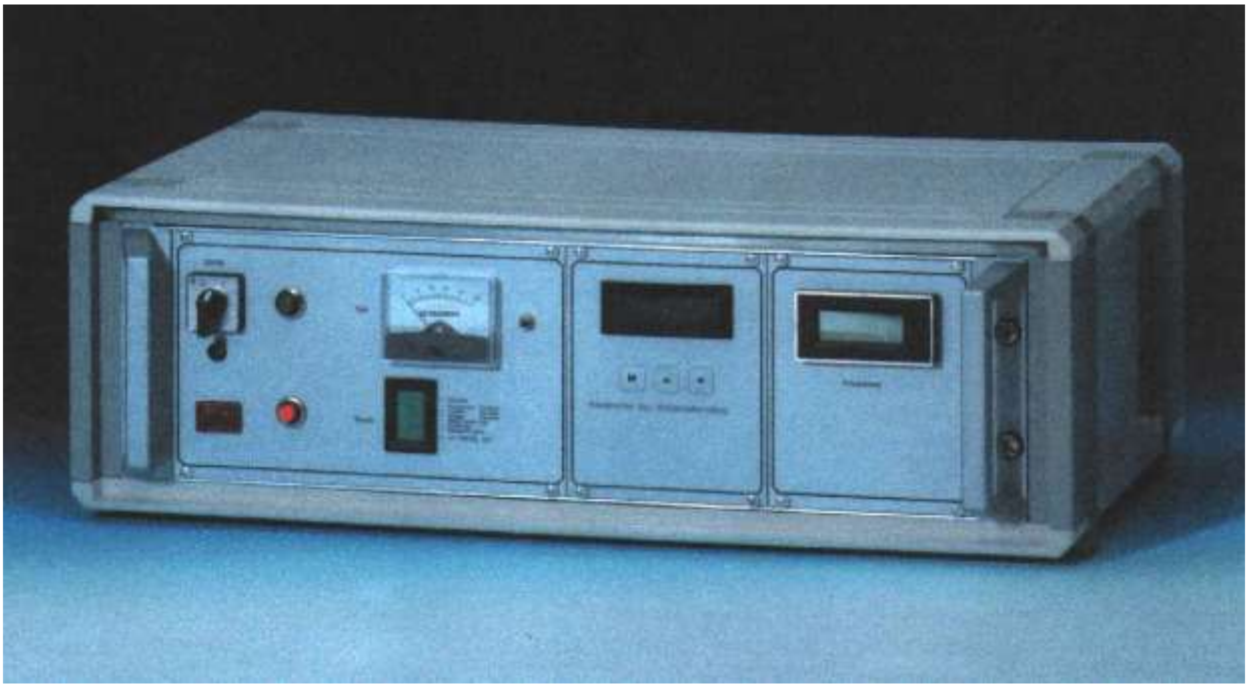

US generator with a power of $3kW$

US resonance systems

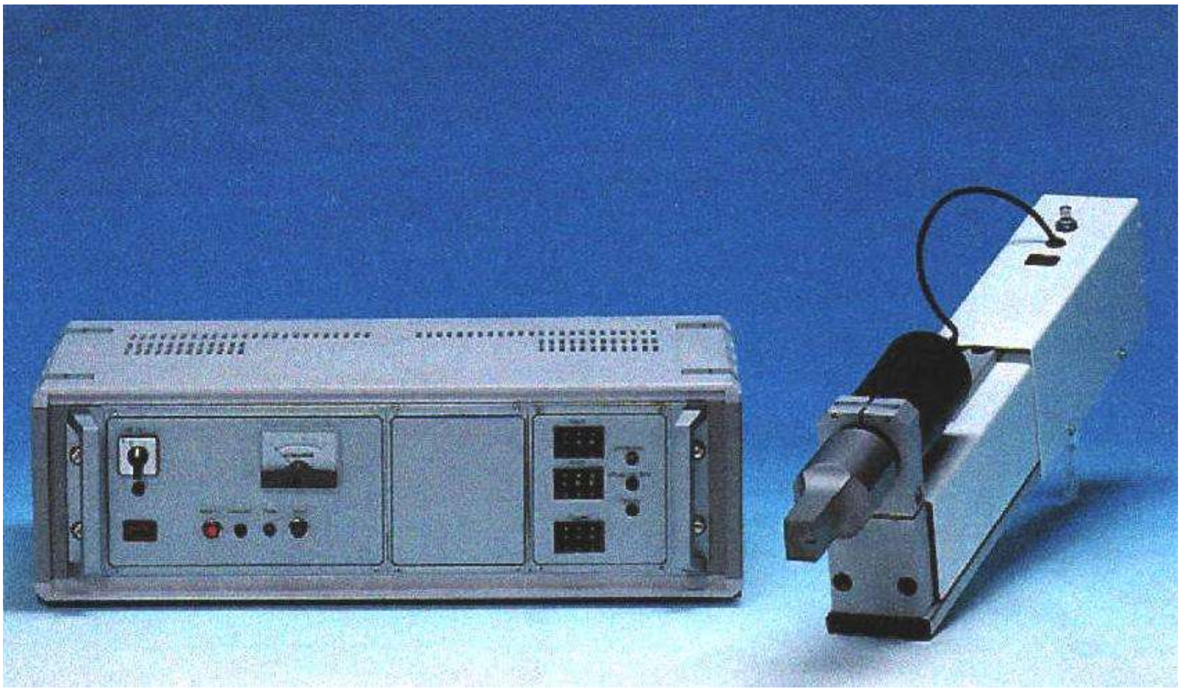

US method for metal joining

The precise and the inexpensive US welding systems

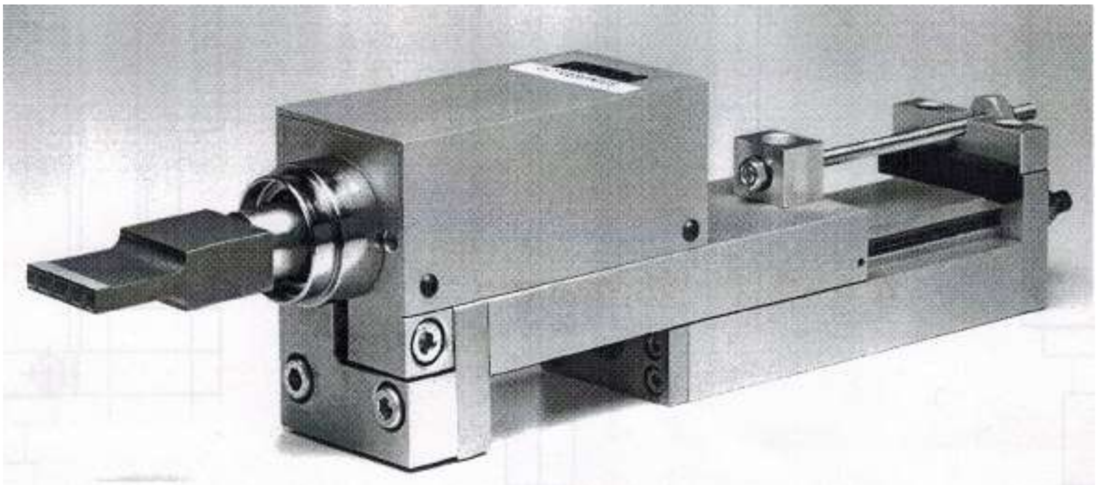

35*kHz* standard linear feed system with US vibrating head, consisting of converter, booster and sonotrode

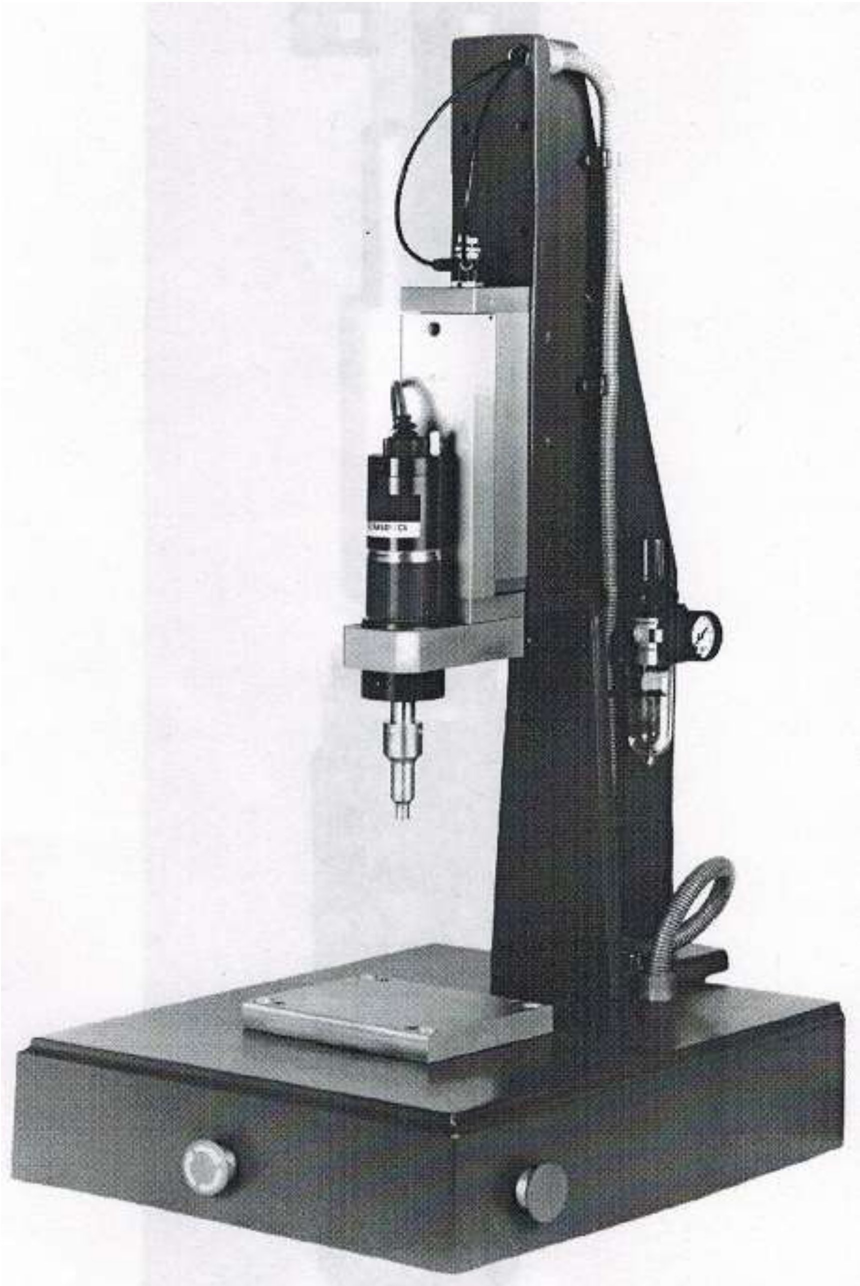

A $35kHz$ transducer system in a "mother-daughter arrangement

The base, to which an adjustable mounting plate is screwed, and the stand, to which the feed system is slidably attached, are made of solid cast aluminium

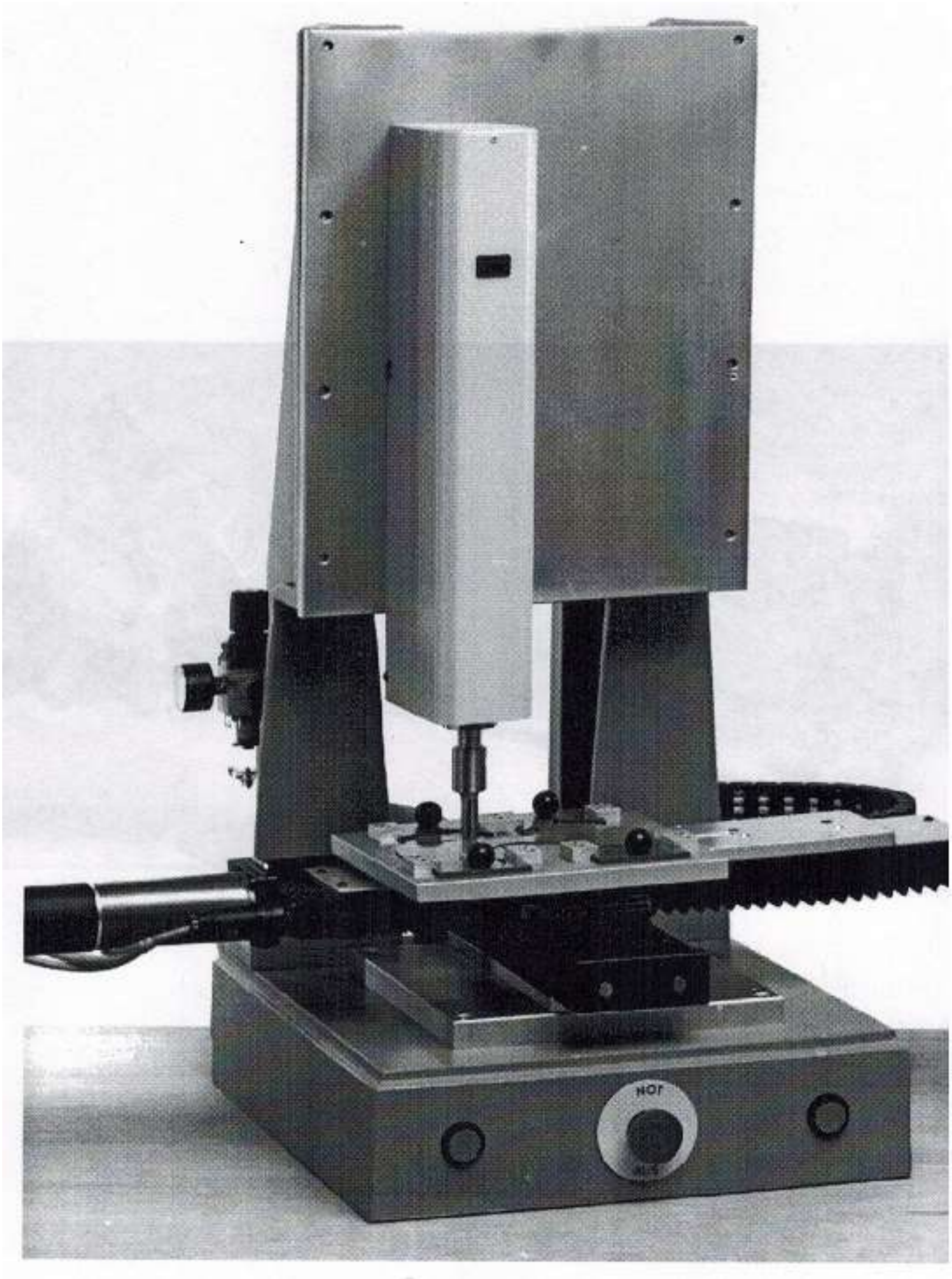

$35kHz$ welding system with path control for welding intricate contours

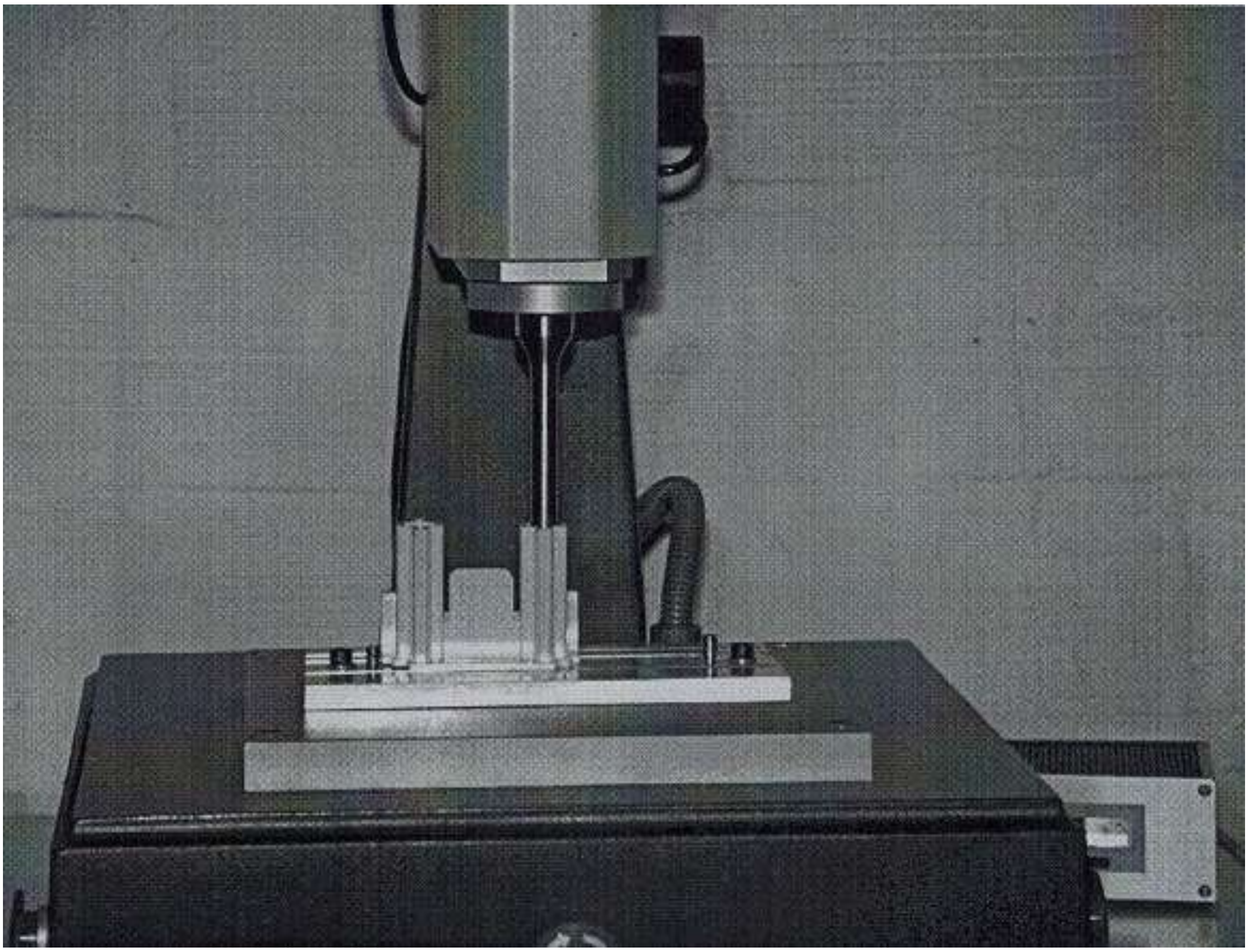

US system for embedding brass nuts in plastic parts

US generator with a $X - Y$ path control for following any curves and radii

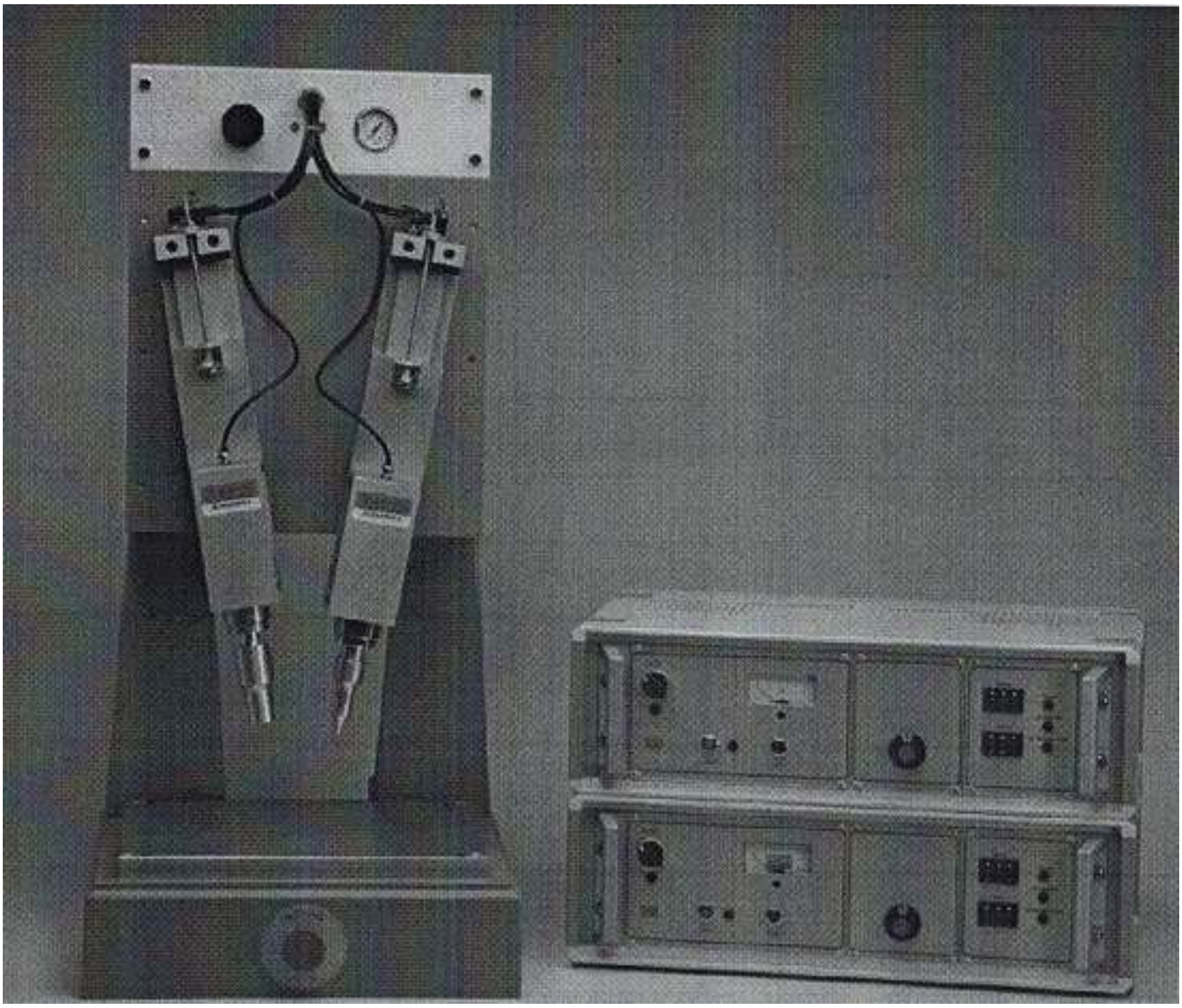

Cylinder welding machine for simultaneous welding at two positions
for a household appliance

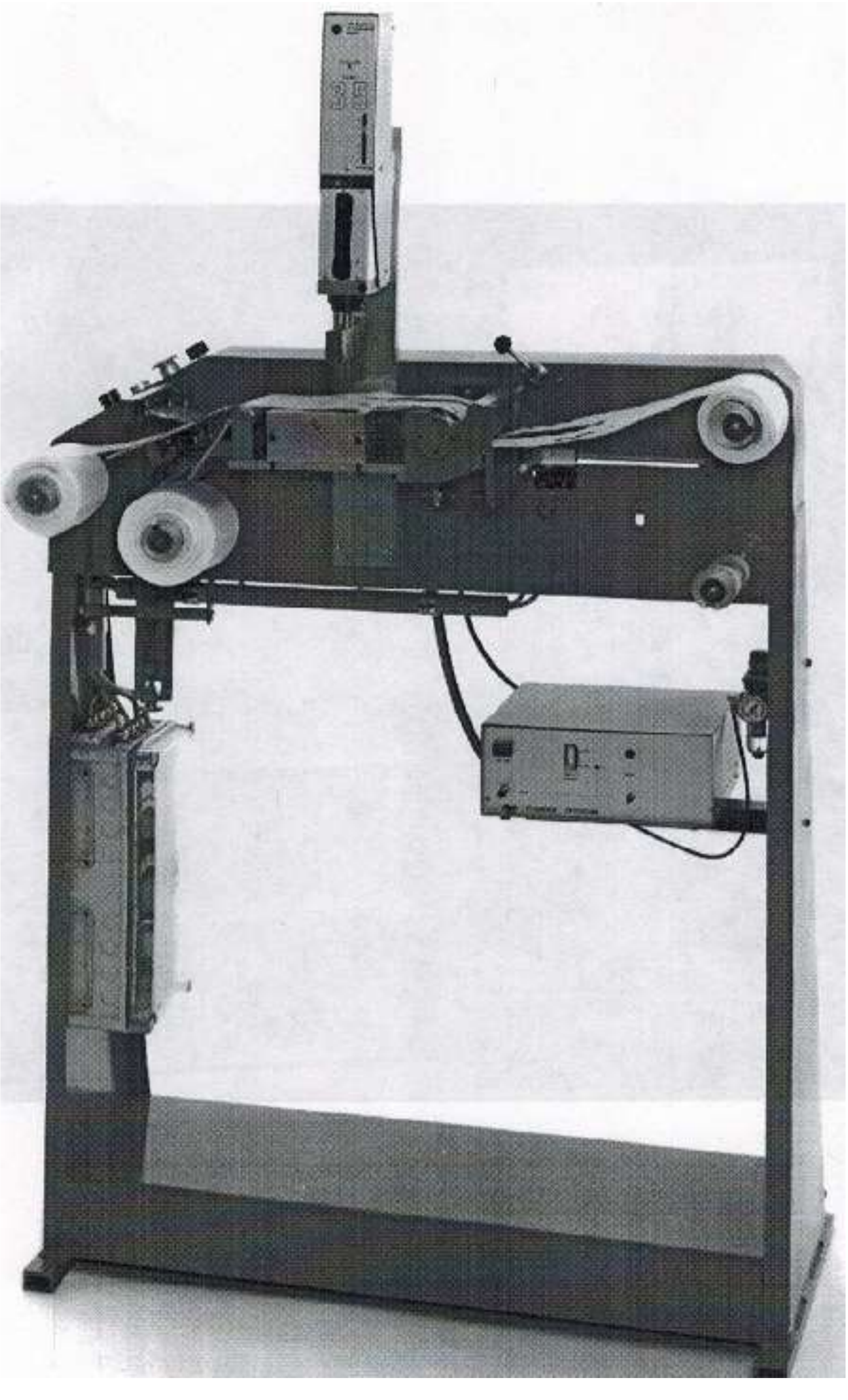

Machine for US welding of synthetic textile fabric to small diameter hoses or tapes with plasticized edge protection

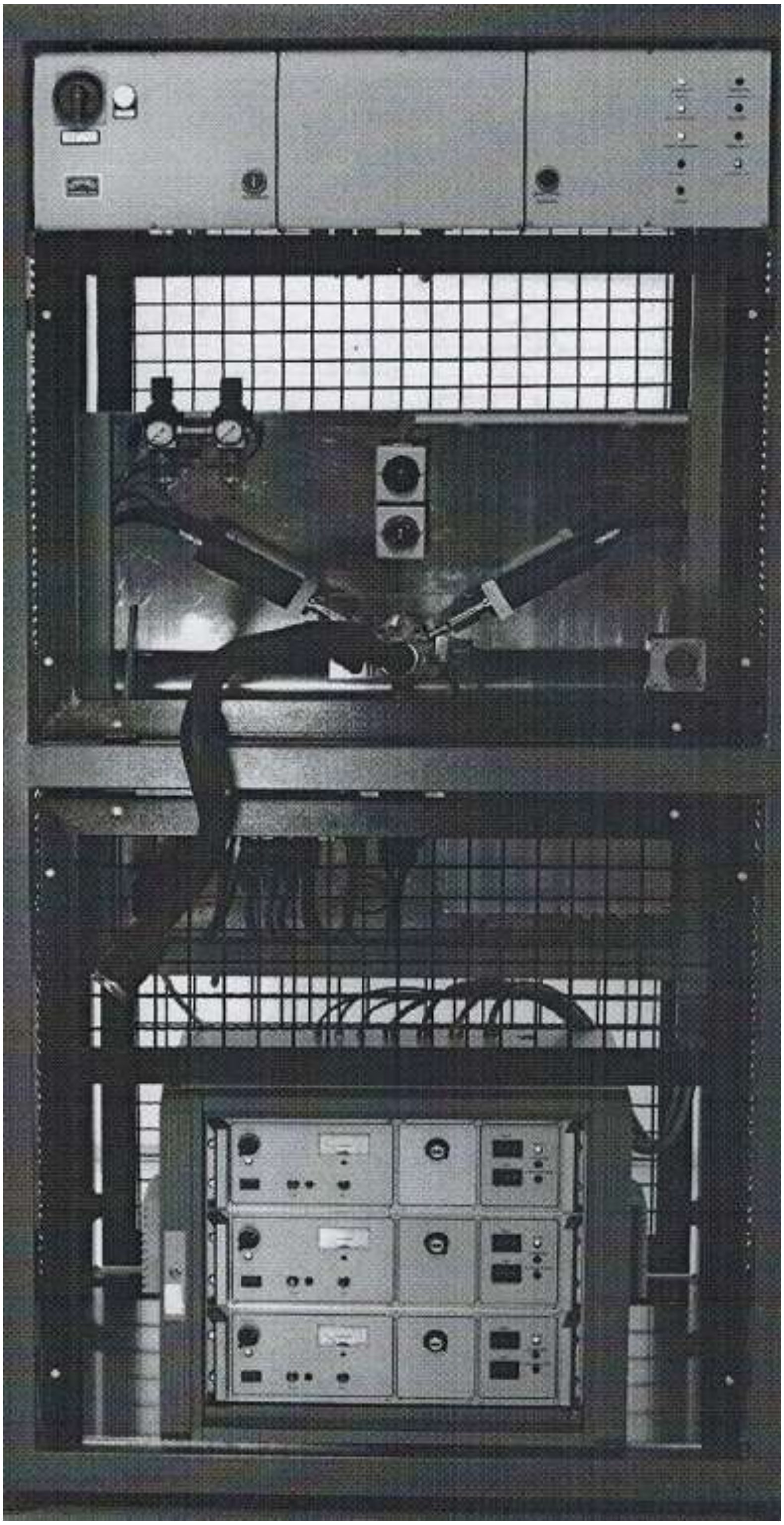

Fully automatic US welding system for welding valves to vehicle filler pipes

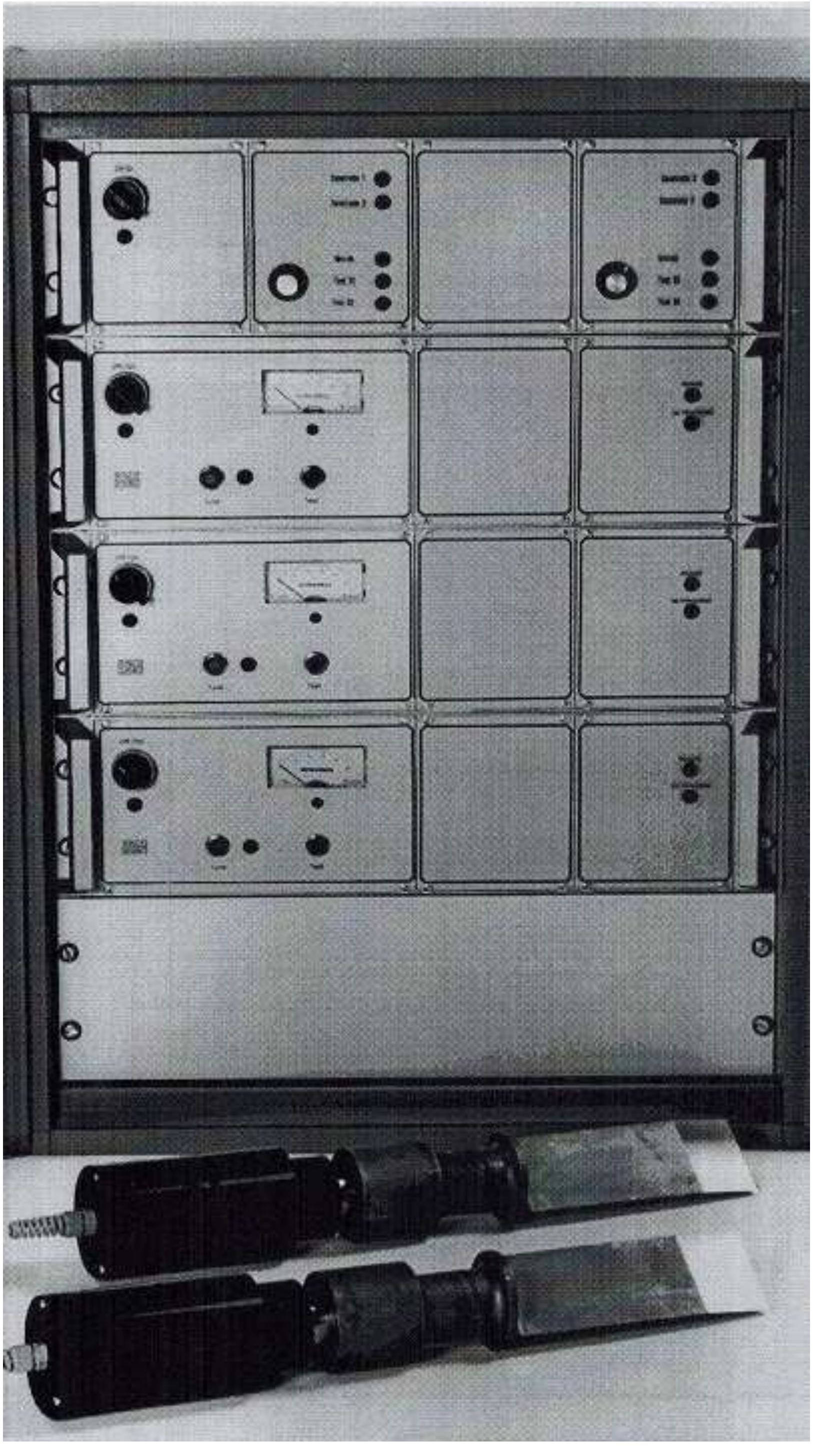

US installation for the fully automatic removal of lost heads in a production plant

35*kHz* standard linear feed system with US vibration head,
consisting of converter, booster and sonotrode

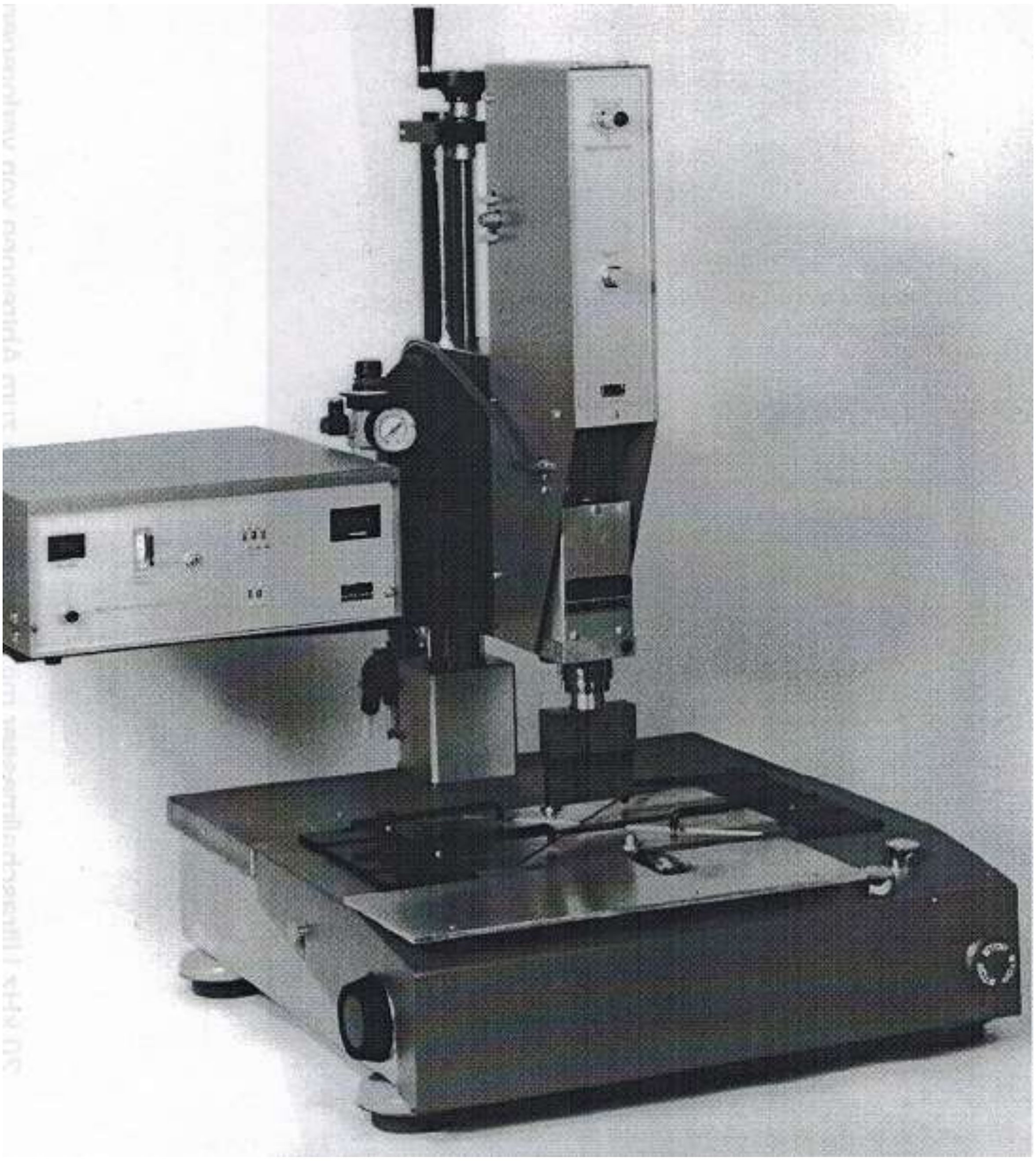

35*kHz* US welding machine for ribbons

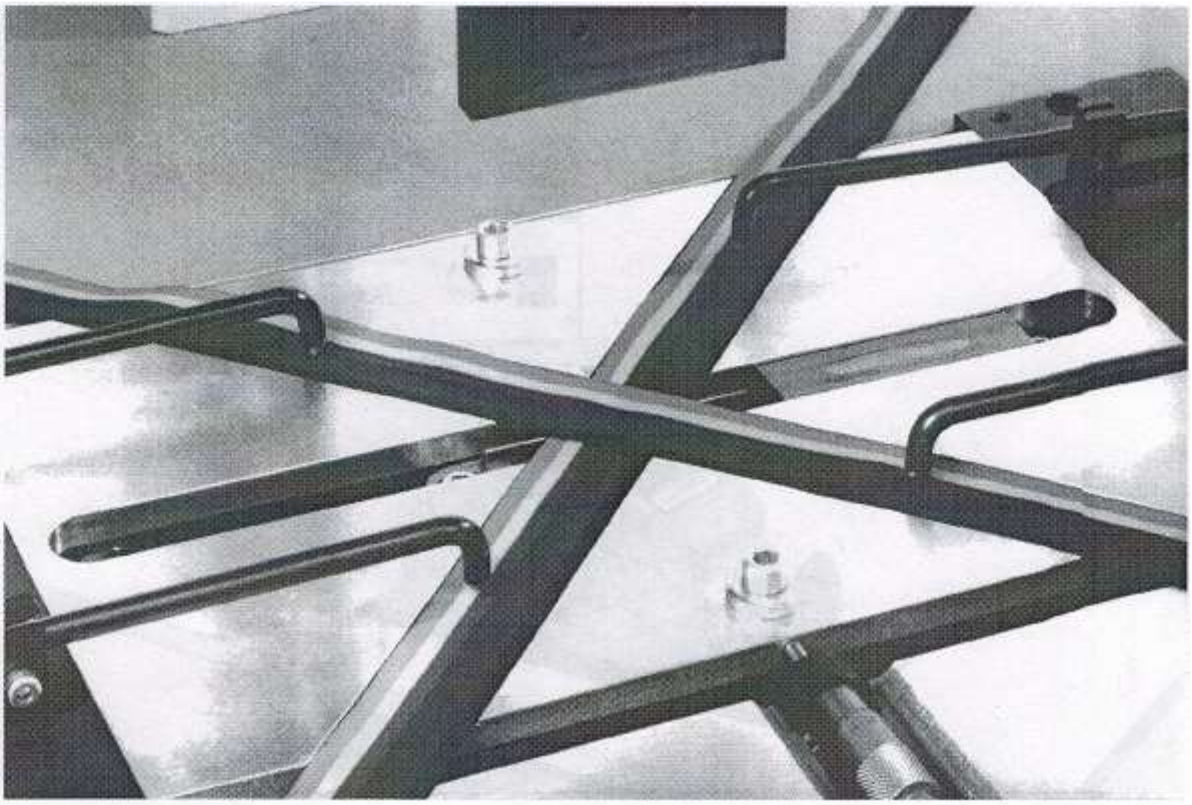

Working table for US welding of ribbons
with precise adjustment of the welding zone using a micrometer screw

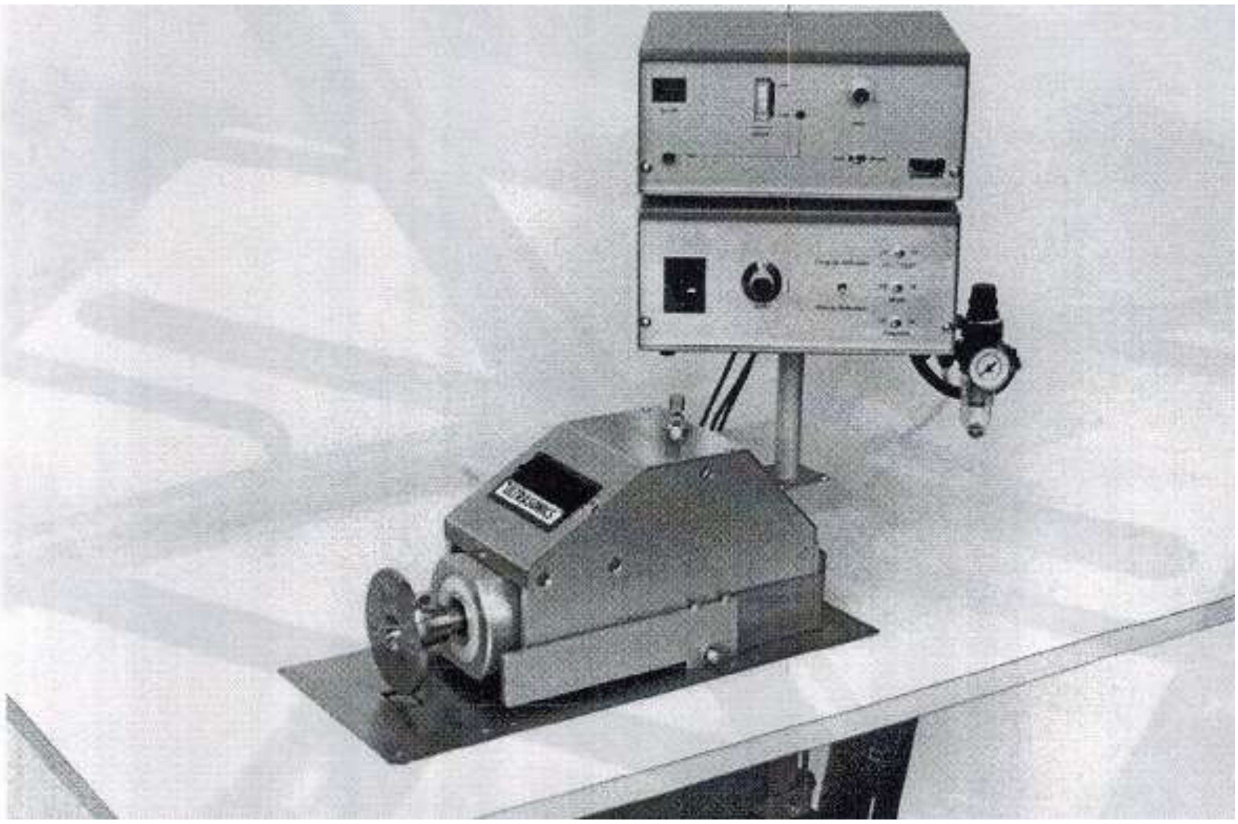

$35kHz$ US roll seam welder for welding synthetic fabric and films

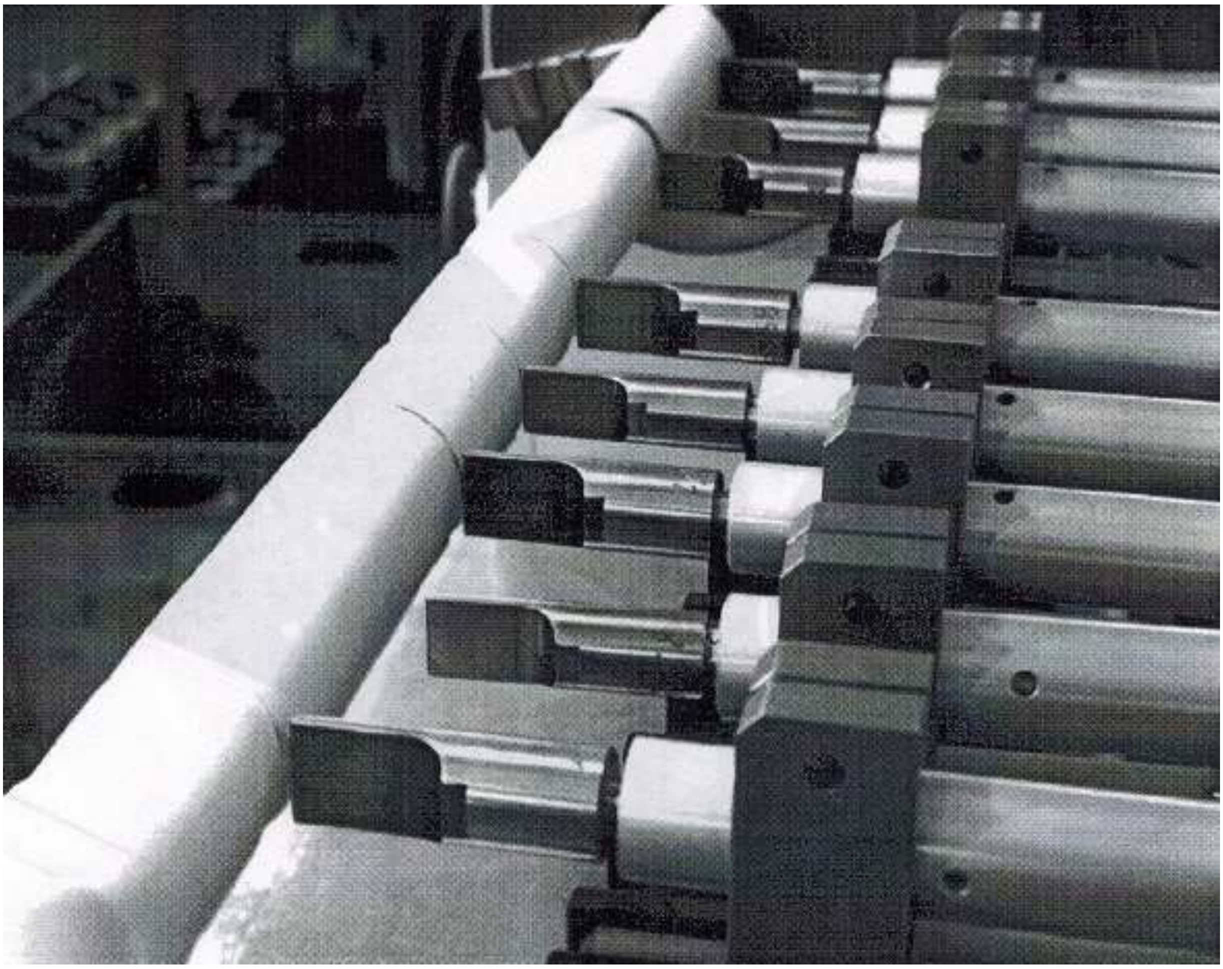

US plant for cutting polyester hoses

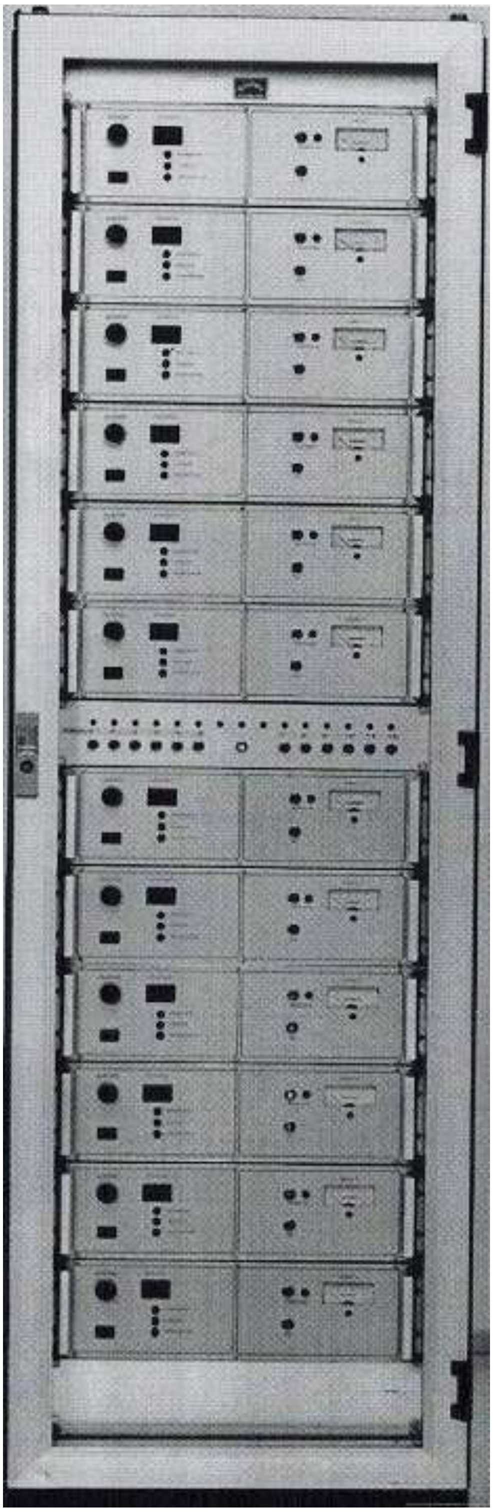

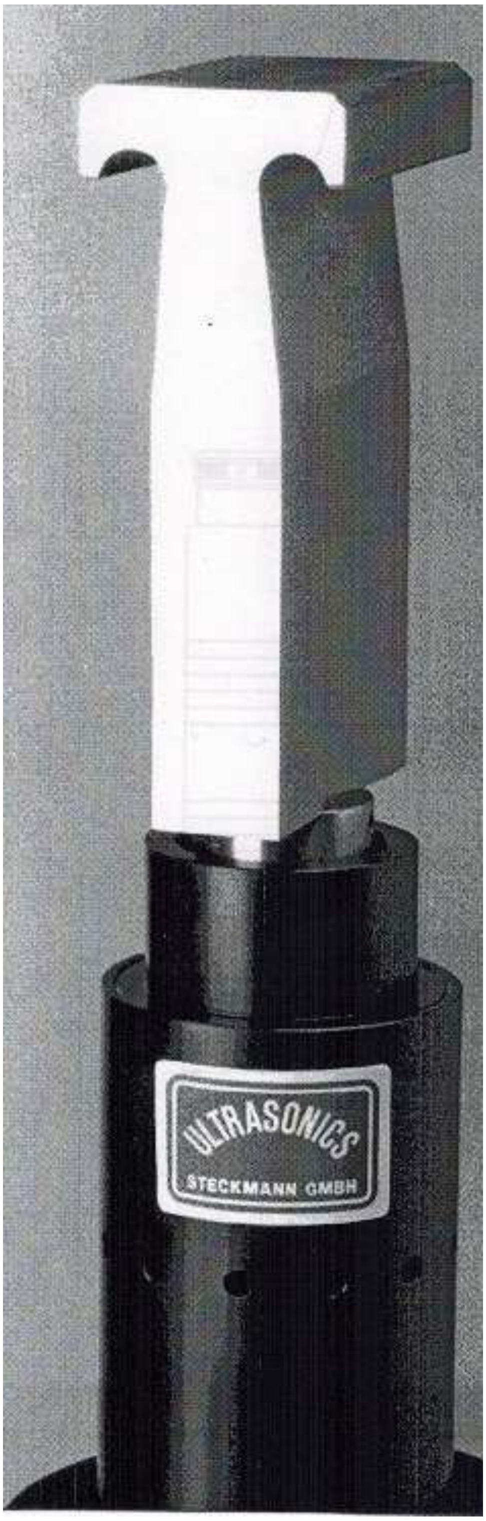

US generator cabinet for folding cover fabrics onto molded plastic parts

Titanium sonotrode for US edge welding

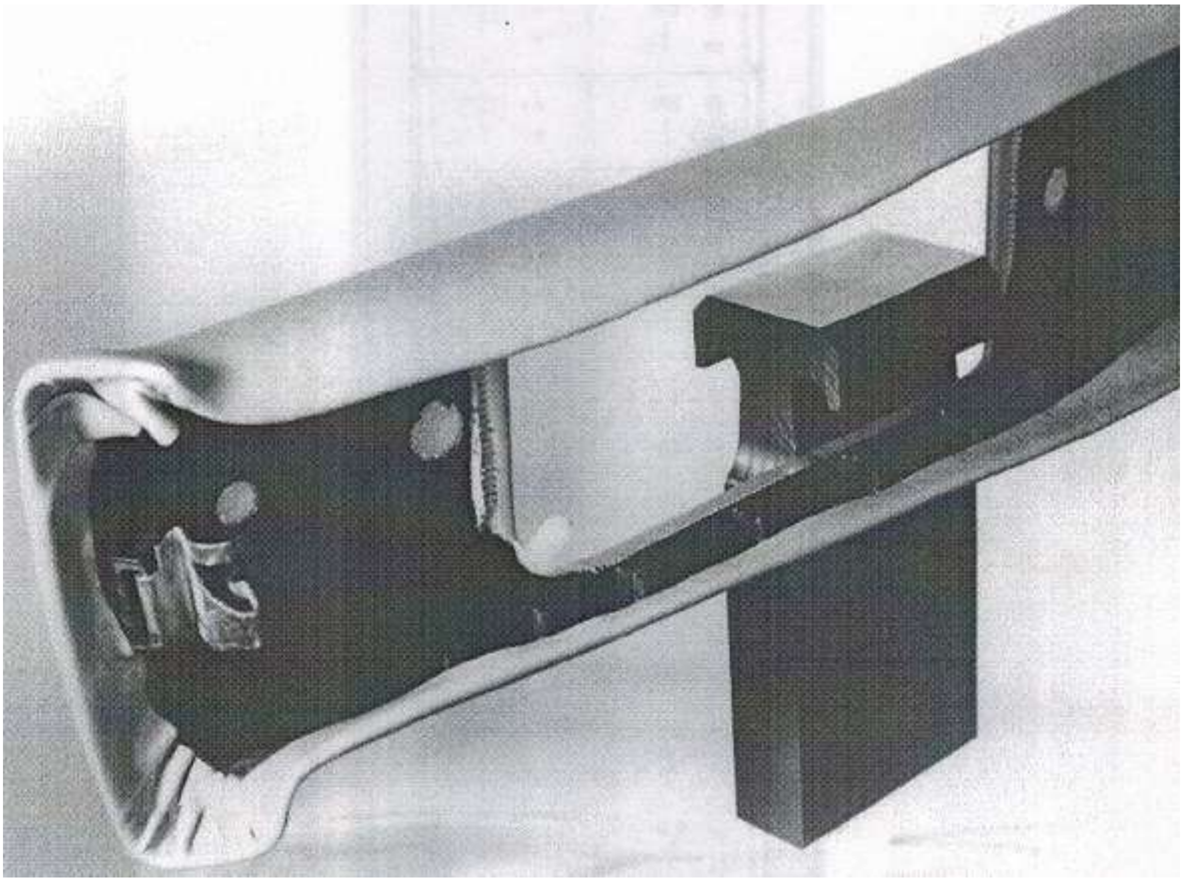

The sonotrode (previous picture) moves into the plastic molding and welds the cover fabric to the carrier material

Tuning device for US vibration system $(10 \div 100) kHz$

Clean US removal of the lost heads of blow molded parts made of polypropylene or polyethylene without chips

US-knife for cutting highly tough materials with reduced friction

8. Referencies

1. Akustische Wellen und Felder, Deutsche Gesellschaft für Akustik e.V., März 2006, 90 S..

2. D. Krahé, D. Schreckenberg, F. Ebner, Ch. Eulitz, U. Möhler. Machbarkeitsstudie zu Wirkungen von Infraschall. Veröffentlichungen des Umwelt-Bundesamts. 137 S. Juni 2014.

3. K.-J. Langenberg, R. Marklein, K. Mayer. Theoretische Grundlagen der zerstörungsfreien Materialprüfung mit Ultraschall. Oldenbourg Wissenschaftsverlag 2009, 664 S..

4. V.E. Prieb. Formgedächtnisphänomene. Das Konzept dual-energetischen Martensits (CODEM) - theoretische und experimentelle Abhandlung", Monographie, 302 S. – Berlin, 2021.

5. Y. Jin, Y. Wang, Y. Ren. Theory and experimental evidence of phonon domains and their roles in pre-martensitic phenomena. Computational Materials, v. 1, 2015.

6. O. Mercier and K. N. Melton. Single-crystal elastic constants of the equiatomic NiTi alloy near the martensitic transformation. Journal of Applied Physics 51(1980)1833.

7. T. R. Finlayson,.Pretransformation phenomena as revealed by elastic waves. Metall. Trans. A 19. 2(1988)185.

8. E. Hu and W. Wang. The Elastic Constants Measurement of Metal Alloy by Using Ultrasonic Nondestructive Method at Different Temperature. Mathematical Problems in Engineering, 2016.

9. V.E. Prieb, V.P. Ljubiwoj. Acoustic Irradiation at Martensitic Transformation. Metallophysika 10 (1988) 94 (*Rus*.).

10. G. F. Nataf, A. Planes et al. Suppression of acoustic emission during superelastic tensile cycling of polycrystalline Ni50.4Ti49.6. Phys. Rev. Mat. 4(2020) 9.

11. Y.-J. Chen, W.-N. Hsu and J.-R. Shih. The Effect of Ultrasonic Treatment on Microstructural and Mechanical Properties of Cast Magnesium Alloys. Materials Transactions, 50(2009)401.

12. I. Kostin, V. Ch. Mann, A. Krokhin et al. The Benefits of Ultrasonic Treatment of Molten Metal for Slabs Casting at UC RUSAL Facilities. In book: Light Metals, 2018.

13. V.L Popov. Reibung unter Einwirkung von Ultraschall. In Buch: Kontaktmechanik und Reibung. 2010.

14. K. Siegert at al. Ultraschallbeeinflusstes Umformen metallischer Werkstoffe. Maschinenmarkt 7(2001)22.

15. V.E. Prieb. Einfluss der Ultraschallbehandlung auf die Oberfläche von Gewindeteilen eines Fotoobjektives aus Alu und Messing, Bericht an die Fa. „Ultrasonics Steckmann GmbH“ und an die „Leica Camera AG“, 2001, http://www.materialforschungsservice-dr-prieb.de/LeikaProjektKfassung.htm.

16. Fügen von Formteilen und Halbzeugen aus thermoplastischen Kunststoffen mit Ultraschall. Verfahrens-, Konstruktions- und Anwendungsempfehlungen. Ausgabe der Fa. „Ultrasonics Steckmann GmbH“, Grävenwiesbach, 1994.

17. H. Giesekus. Phänomenologische Rheologie: Eine Einführung. Springer 1994, 679 p.

18. D. Grewell et al.: Plastic and Composite Welding Handbook, Hanser Publishers, Munich (2003).

19. K.S. Suresh, M. Roop, R. K. Prakasan, R. Rudramoorthy. Modeling of temperature distribution in ultrasonic welding of thermoplastics for various joint designs. Journal of Materials Processing Technology 186(2007)138.

20. V. Prieb, H. Steckmann. Thermoelasticity and hysteresis of martensitic transformation in shape memory alloys. I. Hysteresis of the stress-free thermal transformation. Technical Physics 41(1996)1132.

21. C.B. G. Brito, J. Teuwen, C.A. Dransfeld, I.F. Villegas. The effects of misaligned adherends on static ultrasonic welding of thermoplastic composites. Composites Part A: Applied Science and Manufacturing 155(2022)106810.

22. F. Senders, M. van Beurden, G. Palardy. Zero-flow: a novel approach to continuous ultrasonic welding of CF/PPS thermoplastic composite plates. Advanced Manufacturing: Polymer & Composites Science 2(2016)3-4.

23. M.S. Blanter, I.S. Golovin, H. Neuhäuser, H.-R. Sinning. Internal friction in metallic materials: a handbook. 1. Auflage. Springer, 2007, 559 p..

24. V. Prieb und H. Steckmann. Strukturelle Aspekte des Metallverbindens, -streckens und -prägens im Ultraschallschweißverfahren, „Ultrasonics Steckmann GmbH“, Bericht 1999. Online im Internet <http://www.materialforschungsservice-dr-prieb.de/Ultraschallmetallsschweissen_De.pdf>: Der letzte Abruf 2022.

25. J. Johns, C. DePrisco. The Application of Ultrasonic Energy to Cold Welding of Metals, Research report, Aeroprojects Inc. 1953, n. 53-77.

26. M. Okada, S. Shin, M. Miyagi and H. Matsuda. Joint mechanism of ultrasonic **welding**. Journal of Japan Institute of Metals, 4(1962) 250.

27. C. F. Brockelsb. Some Applications of Ultrasonics. J. Sci. Instrum., 40(1963)153.

28. H. P. C. Daniels. Ultrasonic Welding. Ultrasonics (1965)190**.**

29. T. H. Hazlett and S. M. Ambekar. Additional Studies on Interface Temperatures and Bonding Mechanisms of Ultrasonic Welds. Welding Research Supplement, AWS (1970)196.

30. H. Kreye. Melting Phenomena in Solid State Welding Processes. Welding Research Supplement, AWS (1977)154.

31. K. Graff, Ultrasonic Metal Welding, New Developments in Advanced Welding, Cambridge, (1997)241.

32. American Welding Society Handbook, Vol. 2, 8th ed., 1997.

33. T. Watanabe, A. Yanagisawa and S. Sunaga. Auger Electron Spectroscopy Analysis at the Ultrasonically Welded Interface between Alumina and Aluminum. Metallurgical and Materials Transactions A, 34A(2003)1107.

34. E. De Vries, Mechanics and Mechanisms of Ultrasonic Metal Welding, Ph.D. Thesis, Ohio State University, 2004.

35. D. Bakavos and P. B. Pragnell. Mechanism of joint and microstructure formation in high power ultrasonic spot welding 6111 aluminium automotive sheet. Material Science and Engineering A, 527(2010)6320.

36. B. Sanga, R. Wattal, D. S. Nagesh. Mechanism of joint formation and characteristics of interface in ultrasonic welding: Literature review. Periodical of Engineering and Natural Science 6(2018)1.

37. D. Stöckel und H.J. Oberg. Ultraschallschweißen von Kontaktwerkstoffen, Z. f. Werkstofftechnik, 6(1975)4.

38. D. Stöckel. Ultraschallschweißen in der Kontakttechnik, ETZ 101(1980)18.

39. D. Stöckel. Kontaktschweißtechnik. Lagebericht, F+M, 91(1983)6.

40. B. Oertel. AgMeO-Kontakte mit Ultraschall geschweißt, Kontaktverhalten und Schalten, 11. Kontaktseminar vom 25. – 27. Sept. 1991 an der Uni Karlsruhe, VDE-Fachbericht 42, vde-verlag gmbh, Berlin 1991, S. 131-138.

41. Ch. Born, G. Wagner, D. Eifler. Ultrasonically welded aluminium foams / sheet metal – joints. Advanced Engineering Materials, 8(2006)816.

42. H.-D. Golde. Ultraschallmetallschweißen, die Bibliothek der Technik, Band 108, verlag moderne industrie, 1995, 70 S..

43. J. Tsujino, T. Ueoka, I. Watanabe et all. New methods of ultrasonic metal welding, 1993 IEEE Ultrasonics Symposium, 405-410.

44. B. Gonzalez, S. Knecht, H. Handy and J. Ramirez. The effect of ultrasonic frequency on fine pitch aluminium wedge wirebond,1996 Electronic Components and Technology Conference, 1078-1087.

45. N. Murdeshwar, J.E. Krzanowski. A microstructural study of dislocation substructures formed in metal foil substrates during ultrasonic wire bonding. Metallurgical and Material Transactions A, 28A(1997)2663.

46. V.E. Panin, V.A. Klimenov, V.P. Bezborodov et all. Substructural and phase transformations in ultrasound treatment of a martensitic steel. Physics and Chemistry of Material treatment, 27(1993)593.

47. N. Shen, A. Samanta, H. Ding, W. Cai. Simulating Microstructure Evolution of Ultrasonic Welding of Battery Tabs. Procedia Manufacturing 5(2016)399.

48. A. Rusinko, Ali H. Al Hilfi, M. Rusinko. An analytic description of the creep deformation of metals in the ultrasonic field. Mechanics of Time-Dependent Materials, June 2021.

49. M.R. Sriraman, R. Vasudevan. Some aspects of the damage caused in metallic materials by ultrasonic vibrations. Journal of Materials Processing Technology, 54(1995)47.

50. G.V. Bushueva, G.M. Zinenkova, V.I. Reshetov, A.A. Khromov. Ultrasound-induced dislocation configuration in CdS crystals. Physics of the Solid State, 36(1994)391.

51. J. Tsujino, T. Ueoka, I. Watanabe et all. New methods of ultrasonic metal welding. IEEE Ultrasonics Symposium, 1993, 405-410.

52. J. Tsujino. Recent development of ultrasonic welding. IEEE Ultrasonics Symposium, 1995, 1051-1060.

53. K. Adachi, M. Saito, M. Ikeya and S. Mori. Development of torsional-vibration systems used for high frequency ultrasonic plastic welding. IEEE Ultrasonics Symposium, 1995, 1061- 1064.

54. J. Woltersdorf, E. Pippel, E. Roeder et al. Interlayer microstructure and bonding behaviour of ultrasonic-welded aluminium-oxide/aluminium joints. Physika status solidi A, 150A(1995)307.

55. H. Czichos. Über den Zusammenhang zwischen Adhäsion und Elektronenstruktur von Metallen bei der Rollreibung im elastischen Bereich. Doktorarbeit, TU Berlin, 1968, 81S..

56. V. Prieb and H. Steckmann. Pseudo-Plastic Behaviour of Single-Crystals of Cu-Base Memory Alloys. J. de Physique IV, 5(1995)C8-907.

57. H. Steckmann, V.I. Kolomytsev, A.V. Kozlov. Acoustoplastic effect in the shape memory alloy Ni-Ti-Re at the ultrasonic frequency. Ultrasonics 2133(1998) 215.

58. J. Tsujino, T. Ueoka, Y. Asada, S. Taniguchi, Y. Iwamura. Measurement of the temperature rise at the welding surface of different metal specimens joined by a 15 kHz ultrasonic butt welding system, „Jap. J. of Appl. Phys., Part 1“, 37(1998)2996.

59. B. Tippelt, D. Klimm, P. Paufler. Plastic deformation of GaAs by ultrasonic treatment. Phil. Mag. A, 69A(1994)741.

60. M.R. Sriraman, R. Vasudevan. Some aspects of the damage caused in metallic materials by ultrasonic vibrations. Journal of Materials Processing Technology, 54(1995)47.

61. M. J. Ablowitz, J. T. Cole, P. Hu, and P. Rosenthal. Peierls-Nabarro barrier effect in nonlinear Floquet topological insulators. Phys. Rev. E 103, 042214 – Published 27 April 2021.

62. I.V. Ostrovskii, L.P. Steblenko, A.B. Nadtochii. Effect of ultrasonic treatment on the mobility of short dislocations in Si crystals. Phys. Solid State **42**(2000)488.

63. D.V. Bachurin, R.T. Murzaev, J.A. Baimova et al. Ultrasound influence on behavior of disordered dislocation systems in a crystal with non-equilibrium grain boundaries. Letters on Materials, 6(2016)183.

64. D.V. Bachurin, R. Murzaev, A. Nazarov. Ultrasonic influence on evolution of disordered dislocation structures. Modelling and Simulation in Materials Science and Engineering 25(2017).

65. D.V. Bachurin, R. Murzaev, A. Nazarov. Relaxation of dislocation structures under ultrasonic influence. International Journal of Solids and Structures 156(2019)1.

66. E. Ruszinkó, A. H. Al Hilfi. The Effect of Ultrasound on Strain-hardened Metals. Acta Polytechnica Hungarica (2021).

67. A. Rusinko, A. H. Al Hilfi. Ultrasound-assisted creep deformation of metals. APTEFF, 52, 1-273 (2021), UDC: 669-1:621.9.048 DOI: https://doi.org/10.2298/APT2152265R BIBLID: 1450-7188 (2021) 52, 265-273.

68. A. Rusinko, A. H. Al Hilfi, M.Rusinko. An analytic description of the creep deformation of metals in the ultrasonic field. Mechanics of Time-Dependent Materials, Online First 2021.

69. A. Prabhakara, G. Ch.Vermaa et al. Dislocation density based constitutive model for ultrasonic assisted deformation. Mechanics Research Communications 85(2017)76.